MICROSTRUCTURE AND MECHANICAL PROPERTIES OF MEDIUM MN STEEL

MICROSTRUCTURAL EVOLUTION AND MECHANICAL PROPERTIES OF MEDIUM MANGANESE TRANSFORMATION INDUCED PLASTICITY THIRD GENERATION ADVANCED HIGH STRENGTH STEEL

BY: VIVEK PATEL, B.ENG

A Thesis

Submitted to the School of Graduate Studies

in Partial Fulfilment of the Requirements

for the Degree

Master of Applied Science

McMaster University

McMaster University	MASTER OF APPLIED SCIENCE (2019)
Hamilton, Ontario	(Materials Science & Engineering)

TITLE:	Microstructural Evolution and Mechanical Properties of Medium Manganese Transformation Induced Plasticity Third Generation Advanced High Strength Steel
AUTHOR:	Vivek Patel, B. Eng (McMaster University)
SUPERVISOR:	Dr. Joseph R. McDermid
NUMBER OF PAGES:	107

Abstract

Third-generation advanced high strength steels (3G AHSS) are being developed to facilitate vehicle lightweighting in order to improve their fuel efficiency without compromising passenger safety. This thesis will examine the development of microstructure and mechanical properties of a prototype medium Mn TRansformation- and TWinning-Induced Plasticity (TRIP/TWIP) 3G-AHSS with a composition of 0.15C-6Mn-1Si-1Al. Heat treatments consisting of intercritical annealing and overageing stages compatible with the continuous galvanizing process were investigated in terms of their effects on the microstructure and the mechanical properties from the as-received, tempered martensite (TM) microstructure and a fully martensitic (M) starting microstructure. Samples intercritically annealed from the M starting microstructure exhibited a lamellar morphology of retained austenite/martensite laths and faster austenite reversion kinetics. Samples intercritically annealed from the TM starting microstructure exhibited a globular/equiaxed morphology and slower austenite reversion kinetics. Though they had high (~0.3 volume fraction) initial amounts of retained austenite, samples intercritically annealed from the TM starting microstructure did not meet the 3G-AHSS mechanical property envelope due to insufficient mechanical stability of retained austenite and its resulting transformation to α'-martensite at low strains. These samples did, however, show impressive UTS values (up to 1600 MPa), despite lower tensile elongation values. Despite having lower fractions of retained austenite in the as-annealed microstructure, the samples intercritically annealed from the M starting microstructure achieved combinations of strength and tensile elongations that met the 3G-AHSS mechanical property envelope. In

particular, the M-690-120 sample nearly met the specific U.S. DOE mechanical property target of 1200 MPa UTS and 30% TE exhibiting 1150 MPa UTS and 29% TE. TEM results from strained and fractured tensile samples showed that samples intercritically annealed from the TM and M starting microstructures both exhibited deformation twinning in the retained austenite, which suggests that the combination of the TRIP and TWIP effect resulted in an excellent combination of strength and tensile elongation.

Based on experimental results, this work demonstrates that medium Mn TRIP/TWIP alloys are capable of achieving the target 3G-AHSS mechanical properties employing heat treatments compatible with the continuous galvanizing process.

Acknowledgements

I would like to thank my supervisor, Dr. Joseph McDermid for his guidance and support during my time as a graduate student. I appreciate the voice in my head that is always asking about the “underlying mechanism”.

I would like to thank the International Zinc Association Galvanized Autobody Partnership (IZA-GAP) for their financial support and U.S. Steel Research for providing the substrate material.

I would like to thank all the technical professionals that have assisted with analysis and/or training: John Thompson and Ray Fullerton (McMaster Galvanizing Simulator), Doug Culley, Xiagang Li and Ed McCaffery (MSE labs), Chris Butcher, Carmen Andrei, Andy Duft and Jhoynner Martinez (CCEM), Dr. Fateh Fazeli and Marta Aniolek (CANMET) Dr. James Britten and Vicky Jarvis (MAX), Dr. Elizabeth McNally and Dr. Mike Bruhis (CAMC).

Special thanks to Daniella Pallisco and Sara Filice for their support and input since undergrad. A special thanks to all my friends, especially those supporting the VP-EP. I would like to thank my family for their unwavering support.

Finally, I would like to thank my Guru H.D.H. Hariprasad Swamiji, without whom, none of this would be possible.

Abbreviations and Symbols

List of Abbreviations

1G	First Generation
2G	Second Generation
3G	Third Generation
AHSS	Advanced High Strength Steel
BIW	Body in White
C&S	Carbon and Sulphur
CGL	Continuous Galvanizing Line
CIF	Crystallographic Information Files
CP	Complex Phase Steel
DP	Dual Phase Steel
DSA	Dynamic Strain Ageing
EDM	Electric Discharge Machining
IAT	Intercritical Annealing Temperature
ICP-OES	Inductively Coupled Plasma - Optical Emission Spectroscopy

ICSD	Inorganic Crystal Structure Database
IR	Infrared
L-IP	Lightweight Steels with Induced Plasticity
M	Martensite
MART	Martensitic Steel
MGS	McMaster Galvanizing Simulator
Q&P	Quench and Partition
SEM	Scanning Electron Microscope
SFE	Stacking Fault Energy
SSA	Static Strain Ageing
TCFE	Thermo-Calc Software and Fe-alloys Database
TE	Total Elongation
TEM	Transmission Electron Microscope
TM	Tempered Martensite
TRIP	Transformation Induced Plasticity
TWIP	Twinning Induced Plasticity
U.S. DOE	United States Department of Energy

UFG	Ultra Fine-Grained
UTS	Ultimate Tensile Strength
XRD	X-Ray Diffraction
YPE	Yield Point Elongation

Table of Contents

List of Tables

List of Figures

Chapter 1: Introduction

1.1. Advanced High Strength Steel

Automotive weight reduction is being driven by consumer demands and government regulations to improve fuel efficiency, while simultaneously improving vehicle crashworthiness [1]. Automotive manufactures require materials with good combinations of strength, formability, toughness and fatigue resistance across a large variety of parts and applications. Advanced high strength steels (AHSSs) have [2], and continue to meet these demands [3], exemplified in the body-in-white (BIW) of the 2019 Volvo XC90, shown in Figure 1.1, which highlights the significant utilization of various AHSS grades utilized for different components.

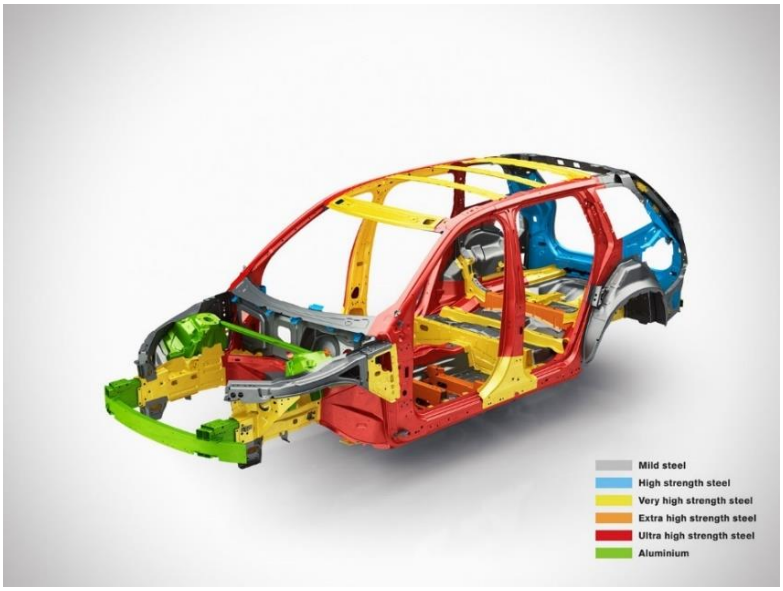

Figure 1.1: Schematic of Volvo XC90 (2019) showing different grades of steel used in the body in white [4].

Ongoing research to improve the balance of strength and ductility of AHSSs has given rise to different generations of AHSSs, where Figure 1.2 shows the different generations of AHSSs, which are defined by the product of their ultimate tensile strength and ductility (as measured by total elongation).

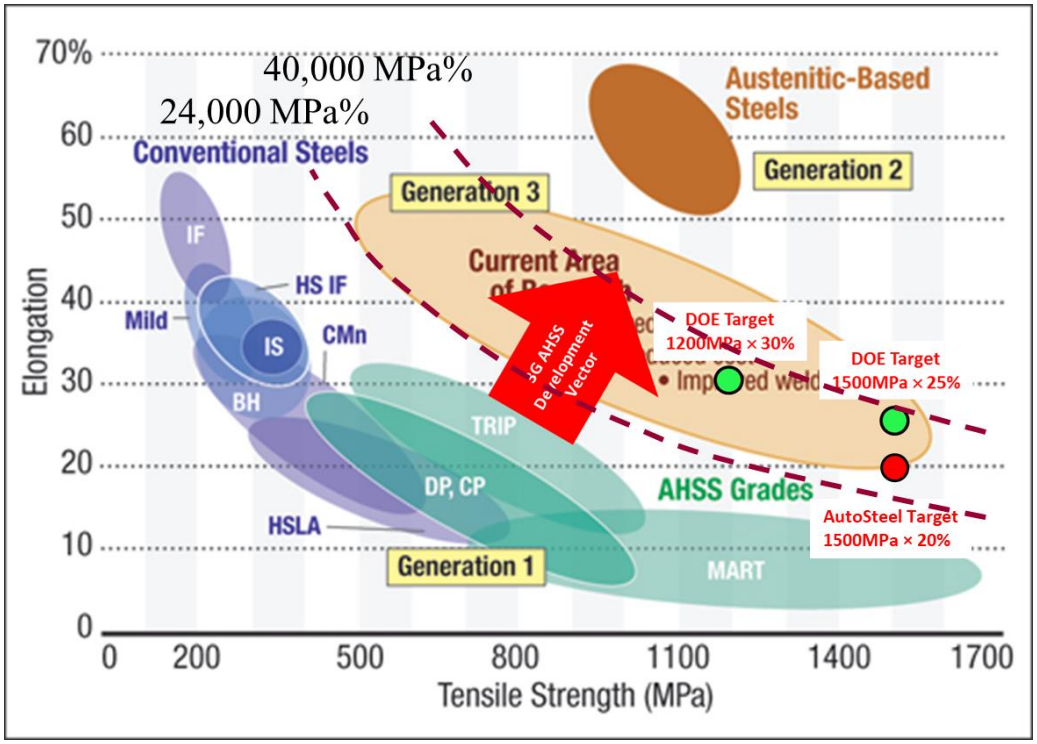

Figure 1.2: Classifications of AHSSs with the 3G-AHSSs mechanical property target window and specific U.S. DOE targets [5].

First generation (1G) AHSS are based on varying the relative volume fractions of ferrite and martensite, with small fractions of bainite and, in the case of the 1G TRansformation Induced Plasticity (TRIP) steels, small fractions (≤ 15%) transformable retained austenite. It has been shown by Matlock et al. [6] that the mechanical properties of the 1G AHSS can be modelled using a simple rule of mixtures formalism of ferrite and

martensite [6]. The 1G AHSSs, in general, have a relatively lean composition, making them inexpensive to manufacture, and include dual phase (DP), low alloy TRIP, complex phase (CP) and martensitic (MART) steels. The strength and ductility balance of 1G-AHSSs is defined by the mechanical property envelope (Fig 1.1) of 10,000 MPa% ≤ UTS × TE ≤ 20,000 MPa% [1][3].

Second generation (2G) AHSS have an austenite-based microstructure and include transformable austenitic stainless steels, high Mn twinning induced plasticity (TWIP) steels and lightweight steels with induced plasticity (L-IP). These steels require high levels of alloying additions, usually Mn, Ni and C, to stabilize the austenitic microstructure, making them expensive and difficult to produce and process. The strength and ductility balance of 2G-AHSSs is generally defined as being within the 50,000 MPa% ≤ UTS × TE ≤ 80,000 MPa% mechanical property envelope [7].

Third generation (3G) AHSSs are being researched to develop alloys that have superior mechanical properties relative to the 1G-AHSSs with lower levels of alloying additions compared to 2G-AHSSs making them cheaper. The 3G-AHSSs have been designed around a variety of microstructures, with the so-called enhanced 3G TRIP steels (Figure 1.2) being the focus of the present research. These grades have large volume fractions (i.e. 0.20 to 0.40) of mechanically transformable, chemically metastable retained austenite due to a combination of alloying additions and thermo-mechanical processing. The United States Department of Energy (U.S. DOE) has defined specific mechanical property targets of 1500 MPa × 25% TE and 1200 MPa × 30% TE and AutoSteel has defined a specific mechanical property target of 1500 MPa × 25% TE for these steels

(Figure 1.2). Matlock et al. [7] have proposed a more modest mechanical property target envelope of UTS × TE ≥ 24,000 MPa%. Numerous strategies have been investigated to develop 3G-AHSSs such as enhanced DP steels, ultrafine bainitic steels modified TRIP steels, one and two step quench and partition (Q&P) steels [3], [7].

Medium manganese TRIP-assisted steels are amongst the most promising candidates in the 3G AHSS literature [8]–[11]. These alloys contain 5 % to 10 % Mn alongside alloying additions of C, Si, Al, Cr and microalloying additions of Ti, Nb and V. These steels rely on maximizing the amount of chemically stable retained austenite and the subsequent mechanical activation of plasticity enhancing mechanisms such as the TRIP effect and TWIP effect [12], [13]. Several researchers have shown that the volume fraction and stability of retained austenite is dependant upon the starting microstructure as well as the thermal processing cycle [9], [14], [15].

However, automotive steels are susceptible to corrosion when exposed to the environment while in service and, thus, require some form of corrosion protection to maintain the structural integrity of the vehicle. Continuous galvanizing is the most economic industrial-scale method used to achieve robust corrosion protection of steel substrates. Therefore, thermal processing cycles developed to obtain target mechanical properties must be compatible with existing continuous galvanizing line (CGL) processing capabilities [16]. Numerous studies were able to achieve excellent balances of strength and ductility, meeting the 3G AHSS mechanical property envelope; however, the intercritical annealing temperature holding times tended to be very long, making the thermal cycles incompatible with the CGL [6], [9], [17], [18]. The objective this research is to develop a

CGL compatible thermal processing route for a prototype medium Mn TRIP/TWIP-assisted AHSS to maximize the amount of chemically stable retained austenite and, ultimately, to achieve mechanical properties that meet the 3G AHSS mechanical property target envelope [19], [20].

Chapter 2: Literature Review

2.1. Continuous Galvanizing

Continuous hot dip galvanizing is used to provide automotive sheet product with corrosion protection. This is achieved by (1) barrier protection, where the Zn coating acts as a barrier between the underlying substrate and the corrosive environment and (2) galvanic protection, where the Zn coating acts as a sacrificial anode if the coating is damaged. Providing corrosion protection is of paramount importance for maintaining long-term vehicle structural integrity and meeting consumer durability expectations, especially when thinner steel cross-sections are used in weight savings applications.

Most sheet products are made using the Sendzimir-type continuous hot-dip galvanizing process, a schematic of which is shown in Figure 2.1. Steel sheets are welded together to form a continuous sheet. The sheet is cleaned to remove oils, iron fines, loose soils and surface carbon from the cold rolled sheets to improve coating adherence and prevent contamination of the Zn bath [16]. Electrolytic cleaning is used to remove tightly adhered contaminants on the steel surface. After cleaning, the steel sheet is dried to remove any moisture on the surface. The sheet then enters the annealing stage consisting of direct fired furnace or a radiant tube furnace. The annealing furnace has two major functions, (1) annealing the sheet to obtain the desired mechanical properties and (2) reducing any iron oxides on the steel surface. The annealing step typically lasts 60 s to 240 s at the peak annealing temperature. To control the partial pressure of oxygen (pO_2) of the process

atmosphere, a controlled mixture of $N_2/H_2/H_2O$ gas is employed. The sheet is then cooled to the molten Zn bath temperature (usually 460°C) and held there to homogenize the temperature through the thickness of the sheet prior to being immersed in the Zn bath for 2 s to 4 s. As the sheet exits the Zn pot, gas jet wipers remove excess Zn and control the final coating thickness. The Zn coating solidifies by natural convection. In the galvannealing process, the galvanized steel sheet is annealed to form a coating consisting of numerous Fe-Zn intermetallics. Finally, the Zn coated sheet is sent to post surface treatments, tension levelling, inspection and packaging [16].

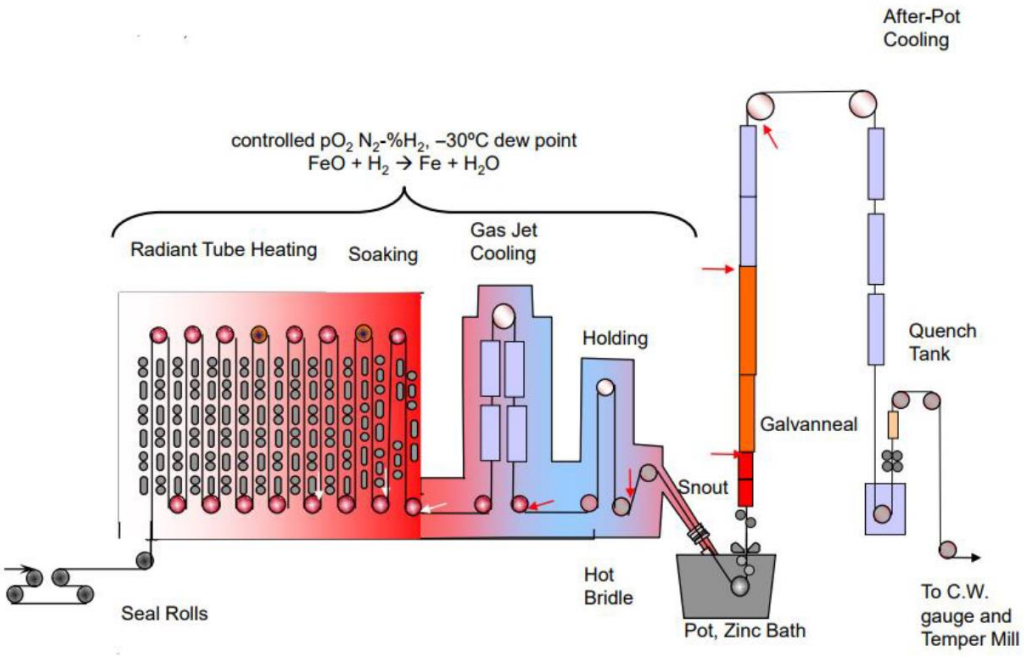

Figure 2.1: Schematic of the continuous hot-dip galvanizing/galvannealing process [21].

Al is added to the galvanizing bath to form the $Fe_2Al_5Zn_x$ inhibition layer at the steel-coating interface. The inhibition layer delays the formation of Fe-Zn intermetallics which are brittle and may cause the coating to crack [16]. Obtaining a high-quality Zn

coating is challenging in the case of medium Mn steels due to the increased alloy content, such as Si and Mn required to obtain the desired mechanical properties [20], [22]. The process atmosphere within the annealing furnace is reducing with respect to Fe, however, alloying additions such as Mn, Si, Al and Cr are selectively oxidized. The Wagner model [23] describes the kinetic factors that determine whether elements form internal and/or external oxides. External oxides prevent the formation of the interfacial layer, which results in poor coating adhesion and/or coating defects such as bare spots [24][25]. Selective oxidation is a critical issue when considering introducing medium Mn steels into industrial production, however, this will not be addressed in this work.

2.2. Advanced High Strength Steels

The various generations of advanced high strength steel (AHSS) were discussed in §1.1. where first generation (1G) AHSS have a lean alloy composition and the strength and ductility balance of 1G-AHSSs is within the 10,000 MPa% ≤ UTS × TE ≤ 20,000 MPa% mechanical property envelope [1], [3]. 2G-AHSS have higher levels of alloying additions and the strength and ductility balance of 2G-AHSSs is within the 50,000 MPa% ≤ UTS × TE ≤ 80,000 MPa% mechanical property envelope [7]. 3G-AHSSs contain fewer alloying additions compared to 2G-AHSSs and superior mechanical properties 1G-AHSSs. Matlock et al. [7] have proposed a strength and ductility balance for 3G-AHSSs mechanical property target envelope of UTS × TE ≥ 24,000 MPa%.

The composite model developed by Matlock et al. [26] provided targets for the required microstructural constituents and their volume fractions that result in a desirable

balance of strength and ductility. The composite model was based on the rule of mixtures, where an iso-strain model was employed. The volume fractions of the constituents were varied and the effects on the mechanical properties i.e. TE and UTS were plotted and superimposed on a graph showing the mechanical properties of various classes of AHSS grades Figure 2.2. The ferrite/martensite composite model overlapped with the 1G-AHSS grades while that of austenite/martensite fell into the 3G-AHSS mechanical property envelope Figure 2.2, however, it assumed fully stable retained austenite that did not transform to martensite during deformation [7], [26]–[28].

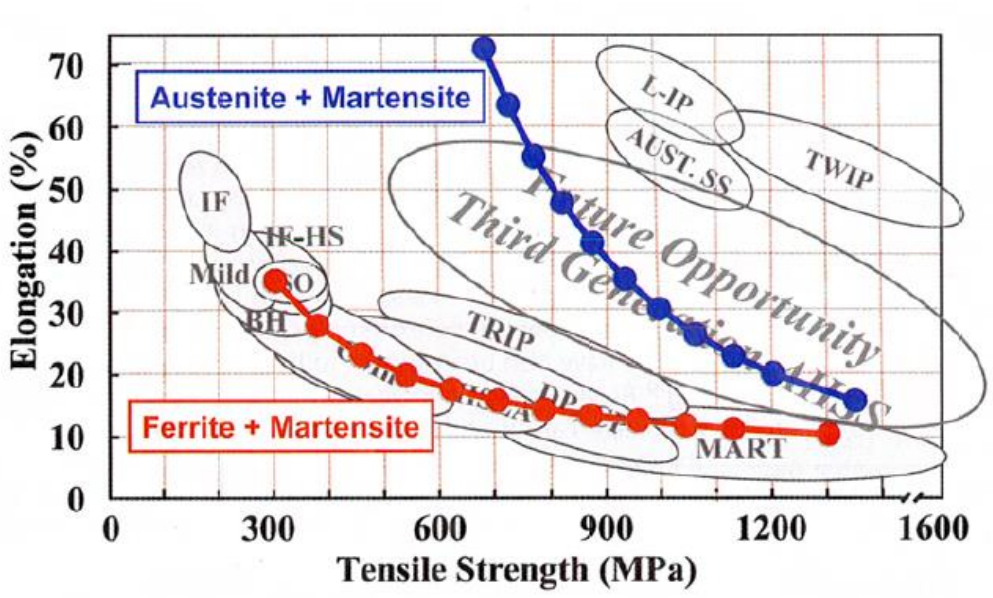

Figure 2.2: Composite models predicting the mechanical properties of ferrite-martensite and austenite-martensite mixtures superimposed on mechanical property overview of advanced high strength steels [27].

The stability of retained austenite was considered to develop a more accurate model (Figure 2.3(a)). Figure 2.3(b) shows the predicted mechanical properties for a ferrite-austenite composite model with the varying stabilities of the austenite shown in Figure 2.3(a).

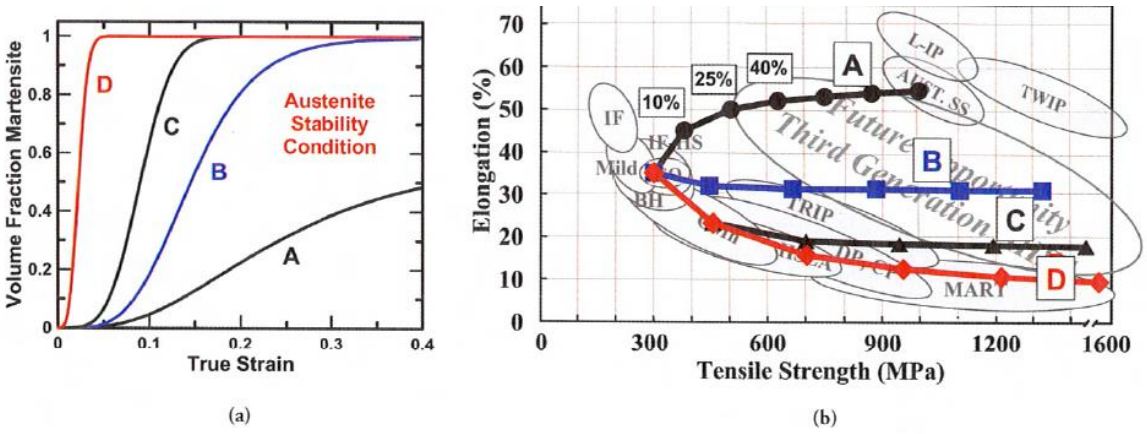

Figure 2.3: (a) Shows the transformation kinetics of austenite with varying stabilities and (b) shows how the mechanical properties of the austenite-ferrite composite model change with austenite stability [27].

The least stable austenite (curve D) transformed to martensite at low strains (Figure 2.3(a)) and the corresponding mechanical properties fell within the 1G-AHSS mechanical property envelope (Figure 2.3(b)). The stability and volume fraction play an important role in the global mechanical properties. The best combinations of strength and ductility (Figure 2.3(b)) were brought about from high volume fraction (0.40) of relatively stable retained austenite (curve B in Figure 2.3(a)). The model suggests that 3G-AHSSs will have complex microstructures consisting of high strength phases such as martensite and ductile phases exhibiting significant strain hardening like retained austenite. A summary of some of the

approaches adopted to achieve the desirable microstructure and mechanical properties are discussed below [3], [28].

Quench and Partition (Q&P) is a two-stage process wherein specimens are fully austenitized and rapidly cooled to the quench temperature between the M_s and M_f temperature resulting in a microstructure consisting of martensite and retained austenite. The specimen is then held at this temperature or heated to the partitioning temperature that is still below the M_s temperature where C partitions from the super saturated martensite into the retained austenite, improving its chemical stability resulting in a high volume fraction of chemically stable retained austenite in the final microstructure [29][30].

2.3. Medium Mn TRIP Steels

Medium Mn TRIP-assisted steels are promising candidates to achieve 3G-AHSSs mechanical property targets. Miller [31] first proposed this alloy composition, 5Mn-7Mn and 0.11C. Miller [31] showed that an ultra fine-grained (UFG) microstructure could be obtained by annealing a cold worked sample in the intercritical region, resulting in a final microstructure comprised of ferrite and retained austenite. The highest combinations of strength and tensile elongations were found in samples where austenite transformed to martensite as specimens were deformed [31].

The alloy compositions for medium Mn TRIP steels generally fall within 0.05 wt.% to 0.4 wt.% C; 4 wt.% to 12 wt.% Mn; 0.5 wt.% to 3 wt.% Al; 0.5 wt.% to 2 wt.% Si and trace amounts of microalloying elements like Ti, Mo and V [32]. C and Mn are excellent austenite stabilizers and improve the hardenability of the alloy. Partitioning of C during

intercritical annealing dictates the chemical stability of retained austenite which heavily influences the mechanical properties [33], [34]. On the other hand, Si and Al are ferrite stabilizers, increasing the transformation temperatures, i.e. A_{c1} and A_{c3} temperatures; this can necessitate greater intercritical annealing temperatures (IATs), which increases the diffusion kinetics of alloying elements. Faster partitioning of C and Mn to intercritical austenite allows for the formation of chemically stable retained austenite in the as-annealed microstructure for short IAT holding times [35]. Carbides have low solubilities of Si and Al, making Si and Al excellent nucleation barriers to carbide precipitation. Preventing the formation of carbides results in greater partitioning of C and Mn to the intercritical austenite, further improving the chemical stability of retained austenite [36]. Alloys containing high amounts of Al may result in as-annealed microstructure consisting of delta ferrite [11].

Researchers have shown that the volume fraction of retained austenite and its chemical stability were dependant on the starting microstructure, the IAT and IAT holding times [9], [15], [37], [38]. The stability of the retained austenite dictated the mechanical properties through the activation of one or more plasticity enhancing mechanisms over the course of deformation [12], [15], [38]. Achieving greater mechanical properties is important for vehicle weight reduction, however, to be industrially viable, the alloy must be able to be galvanized, which is typically done through the continuous hot-dip galvanizing process. Pourmajidian and McDermid [19] successfully galvanized a 0.1C-6Mn-2Si alloy [19], where Pourmajidian et al. [20] later showed that a small addition (0.05

wt.%) of surface active elements like Sn would further improve the reactive wetting of the alloy [20].

2.4. Austenite Reversion Kinetics

Intercritical annealing of medium-Mn steels from the cold rolled or fully martensitic microstructures results in austenite reverse transformation (ART). The formation of austenite from tempered martensite (TM) or martensitic (M) starting microstructures has been extensively studied to determine the conditions required to obtain sufficient amounts (0.35 volume fraction) of retained austenite in the final microstructure, that are chemically stable and gradually transform to martensite with deformation, resulting high strength and ductility. During ART annealing, austenite nucleates at martensite lath boundaries, martensite block boundaries and prior austenite grain boundaries resulting in UFG microstructure consisting of ferrite, martensite and retained austenite [39]. The UFG size and partitioning of C and Mn improve the chemical and mechanical stability of retained austenite [34], [40].

The starting microstructure influences the microstructural evolution as well as the mechanical properties exhibited by as-annealed samples. Arlazarov et al. [18] intercritically annealed a 0.1C-4.6Mn alloy from the TM and M starting microstructures to investigate the microstructural evolution. As-annealed microstructures from the M starting microstructure exhibited both globular and lamellar features whereas as-annealed microstructure from the TM starting microstructure resulted in a globular morphology. Figure 2.4 shows a schematic of the microstructural evolution proposed by Arlazarov et al. from the TM starting microstructure, named the deformed martensite structure, partial

recrystallization occurred prior to the precipitation of carbides at high angle grain boundaries such as prior austenite grain boundaries, which became nucleation sites for austenite resulting in a homogenous distribution of austenite and a globular morphology of the as-annealed microstructure (Figure 2.4(b)). On the other hand, from the M starting microstructure, carbides precipitated along martensite lath boundaries (low angle boundaries) as well as high angle grain boundaries, resulting both a lamellar and globular morphology of the as-annealed microstructure (Figure 2.4(a)) [18].

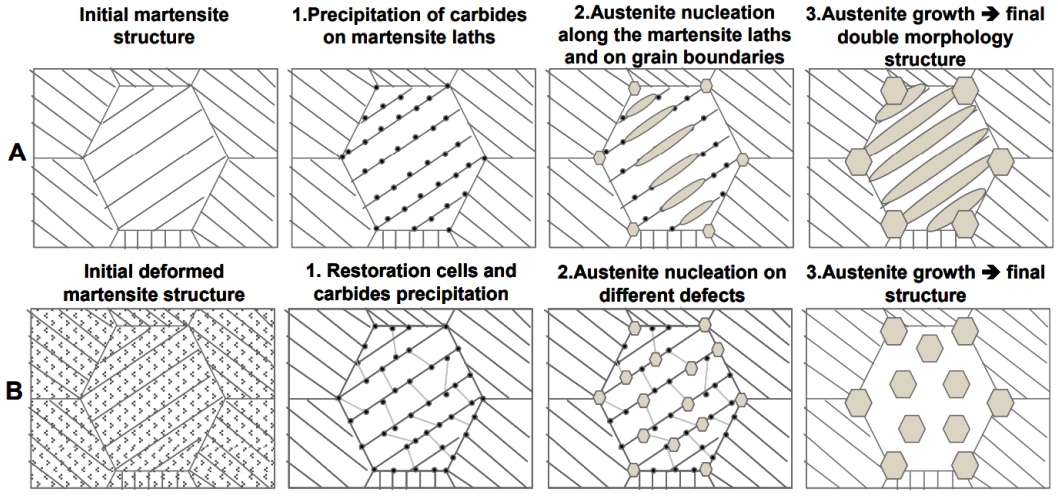

Figure 2.4: Microstructural evolution from the (a) M starting microstructure and (b) TM starting microstructure [18].

Kim et al. determined the effects of the initial microstructure on the austenite reversion kinetics and microstructural evolution of a 0.2C-2.2Mn-1.5Si alloy. Three starting microstructures were investigated, denoted CR, M1 and M2. The CR structure was a heavily consisting of pearlite and ferrite. The M1 was a martensitic microstructure with a small fraction (0.03) of retained austenite present, formed by austenitizing the CR

microstructure above the A_{c3} temperature for 600 s and quenching to room temperature at a cooling rate of 25°C/s and the M2 microstructure was a fully martensitic microstructure obtained by quenching the fully austenitized microstructure at 100°C/s and subsequently quenching in liquid nitrogen [41].

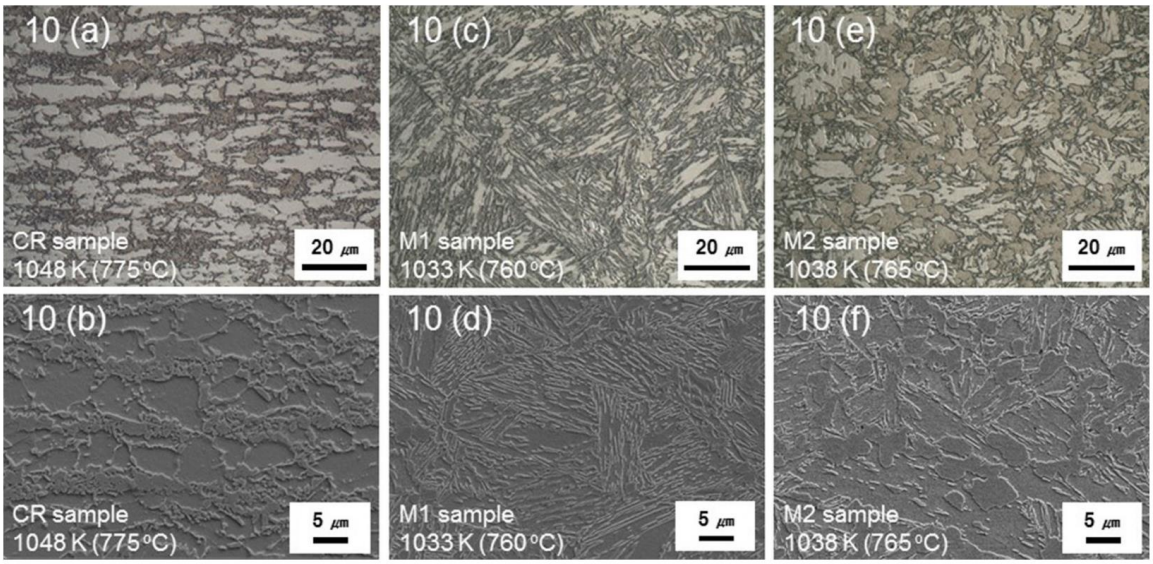

Figure 2.5: Optical and corresponding SEM images of samples intercritically annealed, held for 1 s and quenched from the (a)(b) CR starting microstructure; (c)(d) M1 starting microstructure and (e)(f) M2 starting microstructure [41].

As-annealed samples from the CR starting microstructure resulted in slower austenite reversion transformation kinetics compared the M1 and M2 starting microstructures. This was attributed to the more complex M1 and M2 microstructure giving rise to a greater number of nucleation sites compared to the CR starting microstructure consistent with the findings of other researchers [8], [14], [42]. Samples intercritically annealed from the CR starting microstructure resulted in a globular morphology (Figure

2.5(a)(b)), consistent with the findings of Arlazarov et al's. [18]. Although both M1 and M2 have a martensite starting microstructure, the as-annealed samples show very different morphologies. As-annealed sample from the M1 (Figure 2.5(c)(d)) starting microstructure resulted in a lamellar morphology whereas, samples intercritically annealed from the M2 (Figure 2.6(e)(f)) starting microstructure resulted in a globular morphology. Small films of retained austenite were observed in the M1 starting microstructure from which, the authors suggested the austenite grew during intercritical annealing, in which case, carbide precipitation was not necessary as there was retained austenite available where austenite continued growing, resulting in a lamellar morphology (Figure 2.5(c)(d)). Whereas no such retained austenite was present in the M2 microstructure, therefore, austenite nucleation occurred after precipitation of carbides at high-angle grain boundaries such as prior austenite grain boundaries, resulting in a globular/equiaxed morphology (Figure 2.5(c)(d)) [41].

Luo et al. [38] investigated 0.1C-5Mn and 0.2C-5Mn alloys and the effects of the starting microstructure and IAT on the microstructural evolution and mechanical properties. Luo et al. [38] observed that a higher volume fraction of retained austenite was achieved from the M starting microstructure compared to the TM starting microstructure. The faster austenite reverse transformation, shown in Figure 2.10(b), was attributed to the M starting microstructure having a greater amount of stored energy and the fine microstructure having more nucleation sites for austenite compared to the TM starting microstructure. The starting microstructures also affected the morphology of the as-annealed microstructures, where samples intercritically annealed from the TM starting

microstructure resulted in an equiaxed/globular morphology whereas samples intercritically annealed from the M starting microstructure result in a lamellar morphology [38].

De Moor et al. [43] used ThermoCalc to determine the amount of intercritical austenite that formed alongside the C and Mn content of the intercritical austenite as a function of IAT. Unfortunately, the model proposed by De Moor et al. had large discrepancies between the model and experimental results [43]. Lee et al. [9] proposed an improved model accounting for the grain size effect on stabilizing retained austenite (Figure 2.6).

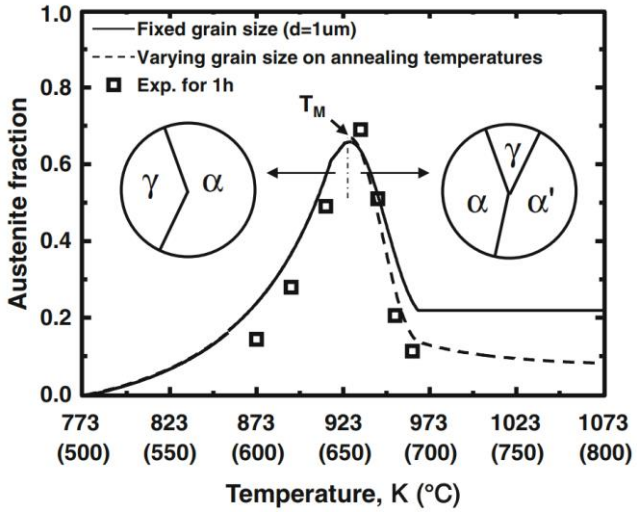

Figure 2.6: The volume fraction of retained austenite as a function of IAT. The solid line shows the model using fixed austenite grain size; dashed line shows the model using grain size varying with IAT and the hollow squares are experimental results [9].

Lee et al. [9] showed that the M_S temperature dropped for all IAT when the austenite grain size was accounted for in the model. A smaller grain size lead to shorter diffusion distance for the partitioning of alloying elements, accelerating austenite reverse transformation. The grain size was calculated as a function of IAT using DICTRA simulation of austenite growing from martensite. The best mechanical properties were obtained at an IAT slightly less than that which maximized the amount of retained austenite ("T_M"). This was attributed to the chemical stability of retained austenite that lead to its gradual transformation to martensite with deformation, allowing the sample to maintain a high work hardening rate, resulting in an excellent combination of strength and ductility [9].

Steineder et al. [14] studied a 0.1C-6.4Mn alloy from the TM and M starting microstructures (IAT holding time of 8 h). Two-step annealing entails formation of a fully martensitic microstructure prior to intercritically annealing, and it was found that retained austenite formed from the two-step process was more stable but decreased in stability with increasing IAT. Retained austenite became less stable with increasing IAT due to the dilution of C and Mn content [14].

Luo and Dong [38] and Steineder et al. [14] observed a decrease in YPE with an increase in the IAT. The authors suggested that, as the IAT was increased, a greater amount of intercritical austenite formed at the expense of ferrite. The reduction in ferrite content and reduced retained austenite stability due to dilution of the C and Mn content resulted in continuous yielding of samples intercritically annealed at greater IATs. Moreover, both authors found as-annealed samples that underwent the one-step process exhibited greater

YPE compared to the two-step process. The lamellar microstructure allowed for dislocation-dislocation interactions, resulting in an increase in dislocation density while the no such interactions were allowed in the globular microstructure resulting in significant YPE [14].

2.5. Strengthening Mechanisms

Medium Mn steels are capable of achieving an excellent balance of strength and ductility by incorporating four major strengthening mechanisms; composite strengthening, solid solution strengthening, TRIP effect and TWIP effect

2.5.1. Solid Solution Strengthening

Figure 2.7 shows the solid solution strengthening effect of various alloying elements in ferrite. C and N have the greatest solid solution strengthening effect.

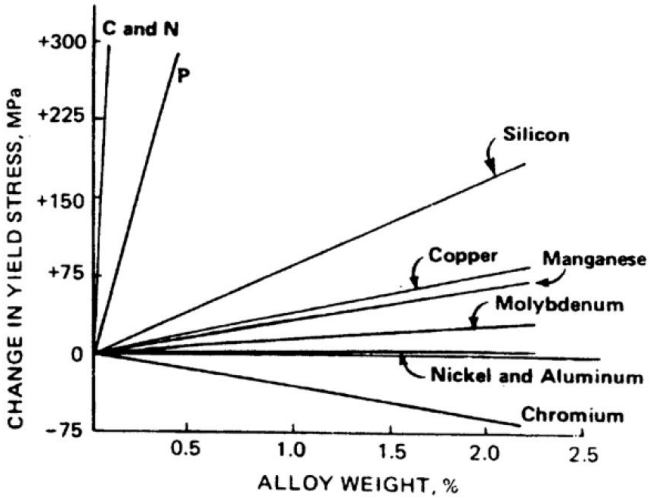

Figure 2.7: Effect of alloy additions on the solid solution strengthening in ferrite [44].

However, increasing the C content results in poor weldability of the steel, limiting the amount of C added to steel alloys for automotive applications. Generally, medium Mn steels also have Si and Mn additions to improve solid solution strengthening. Although Al does not provide any solid solution strengthening to the alloy, Si is partially or fully replaced with Al to improve the reactive wetting of the substrate by the molten Zn [45], [46], discussed in §2.1.

2.5.2. Composite Strengthening

As-annealed medium Mn steels have a multiphase microstructure consisting of ferrite, bainite, martensite and retained austenite. Using neutron diffraction Furnemont [47] measured the yield strength of ferrite, bainite, austenite and martensite to be 500 MPa, 650 MPa, 900 MPa and 2000 MPa, respectively in a low-alloy TRIP-assisted steel containing 0.3C-1.4Mn-1.4Si. Furnemont et al. [48] attributed the greater strength of austenite compared to ferrite and bainite to C partitioning to austenite during intercritical annealing [48]. Jacques et al. [49] modelled the mechanical behaviour with the law of mixtures, assuming an iso-strain model to determine the stress partitioning of each phase, shown in equation 2.1. The harder phases within the matrix improved the overall strength of the material [48][50].

$$\sigma(\varepsilon) = f_{\alpha+\alpha_b}\sigma_{\alpha+\alpha_b}(\varepsilon) + f_{\gamma}(\varepsilon)\sigma_{\gamma}(\varepsilon) \qquad 2.1$$

Using the iso-strain model (equation 2.1), Jacques et al. [49] showed the importance of accounting for the transformation of retained austenite to martensite with deformation (Figure 2.8). The as-annealed microstructure of Medium Mn TRIP-assisted steels also

consist of ferrite, martensite and retained austenite [8], [15], [37], [38] due to which, composite strengthening would plays a role in the alloys global mechanical properties.

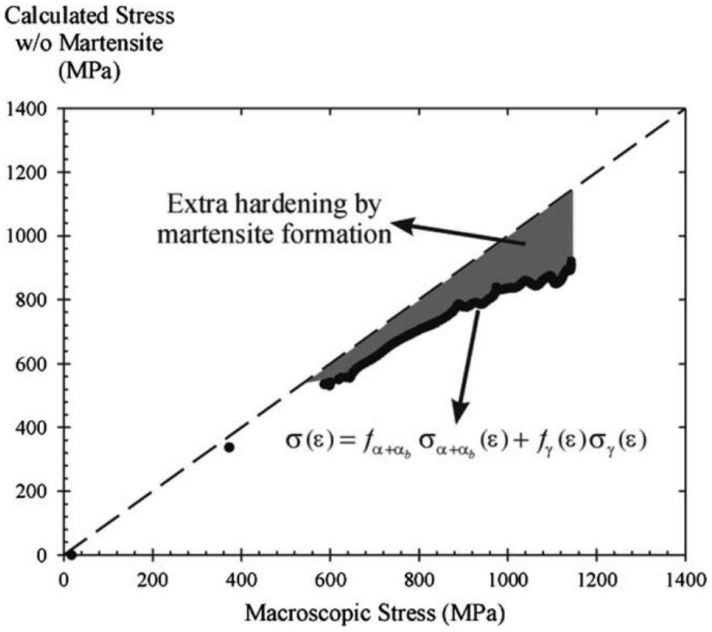

Figure 2.8: Iso-strain model showing the importance of accounting for the TRIP effect when modelling the macroscopic stress and strain [49].

2.5.3. TRIP Effect

Generally, improving a material's strength results in a reduction of the material's toughness and ductility [49]. The TRIP effect helps sustain a high work hardening rate, delaying the onset of necking resulting in a greater balance of strength and ductility. During the TRIP effect, chemically stable retained austenite gradually transforms to martensite upon deformation. This improves the strain hardening by (1) the dynamic formation of hard martensite particles, resulting in higher fractions of hard particles and a continuous increase in composite strengthening and (2) increasing in the dislocation density in the surrounding

ferrite grains to accommodate the volume expansion associated with the retained austenite to martensite transformation (Figure 2.9) [49] .

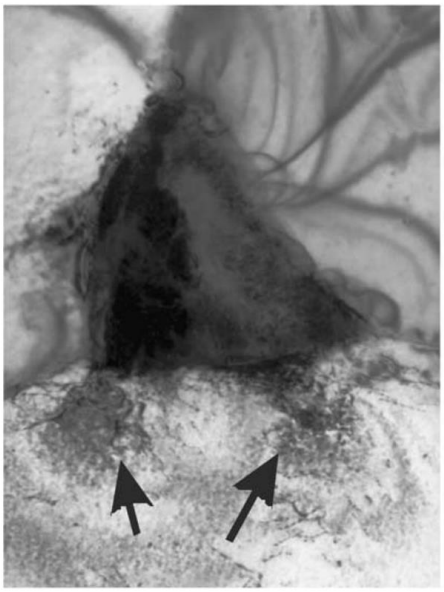

Figure 2.9: Bright Field (BF) image of 0.3C-1.4Mn-1.4Si alloy showing an increase in dislocation density in ferrite neighbouring retained austenite that transformed to martensite [51].

McDermid et al. [52] showed that the transformation of retained austenite to martensite is stress-, not strain-, induced when the temperature is above the stress required to initiate martensitic transformation equals the yield strength of the retained austenite (M^{σ}_{S} temperature). Olson and Cohen's [53] strain-induced transformation model required large variations in fitting parameters based on alloy composition and thermal processing history. The model proposed by McDermid et al. [52] used normalized flow stress and, modelled the transformation accurately without the need of numerous fitting parameters used in the strain-induced model.

2.5.4. TWIP Effect

Medium Mn steels are usually referred to as TRIP steels, however, in some cases, authors have shown deformation twinning occurring prior to the deformation induced transformation of retained austenite to martensite [11], [12]. The activation the TWIP effect is dependant upon the stacking fault energy (SFE) of the retained austenite. The composition of retained austenite dictates the stacking fault energy, the target intrinsic SFE for TWIP steels lies between 15 mJ/m^2 to 45 mJ/m^2 [54], [55]. The SFE is a strong function of alloy composition, namely, Mn, Al, Si, Cr, C and/or N [54]. The work hardening rate increases with the activation of twin formation with deformation [56]. Allain et al. [57] showed that when the SFE of a fully austenitic TWIP steel (0.6C-22Mn) was 20 mJ/m^2 a high work hardening rate was maintained through twinning induced plasticity. At higher SFE, twinning of the austenite grains was supressed. For SFE less than 18 mJ/m^2, deformation induced transformation of retained austenite to ε-martensite occurred [57]. Formation of twins results in the decrease of the mean free path, resulting in an increase in work hardening rate. Twin boundaries are strong obstacles to dislocation motion and become sites of dislocation accumulation; this effect is widely known as the dynamic Hall-Petch Effect [58].

Lee et al. [12] investigated two medium Mn steels, 0.15C/0.3C-6Mn-1.5Si-3Al and selected an IAT of 780°C, based on Lee and De Cooman‘s [9] previous work, where they showed the best mechanical properties were obtained from samples intercritically annealed at temperatures slightly below the IAT at which the maximum amount of retained austenite was stabilized [9] and obtained a retained austenite SFE of 20 mJ/m^2, known to result in

twin formation in retained austenite in high Mn fully austenitic steels 0.3C-6Mn-1.5Si-3Al alloy (1150 MPa × 60% TE) exhibited superior mechanical properties to a 0.6C-18Mn-3Al TWIP steel (976 MPa × 53% TE), which was attributed to the sample exhibiting a combination of the TRIP and TWIP effect.

2.6. Effects of Intercritical Annealing Parameters

Intercritical annealing parameters (temperature and holding times) dictates the amount of intercritical austenite that will form. The objective during this stage of the thermal processing cycle is to maximize the amount of chemically stable retained austenite at room temperature that will gradually transform to martensite upon deformation, which will allow the samples to maintain a high work hardening rate, resulting in an excellent balance of strength and ductility. The chemically stability of retained austenite is dictated by the partitioning of C and Mn into the austenite during intercritical annealing. The morphology and the size of retained austenite govern its stability. Lee et al. [34] intercritically annealed a 0.05C-6.15Mn-1.4Si alloy from the cold rolled state at 680°C for 180 s and 24 h and showed that the Mn content of retained austenite can reach near equilibrium values for short IAT holding times [34].

The IAT temperature and holding time affect the amount of intercritical austenite that forms and provide the energy required for partitioning of alloying elements; therefore, these two factors dictate the stability of retained austenite in the as-annealed microstructure. The retained austenite stability determines the rate of transformation of retained austenite to martensite with deformation. Researchers studying medium Mn steels showed that samples intercritically annealed at low IATs resulted in very stable retained austenite that

did not exhibit the TRIP effect during deformation. Increasing the IAT resulted in the retained austenite exhibiting gradual transformation to martensite with deformation resulting in the greatest balance of strength and ductility. Further increasing the IAT resulted in very unstable retained austenite that rapidly transformed to martensite with deformation which resulted in a high UTS but limited ductility [15], [37], [38]. The optimal IAT corresponded with the results obtained by Lee et al. [9], who suggested that the greatest balance of strength and ductility was obtained at a temperature slightly less than the temperature at which the greatest amount of retained austenite was obtained in the as-annealed microstructure [9].

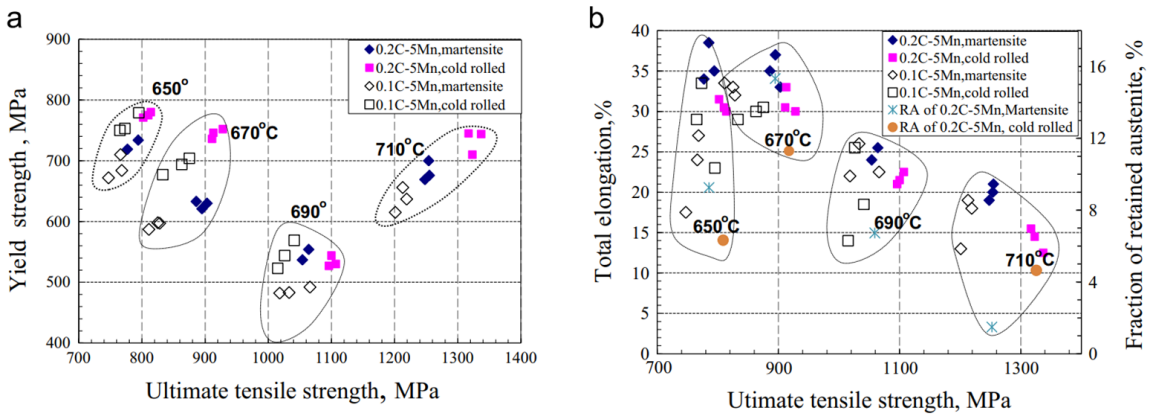

Figure 2.10: Mechanical properties of 0.1C-5Mn and 0.2C-5Mn alloys as a function of starting microstructures and IAT on (a) YS and UTS and (b) TE, UTS and fraction of retained austenite [38].

Luo shows the evolution of YS and UTS with IAT in Figure 2.10(a). As IAT was increased the UTS increased. As the IAT increased, the volume fraction of retained austenite simultaneously increased, which transformed to martensite upon deformation.

The formation of increased martensite resulted in an increase in the UTS. With increasing IAT, a reduction in YS was observed (Figure 2.10(a)). Luo suggested that the YS was dependant on the YS of ferrite (being the softest phase). With increasing IAT, the was greater partitioning of C and Mn from ferrite to retained austenite, resulting in a decrease in YS of ferrite. Moreover, this resulted in fewer C atoms being available to lock dislocations by forming a Cottrell atmosphere, resulting in a reduction in YPE. At an IAT of 710 C, the matrix consisted of a great volume fraction of martensite, which would isolate the ferrite grain, therefore, yielding would be dictated by the other phases (martensite and retained austenite) resulting in an increase in YS [38]. Steineder et al. [37] also observed decreasing YS with increasing IAT but attributed the reduction of YS to the loss of chemical stability of retained austenite, which would yield and begin transforming to martensite at lower stresses. Additionally, Steineder et al. [37] also observed an increase in YS at the highest IAT, which was attributed to self tempering of the martensite during cooling [37]. The micrographs also showed a significant decrease in ferrite content, giving merit to Luo's [38] proposed mechanism by which the YS increases. Figure 2.10(b) shows a decrease in TE with increasing IATs. Luo [38] observed a greater volume fraction of ferrite present in as-annealed microstructures at lower IATs. Ferrite being a soft and ductile phase would explain the greater ductility exhibited by samples intercritically annealed at lower temperatures. With increasing IAT, there was a reduction in the stability of retained austenite, resulting in faster transformation of retained austenite to martensite, which would increase the work hardening rate but would not be sustained due to the rapid transformation, resulting in a reduction of TE [38].

2.7. Fracture Mechanisms

Steineder et al. [59] studied the damage behaviour of a 0.1C-6Mn alloy intercritically annealed for 8 h, where the resultant fracture surfaces are shown in Figure 2.11. At an IAT of 580°C (Figure 2.11(a)) and 620°C (Figure 2.11(b)), the microstructure contained ferrite and martensite while the fracture surfaces exhibited a dimpled surface suggesting ductile fracture. At an IAT of 680°C (Figure 2.11(c)), the predominant fracture mode was cleavage fracture with a small amount of ductile fracture.

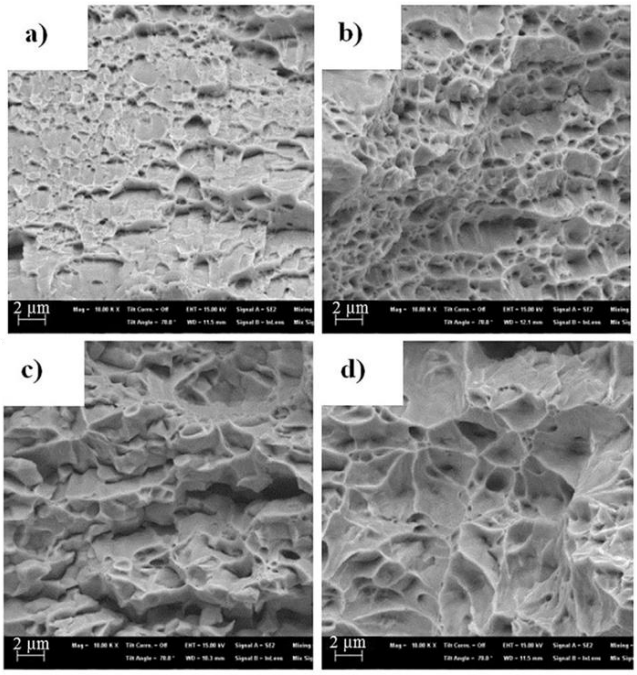

Figure 2.11: Fracture surfaces of 0.1C-6Mn alloy intercritically annealed from the TM starting microstructure at and IAT of (a) 580°C; (b) 620°C; (c) 680°C and (d) 700°C [59].

The as-annealed microstructure consisted of ferrite, martensite and retained austenite; where the reduced ductility was attributed to the low chemical stability of the retained austenite and the presence of martensite. Further increasing the IAT to 700°C

(Figure 2.11(d)) resulted in quasi-cleavage fracture surface alongside larger dimples (compared to the samples intercritically annealed at 580°C and 620°C). These fracture mechanisms were consistent with those observed by Sun et al. [60] who investigated an 0.2C-10Mn-3Al alloy. The as-annealed microstructure consisted of ferrite, retained austenite, martensite and tempered martensite. As the IAT was increased, a greater amount of intercritical austenite formed, resulting in dilution of the alloy content, namely C and Mn in retained austenite. This reduction in alloy content in retained austenite increased the M_s temperature and resulted in tempering of the martensite as the samples were cooled. The presence of tempered martensite changed the fracture mode from cleavage fracture to quasi-cleavage fracture alongside micro-void coalescence.

Steineder et al. [59] proposed that micro-void nucleation was initiated at the interface between ferrite and harder phases as a result of stress localization arising from the disparity in hardness between the phases in the case of samples intercritically annealed at 580°C (Figure 2.12(a)) and 620°C (Figure 2.12(b)). For samples intercritically annealed at 680°C, where fresh martensite was present in the microstructure, voids were formed by cracking of the hard martensite particles or due to decohesion between ferrite and martensite. For samples intercritically annealed at 700°C, there was less disparity of hardness between fresh and tempered martensite resulting in void nucleation occurring at these interfaces [59].

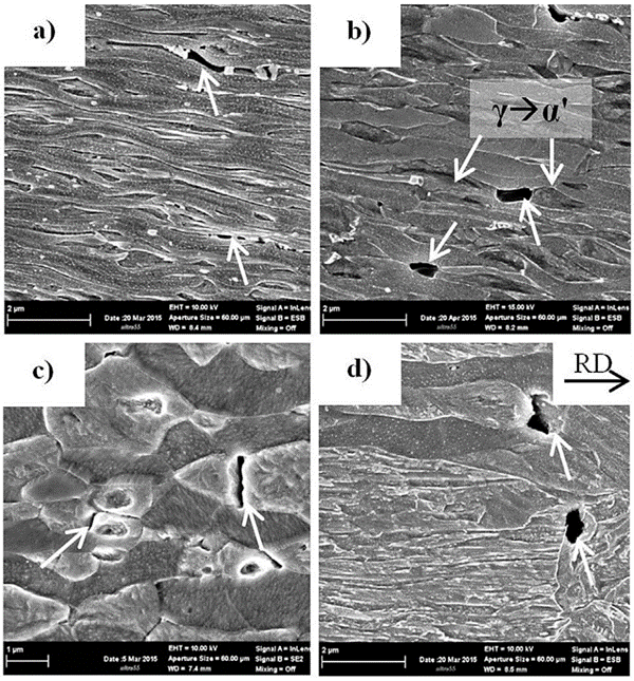

Figure 2.12: Cross sections of 0.1C-6Mn alloy intercritically annealed from the TM starting microstructure at and IAT of (a) 580°C; (b) 620°C; (c) 680°C and (d) 700°C [59].

Chapter 3: Research Objectives

As was demonstrated in Chapter 2, the final microstructure and mechanical properties of medium Mn TRIP-assisted steels are heavily influenced by the starting microstructure and subsequent thermal processing cycle. Numerous researchers studying medium Mn steels have obtained excellent mechanical properties that meet the target 3G-AHSS mechanical property envelope, however, employ intercritical annealing temperatures (IATs) and/or holding times incompatible with existing continuous galvanizing lines (CGLs) [12], [15], [37], [38], [61]. The objective of the research is to develop a thermal processing cycle for a prototype medium Mn TRIP-assisted steel compatible with existing CGL infrastructure that produces the desired microstructure and results in a combination of strength and tensile elongation that meets the 3G-AHSS mechanical property targets. To this end, the objectives of this research are:

- Develop a CGL-compatible thermal profile for a prototype medium Mn TRIP-assisted steel
- Determine the effects of intercritical annealing parameters (IAT and holding time) and starting microstructure on the as-annealed microstructure and mechanical properties
- Assess the mechanical properties with respect to the target 3G-AHSS mechanical property envelope

Chapter 4: Experimental Methods

4.1. Experimental Steel Fabrication and Chemical Analysis

The experimental alloy was fabricated at U.S. Steel R&D (Munhall, Pennsylvania) by vacuum melting, slab casting, hot rolling, pickling and cold rolling to a final thickness of 1.2 mm. The experimental alloy was cast, heated to 1250°C and hot rolled to 25 mm with a finish temperature of 1050°C and slow cooled in vermiculite. The ingots were then reheated to 1250°C and hot rolled to 4 mm, the finishing temperature was 900°C. Dilatometry samples (2 mm ø × 10 mm) were machined from the hot rolled structure. The steel was annealed at 665°C for 2 h, ground to 2.7 mm, followed by cold rolling to a final thickness of 1.2 mm. The composition of the steel was determined by Inductively Coupled Plasma-Optical Emission Spectroscopy (ICP-OES) using the Vista-PRO ICP-OES. Carbon and sulphur (C&S) analysis was carried out using a Leco CS-444 Carbon/Sulfur Determinator. The composition of the experimental steel, as determined using the above techniques, is given in Table 4.1.

Table 4.1: Chemical composition of the experimental 3G-AHSS (wt.%).

C	Mn	Al	Si	S	Mo	Ti
0.15	5.56	0.99	1.17	0.003	0.073	0.011

The as-received microstructure comprised of highly deformed tempered martensite, ferrite and carbides (denoted TM), shown in Figure 4.1(a). As discussed in Chapter 2

previous workers have shown that the starting microstructure has a significant effect on the austenite reversion kinetics, where a martensitic starting microstructure favours more rapid austenite formation [38][8]. In order to determine the effect of starting microstructure for the present experimental steel, a fully martensitic structure (denoted M), shown in Figure 4.1(b) was obtained by heating the sample to 900°C and holding for 600 s before gas quenching to room temperature at a rate of -20 °C/s. Microstructural analysis by scanning electron microscopy (SEM) confirmed that it was a fully martensitic structure. X-ray Diffraction (XRD), showed that there were no detectable amounts of retained austenite present in either of the starting microstructures, shown in Figure 4.2. Parameters used for XRD data acquisition can be found in §4.6.2. X-Ray Diffraction (XRD). Figure 4.2 also contains an XRD pattern for a sample intercritically annealed at 710°C for 120 s from the TM starting microstructure. Heat treated samples were identified starting with the alloy name, steel D, shortened to “D”, followed by the starting microstructure it was annealed from, either “TM” or “M”. The last two numbers correspond to the IAT (°C) and IAT holding time (s) respectively.

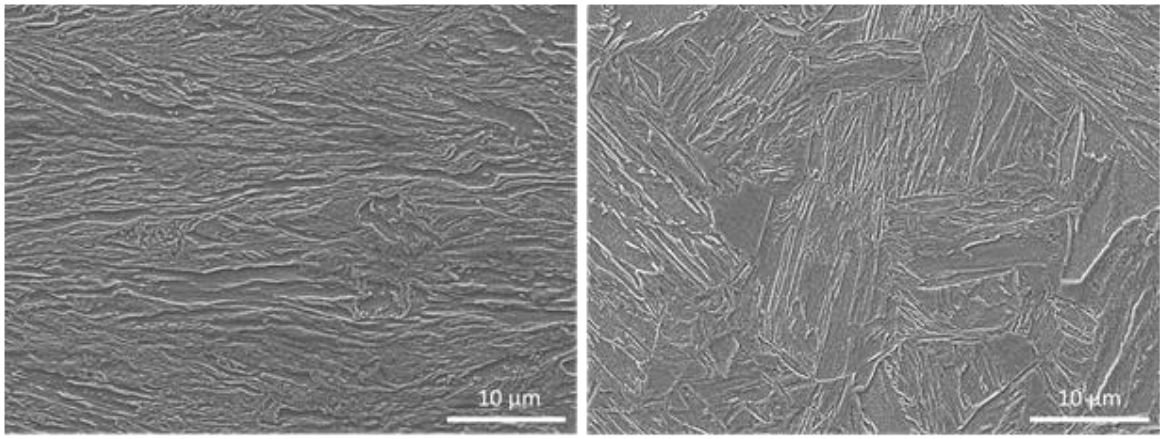

Figure 4.1: SEM images of (a) tempered martensitic (TM) starting microstructure and (b) fully martensitic (M) starting microstructure.

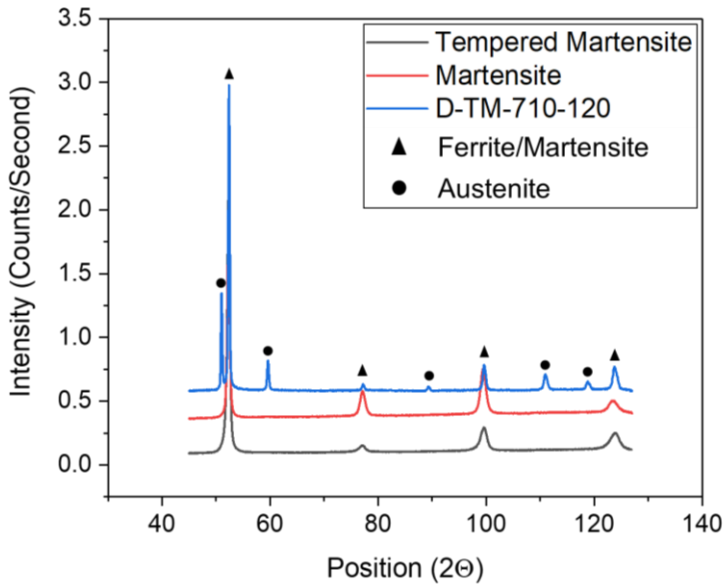

Figure 4.2: X-ray diffraction pattern of the two starting microstructures (tempered martensite and fully martensite) and a sample annealed from the TM starting microstructure at 710°C for 120 s.

Two sample geometries were used to investigate the microstructural and mechanical property development of the alloy. Coupons measuring 10 mm (transverse direction, TD) × 50 mm (rolling direction, RD) were annealed for Scanning Electron Microscopy (SEM), X-Ray Diffraction (XRD) and Transmission Electron Microscopy (TEM) microstructural analysis. Based on microstructural analyses, promising heat treatments that contained significant fractions of chemically stable retained austenite were selected for mechanical testing. Mechanical testing coupons consisted of 120 mm × 200 mm panels, from which sub-size tensile samples conforming to ASTM E8 [62] (with the tensile direction along the RD) were cut by Electric Discharge Machining (EDM). To determine the area within the mechanical testing coupons that had the least temperature variations during the heat treatment, named the uniform heated zone, Rockwell hardness tests according to ASTM E18 [63] were conducted in 1 cm increments. The variations in hardness were assumed to correspond to variations in temperature during annealing. A contour plot for the hardness results for sample D-M-690-240 is shown in Figure 4.3(a). The uniform heated zone was a 90 mm × 90 mm area 50 mm from the top of the mechanical testing coupons, shown in Figure 4.3(b). Sub-sized tensile specimens were machined from within this zone to ensure samples were subject to an uniform temperature profile.

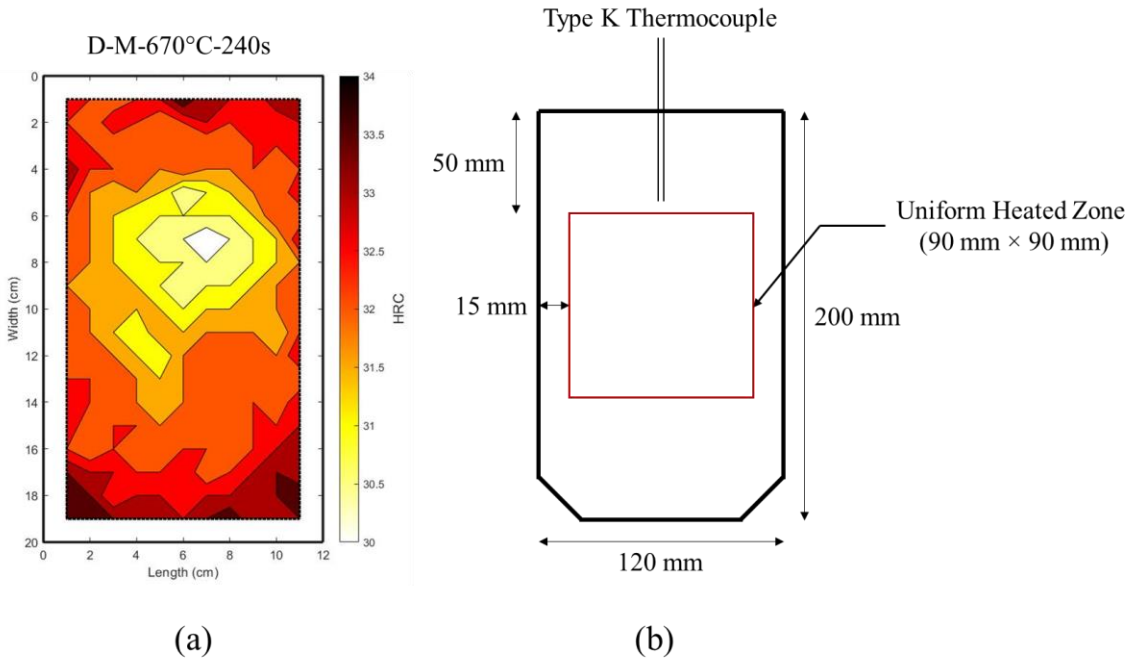

Figure 4.3: (a) Contour plot showing the variation in hardness across the mechanical testing coupon and (b) Schematic of uniform heated zone location on mechanical tests coupons [64].

4.2. McMaster Galvanizing Simulator

All heat treatments were conducted in the McMaster Galvanizing Simulator (MGS) shown in Figure 4.4(a). Going top down, the MGS consists of a sample loading and cooling section, below which resides the quartz-tube infrared (IR) furnace followed by a high frequency induction furnace, all of which have atmosphere control. The heat treatments were performed in the IR furnace. The thermal cycle was controlled using a 0.5 mm K-type thermocouple welded to a dummy sample in the case of the smaller heat treatment samples and directly to the larger panel for the tensile coupons. The annealing atmosphere consisted of a N_2-5% H_2 gas mixture at a dew point of -30°C, where the process atmosphere dew

point within the MGS is controlled by a dew point control system, shown in Figure 4.4(b), that mixes a water-saturated stream of gas with a dry stream in the appropriate ratio.

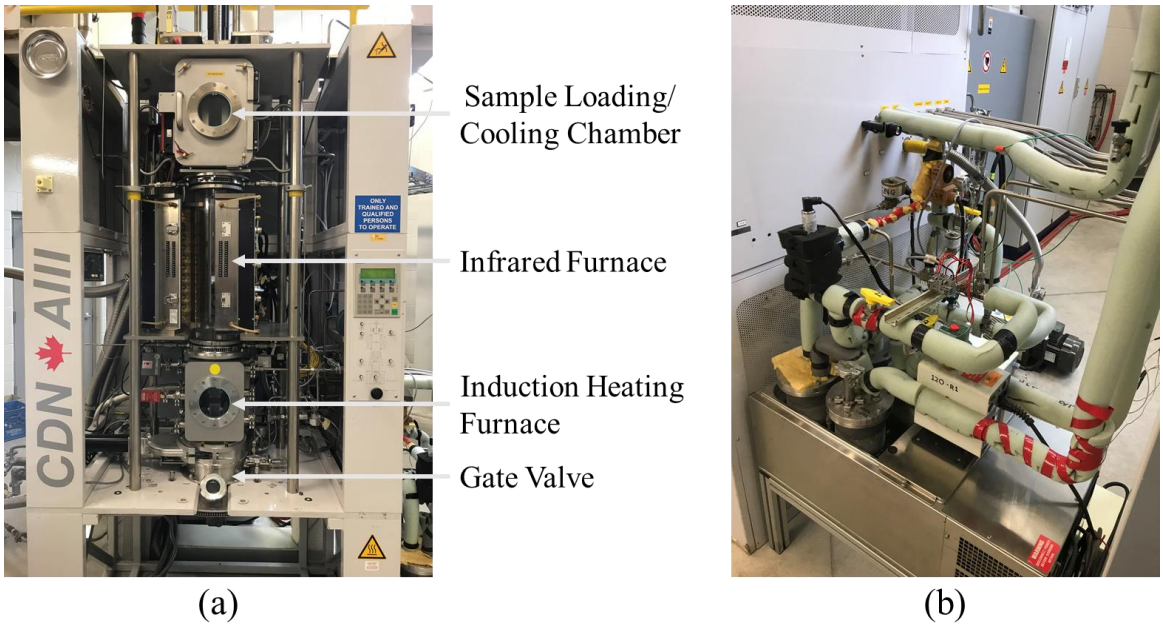

Figure 4.4: (a) McMaster galvanizing simulator (MGS) and (b) dew point control system.

4.3. Dilatometry

To determine the transformation temperatures of the experimental alloy and the austenite reversion kinetics, dilatometry experiments were conducted at CanmetMATERIALS (Hamilton, Canada). Samples measuring 3 mm (diameter) × 10 mm (length) were heated up to 1000 °C using heating rates of 5 °C/s, 10 °C/s and 15 °C/s and a cooling rate of 20 °C/s to room temperature. The dilation vs. temperature curves, an example of which is shown in Figure 4.5(a), were analyzed to determine the Ac_1, Ac_2, Ac_3, M_s and M_f temperatures. It was found that the transformation temperatures were not strongly dependant on heating rate.

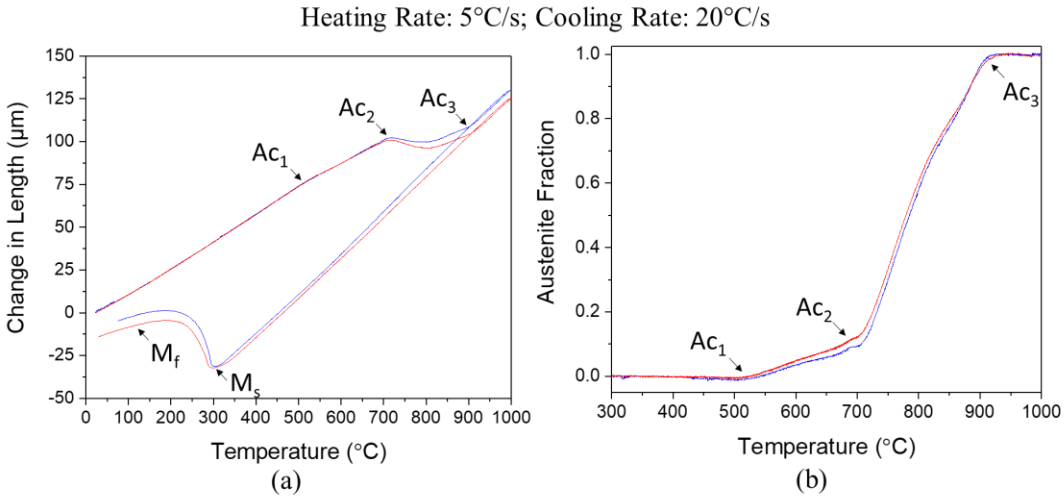

Figure 4.5: Dilatometry results (a) the change in length as a function of temperature and (b) the volume fraction of austenite as a function of temperature.

4.4. Iron-Carbon Phase Diagram

Thermo-Calc Software and Fe-alloys Database (TCFE 6) was used to create an iron-carbon phase diagram for the alloy, shown in Figure 4.6(a). From the phase diagram, the partitioning of C into austenite was calculated under equilibrium conditions as a function of temperature, shown in Figure 4.6(b). Based on Figure 4.5(b) and Figure 4.6(b), a series of intercritical annealing temperatures were selected. An IAT of 740°C was selected that corresponded to a 0.25 volume fraction austenite (Figure 4.5(b)) and IATs of 690°C and 720°C which had increasing C content of austenite based on Figure 4.6(b).

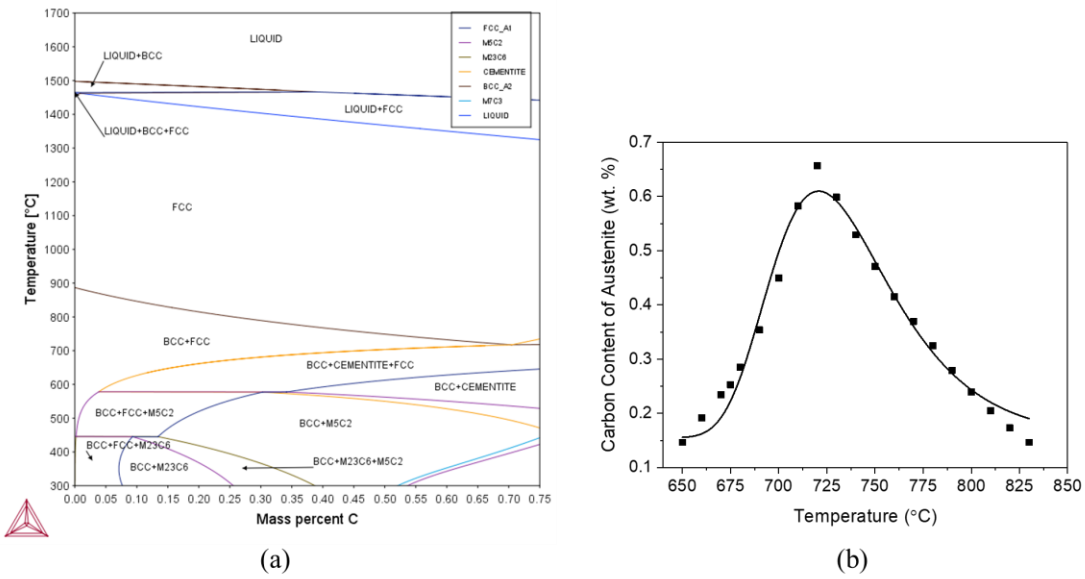

Figure 4.6: (a) Iron-carbon phase diagram for the experimental alloy and (b) carbon content of austenite as a function of temperature.

4.5. Thermal Processing Cycle

Based on the dilatometry results and taking into consideration the constraints of industrial galvanizing lines (limiting temperatures, holding times, cooling and heating rates), a two-stage thermal processing cycle was developed, as seen in Figure 4.7. The intercritical annealing temperature (IAT) and the IAT holding time was varied to determine the amount of chemically stable retained austenite in the room temperature microstructure. Typically, IAT holding times of 60 s to 120 s are used industrially, with 240 s being marginally compatible with conventional CGLs but longer holding times were also investigated to better determine the austenite reversion kinetics. The 30 s hold at 460°C simulates both the equilibration with the Zn(Al,Fe) bath and the actual dipping step (as the bath would also be held at approximately 460°C). Finally, the sample was cooled to room

temperature at a rate of -20°C/s. IATs of 690°C, 710°C, 720°C and 740°C were used for the tempered martensite starting structure whereas IATs of 670°C, 690°C, 710°C, 720°C and 740°C were used for the martensite starting microstructure. Table 4.2 summarizes the experimental matrix.

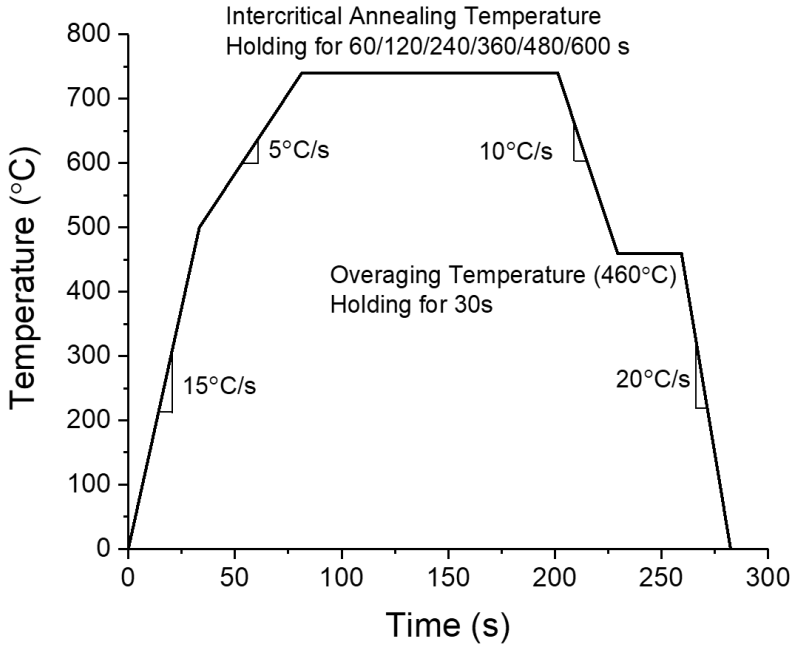

Figure 4.7: Schematic of the thermal processing cycle.

Table 4.2 Summary of IATs, IAT holding time and OT condition for annealing the experimental alloy.

Sample ID	IAT (°C)	IAT Holding Time (s)	Overaging Conditions
TM	690	60, 120, 240, 360, 480, 600	460°C for 30 s
	710		
	720		
	730		
	740		
M	670	60, 120, 240, 360, 480, 600	460°C for 30 s
	690		
	710		
	720		
	740		

4.6. Analysis Techniques

4.6.1. Scanning Electron Microscopy (SEM)

Microstructural images were taken on a JEOL JSM-7000F using an acceleration voltage of 10 keV and a working distance of 10 mm. Samples were mounted in epoxy and prepared using standard metallographic techniques with 1 μm diamond suspension used as the final polishing step. The samples were etched with 4% nitric acid in anhydrous ethanol (4 % Nital). Images of fracture surfaces after uniaxial tensile tests were taken on a JEOL 6610-LV using an acceleration voltage of 5 keV and a working distance of 20 mm.

4.6.2. X-Ray Diffraction (XRD)

Two-dimensional X-ray diffraction (XRD^2) was used to measure the volume fraction of retained austenite and estimate the C content of the retained austenite of thermally treated samples. After the 10 mm × 50 mm coupons were annealed, cross sections from the centre of the specimen were mounted in epoxy and ground using a final step of 1200 grit SiC paper. A cobalt (Co) source ($\lambda = 1.79026$ Å) Bruker D8 DISCOVER with a DAVINCI.DESIGN diffractometer was used to collect data. The Vantec 500 (MiKroGap TM Technology) area detector was set 20 cm away from the sample. The collimator and slit size were both 0.5 mm. Four frames were acquired per sample (600 s exposure time per frame) from a 2θ range of 37° to 115° at 19° increments. The acquired frames were integrated from 45° to 127° using DIFFRAC.EVA software (Bruker AXS Inc.) and imported into DIFFRAC.TOPAS (Bruker AXS Inc.). Rietveld refinement was performed in TOPAS according to the ASTM E 975 standard to calculate the volume fraction of retained austenite in the samples [65]. ASTM E 975 uses the austenite (111), (200) and (220) peaks and the ferrite (110), (200) and (211) peaks. Martensite was also present in the microstructure so the martensite (200), (112) and (211) peaks were also utilized. From the retained austenite lattice parameter calculated in TOPAS, the C content of the retained austenite was calculated from equation 4.1, which is a combination of the Ruhl and Cohen equations for the effects of Mn, Si and C [66] and Dyson and Holmes equation for Al [67] on the austenite lattice parameter.

$$a = 3.572 + 0.0012(\text{wt.\%Mn}) - 0.00157(\text{wt.\%Si}) + 0.0056(\text{wt.\%Al}) + 0.033(\text{wt.\%C})\text{Å} \quad 4.1$$

where a is the lattice parameter in Å and the remaining terms are related to the composition of the retained austenite. The Mn, Al and Si contents were assumed to be equal to the bulk composition.

4.6.3. Transmission Electron Microscopy (TEM)

TEM foils were prepared by mechanically grinding samples obtained from coupons and the gauge length of strained samples to a thickness of 80 μm and subsequently punching 3 mm discs. Twin jet electropolishing was performed using a Struers TenuPol-5 using a voltage of 25 V and an electrolyte containing 10 % perchloric acid and methanol at -35°C. Fine scale microstructural analysis to determine the phase distribution and morphology was performed on a PHILIPS CM12 with an acceleration voltage of 120 KeV. Selected Area Diffraction (SAD) was conducted to identify the phases present based on their crystal structures and lattice parameters. SAD patterns were obtained using a camera constant of 180 mm. The diffraction patterns for ferrite and austenite were indexed using crystallographic information files (CIF) from the Inorganic Crystal Structure Database (ICSD), the ID numbers were 41506 and 53802 respectively [68]. Bright field and dark field images were obtained at areas of interest on the samples.to observe phase distributions and investigate the presence of deformation twins formed in retained austenite.

4.6.4. Uniaxial Tensile Tests

Uniaxial tensile tests were conducted for selected heat treatments that yielded interesting volume fractions of chemically stable retained austenite, as determined from the XRD results. ASTM E8 [62] sub sized tensile specimens were cut from 120 mm × 200 mm panels annealed in the MGS using electric discharge machining (EDM), where the sample

gauge lengths were taken from the 90 mm × 90 mm uniform temperature zone on the panels (Figure 4.3). All tests were performed at room temperature using a cross head speed of 1 mm/min on an Instron 100 kN servohydraulic tensile frame with a conventional extensometer attached within the gauge length of the tensile specimens. Specimens pulled to fracture were conducted in triplicates while only a single specimen was used for the interrupted tensile tests. Work hardening curves for the samples tested to fracture were constructed by taking the derivative of the plastic portion of the true stress – true strain curves and smoothing the curves to reduce the noise.

Chapter 5: Results

5.1. X-ray Diffraction on As-Annealed Samples (XRD)

The volume fraction of retained austenite and its calculated C content were determined as a function of intercritical annealing temperature (IAT), IAT holding time and starting microstructure (i.e. tempered martensite (TM) or martensitic (M)), shown in Figure 5.1.

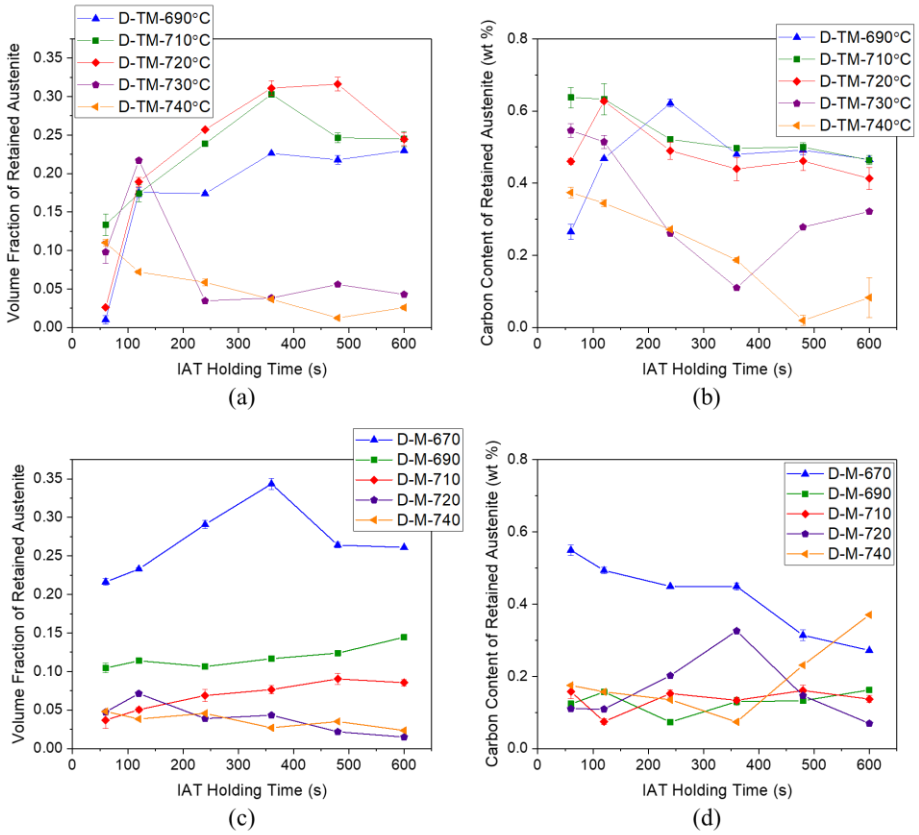

Figure 5.1: Volume fraction of retained austenite for samples intercritically annealed from: (a) TM starting microstructure, (b) M starting microstructure and carbon content of

retained austenite for samples intercritically annealed from: (c) TM starting microstructure and (d) M starting microstructure as a function of IAT and IAT holding times.

The volume fraction of retained austenite and its calculated C content as a function of IAT and IAT holding time for the TM starting microstructure are shown in Figure 5.1(a) and Figure 5.1(b), respectively. The volume fraction of retained austenite for as-annealed samples intercritically annealed at 690°C gradually increased with increasing IAT holding times up to 360 s after which the volume fraction of retained austenite remained constant at 0.22 to the 600 s IAT time (Figure 5.1(a)). The C content of the retained austenite, shown in (Figure 5.1(b)), increased with IAT time to a maximum of 0.6 wt.% C for the IAT holding time of 240 s and decreased to 0.5 wt.% C for longer IAT holding times. Samples intercritically annealed at 710°C peaked at 0.30 volume fraction retained austenite after an IAT holding time of 360 s, dropping to retained austenite volume fractions of 0.25 for longer IAT holding times (Figure 5.1(a)). Samples intercritically annealed at 720°C peaked at 0.30 volume fraction retained austenite after an IAT holding time of 480 s and dropped to 0.20 volume fraction retained austenite after an IAT holding time of 600 s (Figure 5.1(a)). The C content of retained for samples intercritically annealed at 710°C and 720°C did not show a significant change with increasing IAT holding times and was relatively constant at 0.50 wt.% C (Figure 5.1(b)). Samples intercritically annealed at 730°C had a peak retained austenite volume fraction of 0.22 after an IAT holding time of 120 s, after which there was a sharp drop in retained austenite content (Figure 5.1(a)). At an IAT of 730°C, the C content of retained austenite gradually decreased with increasing IAT holding

time (Figure 5.1(b)), which suggests that the C content of intercritical austenite dilutes for longer IAT holding times, resulting in reduced stability of intercritical austenite. For samples intercritically annealed at 740°C, the volume fraction of retained austenite was approximately 0.10 after 60 s and gradually decreased with increasing IAT holding time (Figure 5.1(a)). The C content of the retained austenite also steadily declined with increasing IAT holding time (Figure 5.1(b)). This suggests that an IAT of 740°C was too high and formed chemically unstable retained austenite.

The volume fraction of retained austenite and its calculated C content as a function of IAT and IAT holding time for the M starting microstructure are shown in Figure 5.1(c) and Figure 5.1(d), respectively. The volume fraction of retained austenite was below 0.10 for all IAT holding times for IATs of 710°C, 720°C and 740°C (Figure 5.1(c)). The volume fraction of retained austenite increased with increasing IAT holding times up to 360 s for the IAT of 670°C, peaking at 0.35 (Figure 1.1(c)). The C content of the retained austenite decreased marginally with increasing IAT holding times to 360 s, ranging between 0.45 to 0.55 wt. % C, followed by a more significant drop (0.3 wt.% C) in C content for longer IAT holding times (Figure 5.1(d)). Samples annealed at an IAT of 690°C showed a marginal increase in the volume fraction of retained austenite with increasing IAT holding times, increasing from 0.1 after 60 s to 0.15 after an IAT holding time of 600 s (Figure 5.1(c)).

Isochronal sections from samples intercritically annealed from the TM starting microstructure show the effect of the IAT on the volume fraction and C content of retained austenite in Figure 5.2.

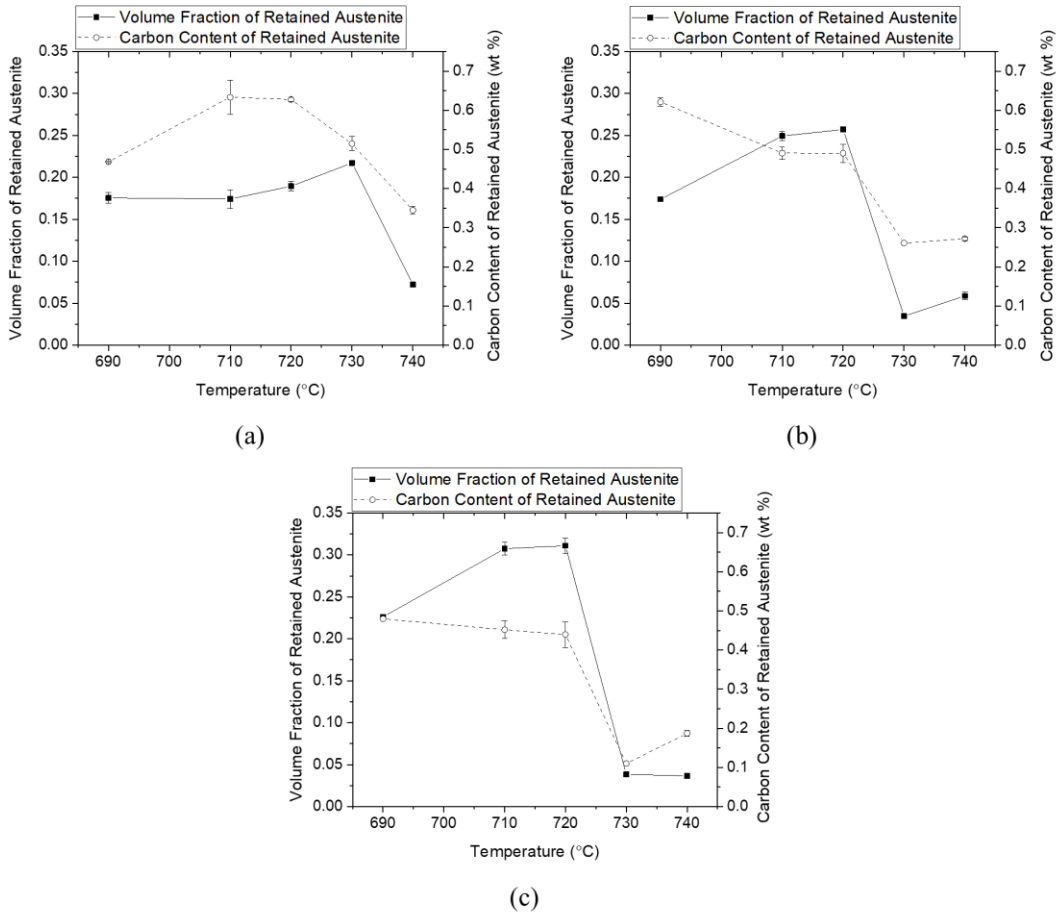

Figure 5.2: Volume fraction and carbon content of retained austenite for samples annealed from the TM starting microstructure as a function of IAT for IAT holding times of (a) 120 s; (b) 240 s and (c) 360 s.

For an IAT holding time of 120 s, the retained austenite volume fraction gradually increased with increasing IAT up to 730°C, achieving 0.23 volume fraction of retained austenite (Figure 5.2(a)). The C content of retained austenite increased from 0.46 wt.% C to 0.64 wt.% C from the IAT of 690°C to 710°C and remained constant to 720°C (Figure 5.2(a)). At the IATs of 730°C and the 740°C the retained austenite C content decreased to 0.5 wt. % C and 0.35 wt. % C respectively. Moreover, at the IAT of 740°C the volume

fraction of retained austenite decreased to 0.15 (Figure 5.2(a)). Similarly, for the IAT holding time of 240 s, the volume fraction of retained austenite increased with increasing IAT (Figure 5.2(b)), increasing from 0.17 to 0.25 when the IAT was increased from 690°C to 710°C and remaining constant when the IAT was further increased to 720°C (Figure 5.2(b)). Increasing the IAT to 730°C and 740°C resulted in volume fractions of retained austenite below 0.07 (Figure 5.2(b)). The C content of retained austenite was 0.60 wt.% at an IAT of 690°C. The C content decreased to 0.5 wt.% when the IAT was increased to 710°C and 720°C and was further reduced to 0.27 wt.% for greater IATs i.e. 730°C and 740°C (Figure 5.2(b)). Further increasing the IAT holding time to 360 s (Figure 5.2(c)) resulted in similar trends to samples held for 240 s (Figure 5.2(b)). A volume fraction of 0.30 retained austenite was achieved at an IAT of 710°C and 720°C, the C content of the retained austenite remained stable at 0.45 wt.% (Figure 5.2(c)). At greater IATs, 730°C and 740°C, both the volume fraction of retained austenite was reduced to 0.03 and its C content was close to the global composition of the alloy, i.e. 0.15 wt.% C (Figure 5.2(c)).

Isochronal sections from samples intercritically annealed from the M starting microstructure show the effect of the IAT on the volume fraction and C content of retained austenite in Figure 5.3.

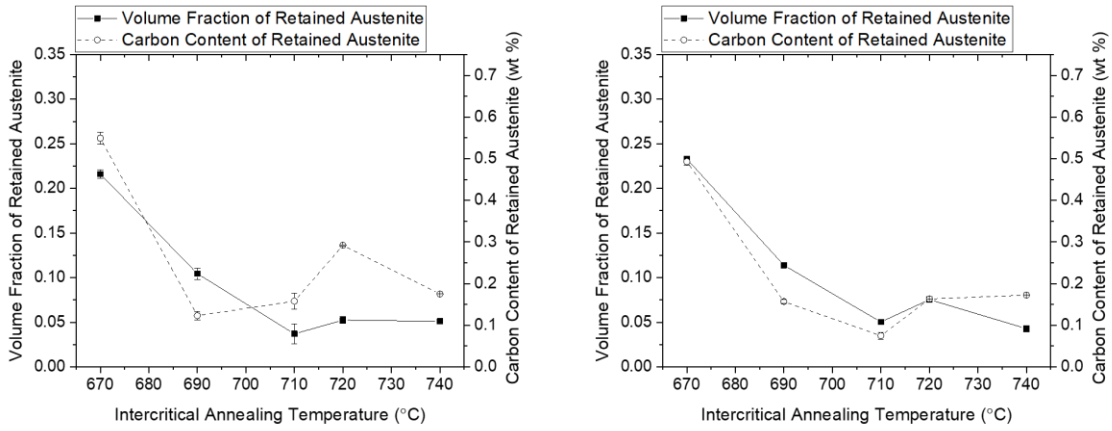

Figure 5.3: Volume fraction and carbon content of retained austenite for samples annealed from the M starting microstructure as a function of IAT for IAT holding times of (a) 60 s and (b) 120 s.

An IAT holding time of 60 s at the IAT of 670°C resulted in the highest volume fraction of retained austenite, 0.22 with the highest C content of 0.55 wt.% C (Figure 5.3(a)). At the IAT of 690°C, the volume fraction of retained austenite was approximately 0.10 and C content of the retained austenite was 0.15 wt.% C (Figure 5.3(a)). Further increasing the IAT resulted in barely detectable amount of retained austenite, under 0.05 volume fraction (Figure 5.3(a)). The IAT holding times of 60 s (Figure 5.3(a)) and 120 s (Figure 5.3(b)) showed similar trends, where the volume fraction and C content of retained austenite decreased with increasing IAT, independent of IAT holding times (Figure 5.3).

As-annealed samples from the M starting microstructure showed faster austenite reversion kinetics compared to samples annealed from the TM starting microstructure, requiring lower IATs and shorter holding times to achieve appreciable amounts of retained

austenite in the final microstructure (Figure 5.1). Volume fractions of retained austenite greater than 0.20 were observed in samples intercritically annealed at 670°C from the M starting microstructure for all holding times, achieving 0.33 volume fraction of retained austenite for the M-670-360 heat treatment (Figure 5.1(c)). On the other hand, as-annealed samples from the TM starting microstructure required IATs between 690°C to 730°C and holding times of at least 120 s to obtain volume fractions of retained austenite approaching 0.20 (Figure 5.1(a)).

The reduction of volume fraction of retained austenite in as-annealed samples with increasing IAT coincided with a decrease in the C content of the retained austenite. Increasing the IAT and/or IAT holding times resulted in a greater amount of intercritical austenite formation, and increasing the volume fraction of intercritical austenite diluted the C content of the austenite. This is consistent with the phase diagram for the experimental alloy and the C content of intercritical austenite shown in Figure 4.6(a). If the austenite contained an insufficient amount of C, which is an excellent austenite stabilizer [34], the austenite transformed to fresh martensite upon quenching and only a small volume fraction of retained austenite remained in the as-annealed microstructure. Based on the XRD data (Figure 5.1) mechanical testing coupons were fabricated for as-annealed samples from the TM starting microstructure for IATs of 690°C, 710°C, 720°C and 730°C and as-annealed samples from the M starting microstructure for IATs of 670°C, 690°C and 710°C.

5.2. Microstructural Characterization – SEM

Microstructural images for the as-annealed samples taken using a Scanning Electron Microscope (SEM) are presented in Figure 5.4 through Figure 5.13, where the as-annealed microstructures arising from the TM starting microstructure are documented in Figure 5.4 to Figure 5.8 and those from the M starting microstructure in Figure 5.9 to Figure 5.13. The phases present are labelled, where α = ferrite, γ = retained austenite and α' = martensite. The average grain size for the as-annealed microstructures from both the TM and M starting microstructures was 4 μm ± 0.9 μm. Thus, the heat treatments did not significantly affect the average grain size. The as-annealed microstructures from the TM starting microstructures comprised retained austenite/martensite and ferrite. The as-received TM starting microstructure, shown in Figure 4.1(a) consisted of tempered martensite and ferrite, where both phases were heavily deformed and elongated as a result of cold rolling.

Figure 5.4 shows as-annealed samples from the TM starting microstructure intercritically annealed at 690°C. The phases in the TM-690-60 microstructure (Figure 5.4(a)) show an elongated morphology, which suggests that the low IAT and short IAT holding time resulted in partial recrystallization. As the holding time was increased the size and volume fraction of the ferrite islands was reduced as well as a decrease in the aspect ratio of the retained austenite/martensite grains was observed, resulting in a more equiaxed microstructure (Figure 5.4 to Figure 5.8), suggesting more complete recrystallization occurred. A globular/equiaxed morphology of retained austenite is known to be less stable than lamellar retained austenite [15], [42].

The microstructure of as-annealed samples from the TM starting microstructure intercritically annealed at 710°C, 720°C, 730°C and 740°C are shown in Figure 5.5, Figure 5.6, Figure 5.7 and Figure 5.8, respectively. The as-annealed microstructures had a globular morphology and consisted of martensite, retained austenite and ferrite. Large ferrite islands were not observed in these micrographs, particularly at the higher IATs. (Figure 5.4 to Figure 5.8). Increasing the IAT and/or IAT holding time resulted in a greater amount of recrystallization of the TM starting microstructure, resulting in an equiaxed morphology of the as-annealed microstructure. Moreover, from the phase diagram shown in Figure 4.6, increasing the IAT results in a greater amount of intercritical austenite forms at the expense of ferrite (Figure 5.4 to Figure 5.8). This is consistent with the decrease in ferrite content observed in the as-annealed microstructures (Figure 5.4 to Figure 5.8).

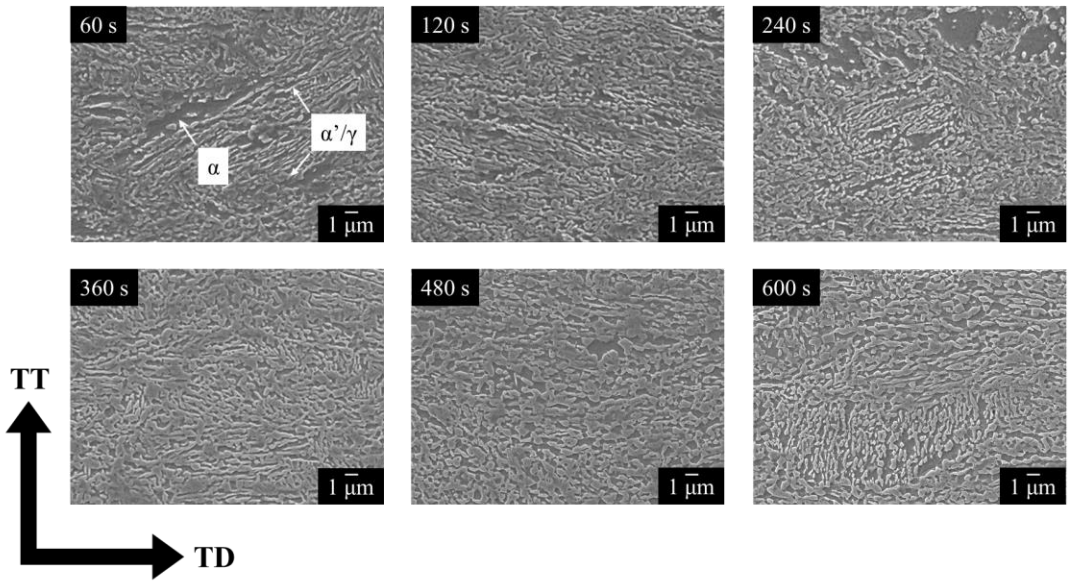

Figure 5.4: SEM micrographs of samples intercritically annealed at 690°C from the TM starting microstructure as a function of IAT holding time.

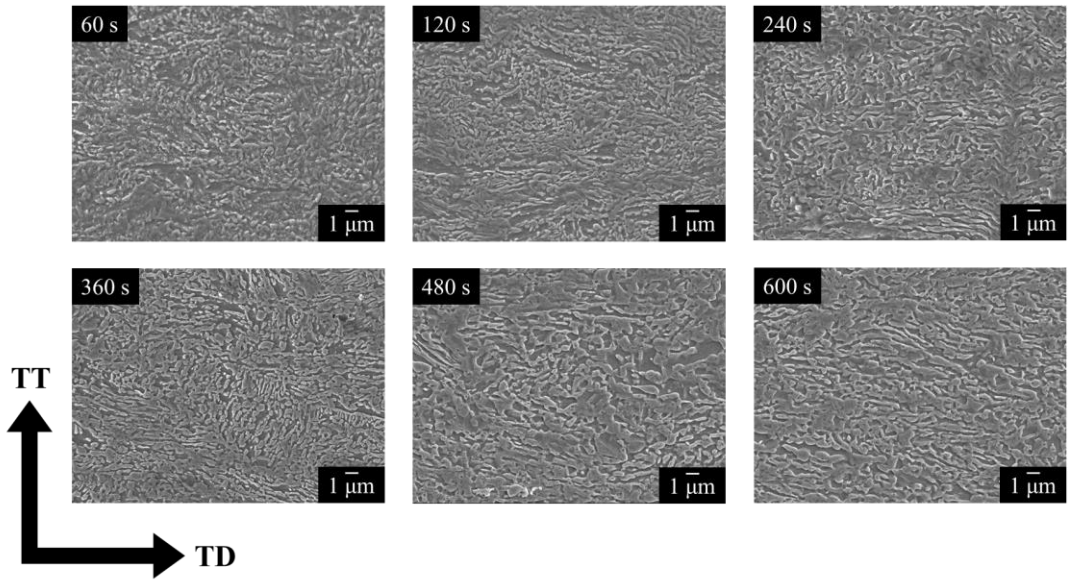

Figure 5.5: SEM micrographs of samples intercritically annealed at 710°C from the TM starting microstructure as a function of IAT holding time.

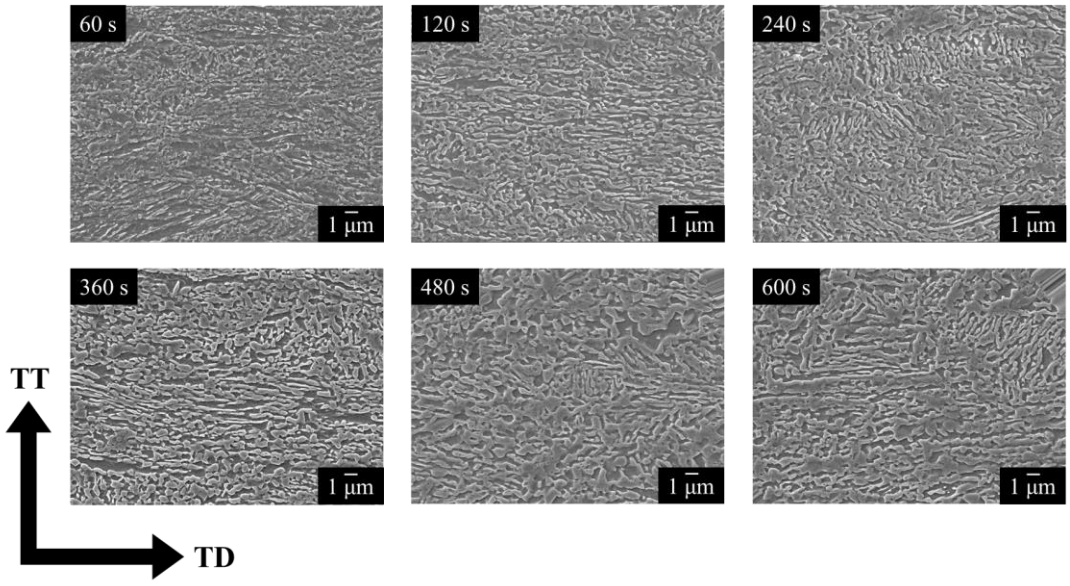

Figure 5.6: SEM micrographs of samples intercritically annealed at 720°C from the TM starting microstructure as a function of IAT holding time.

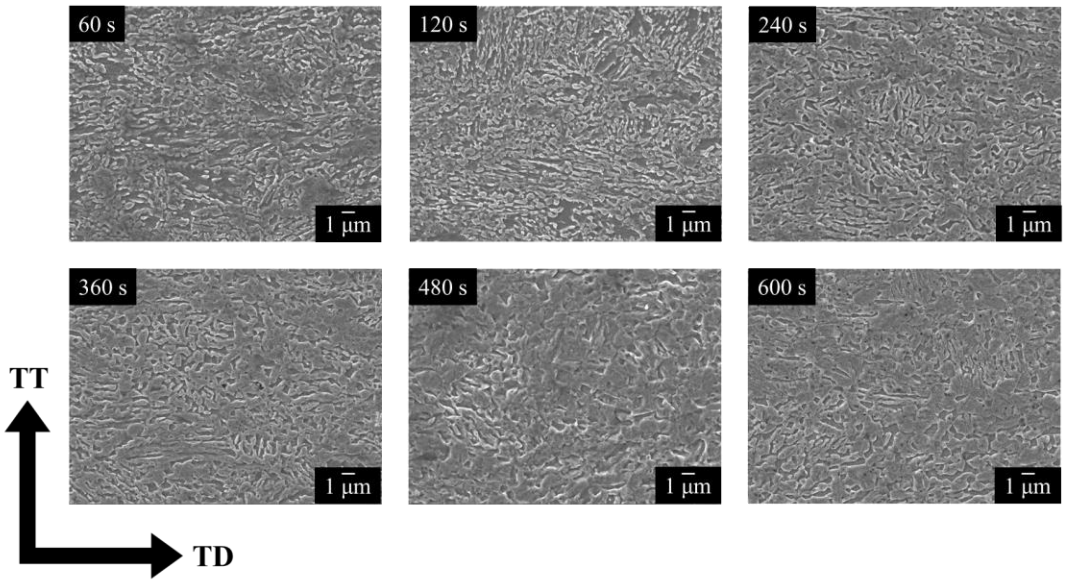

Figure 5.7: SEM micrographs of samples intercritically annealed at 730°C from the TM starting microstructure as a function of IAT holding time.

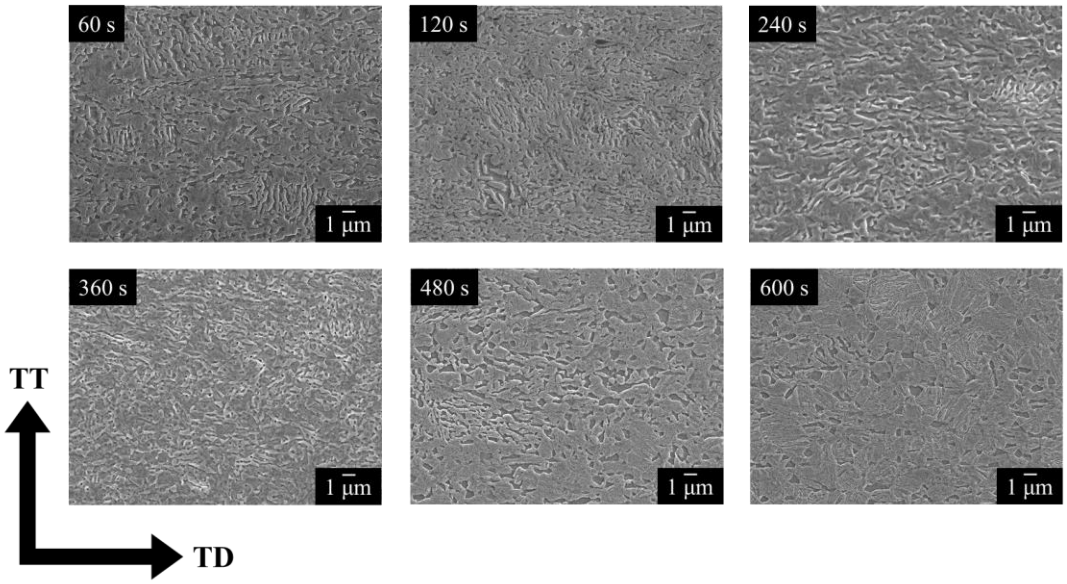

Figure 5.8: SEM micrographs of samples intercritically annealed at 740°C from the TM starting microstructure as a function of IAT holding time.

SEM microstructural images for the samples intercritically annealed from the M starting microstructure are shown in Figure 5.9 to Figure 5.13. All the as-annealed samples from the M starting microstructure consisted of lamellar retained austenite/martensite and ferrite. Samples annealed at 670°C from the M starting microstructure contained islands of ferrite dispersed among packets of lamellar retained austenite/martensite (Figure 5.9). Samples intercritically annealed at 690°C, 710°C, 720°C and 740°C, shown in Figure 5.5, Figure 5.6 through Figure 5.8, respectively, contained small fraction of ferrite. However, they existed between the retained austenite/martensite lamellae, not as islands. Kim et al. [69] suggested that the austenite grew from pre-existing films of retained austenite present in between martensite laths, resulting in a lamellar morphology.

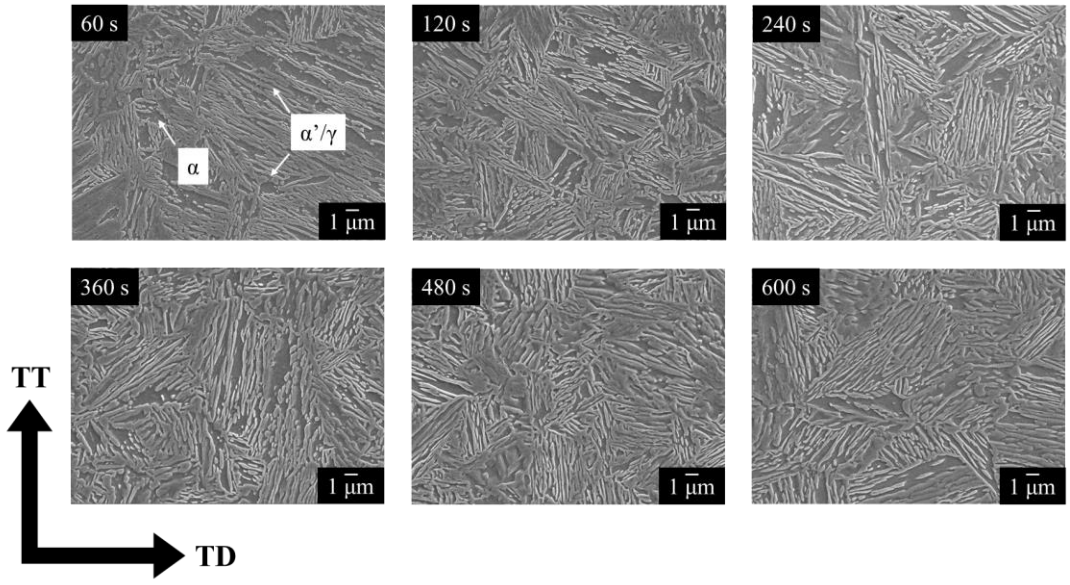

Figure 5.9: SEM micrographs of samples annealed at 670°C from the M starting microstructure as a function of IAT holding time.

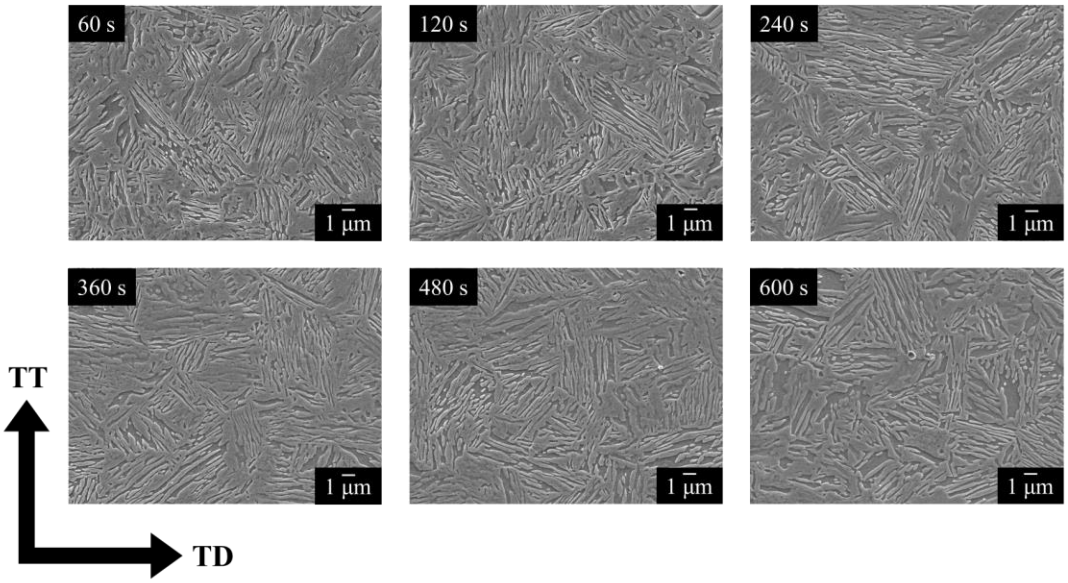

Figure 5.10: SEM micrographs of samples annealed at 690°C from the M starting microstructure as a function of IAT holding time.

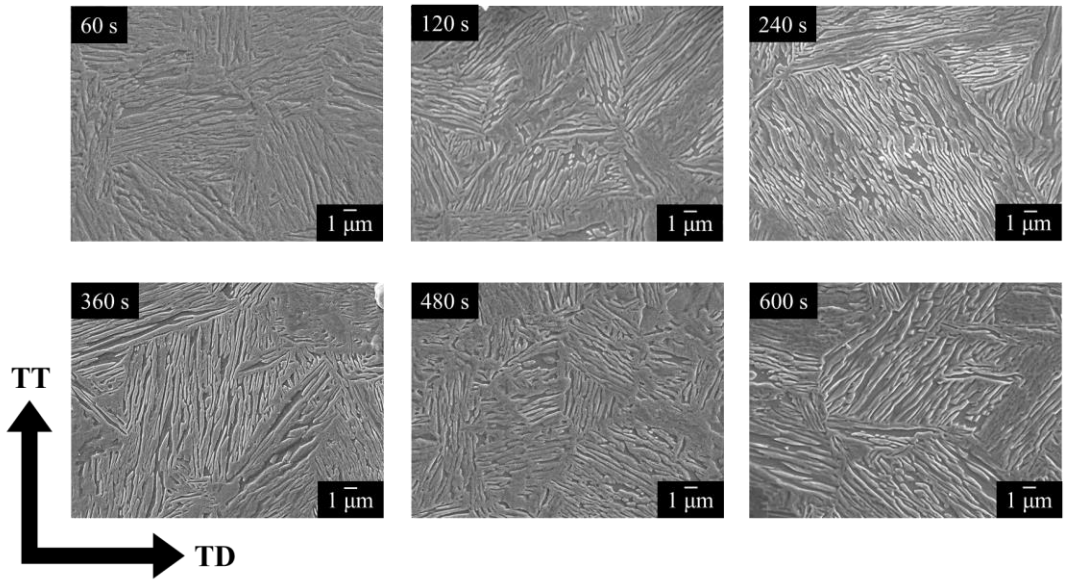

Figure 5.11: SEM micrographs of samples annealed at 710°C from the M starting microstructure as a function of IAT holding time.

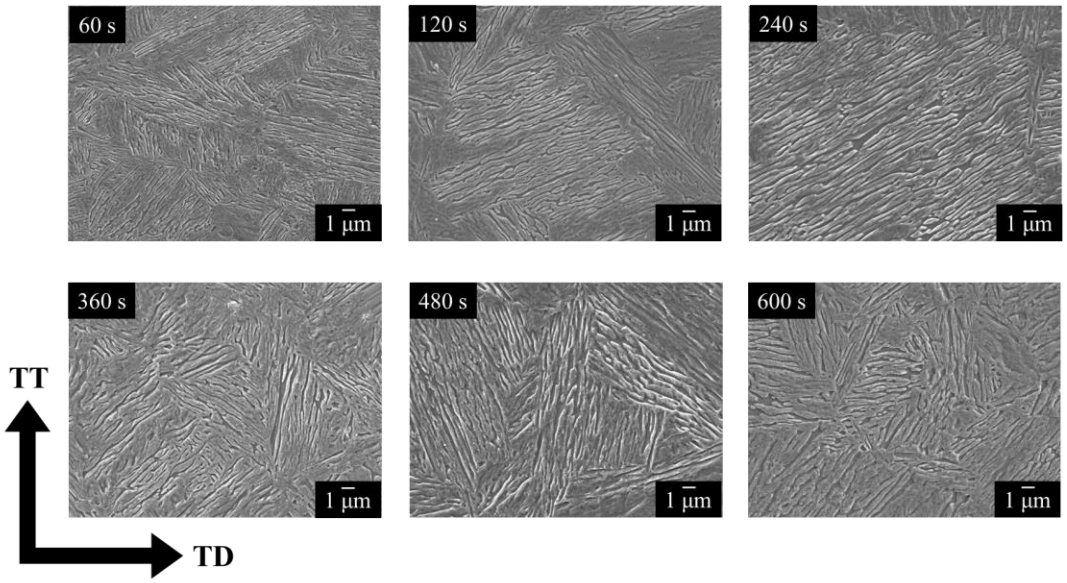

Figure 5.12: SEM micrographs of samples annealed at 720°C from the M starting microstructure as a function of IAT holding time.

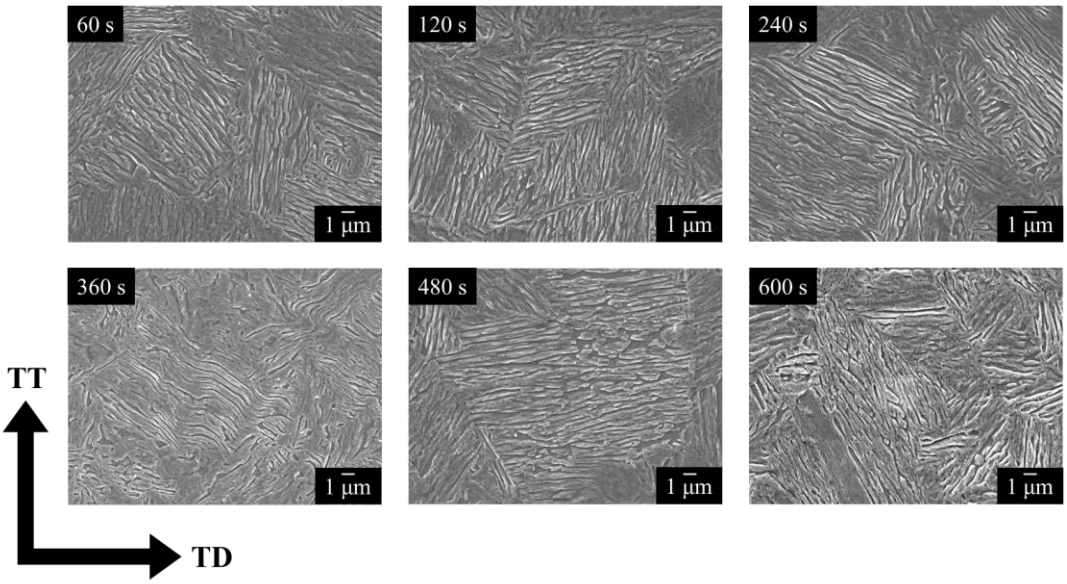

Figure 5.13: SEM micrographs of samples annealed at 740°C from the M starting microstructure as a function of IAT holding time.

5.3. Mechanical Testing

Uniaxial tensile tests were conducted on selected samples intercritically annealed from the TM and M starting microstructures that contained significant volume fractions of chemically stable retained austenite as assessed by XRD (Figure 5.1(a) and (c)).

5.3.1. Tempered Martensite Starting Microstructure

Representative true stress – true strain and their corresponding instantaneous work hardening rate (i.e. ($d\sigma/d\varepsilon$) curves for samples annealed from the TM starting microstructure are shown in Figure 5.14.

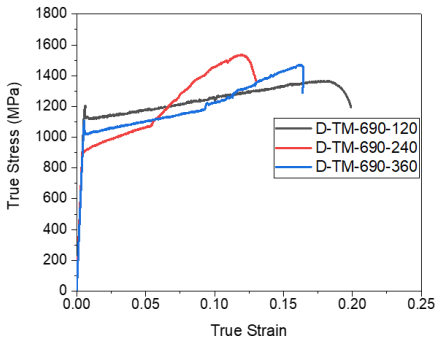
True Stress (MPa)
True Strain
D-TM-690-120
D-TM-690-240
D-TM-690-360

(a)

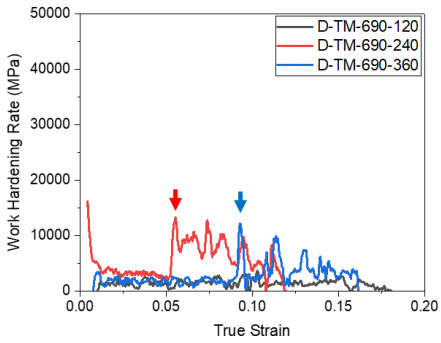
Work Hardening Rate (MPa)
True Strain
D-TM-690-120
D-TM-690-240
D-TM-690-360

(b)

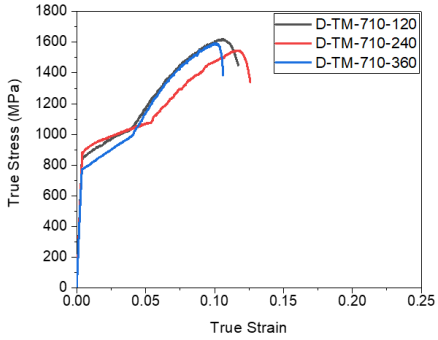
True Stress (MPa)
True Strain
D-TM-710-120
D-TM-710-240
D-TM-710-360

(c)

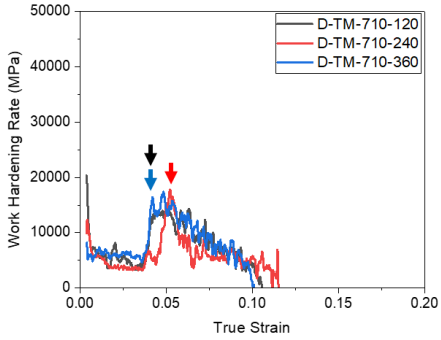
Work Hardening Rate (MPa)
True Strain
D-TM-710-120
D-TM-710-240
D-TM-710-360

(d)

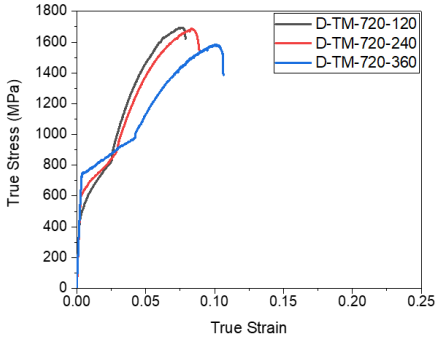
True Stress (MPa)
True Strain
D-TM-720-120
D-TM-720-240
D-TM-720-360

(e)

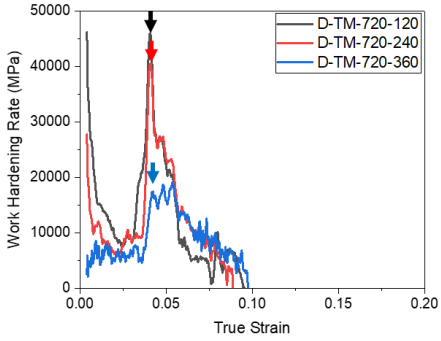
Work Hardening Rate (MPa)
True Strain
D-TM-720-120
D-TM-720-240
D-TM-720-360

(f)

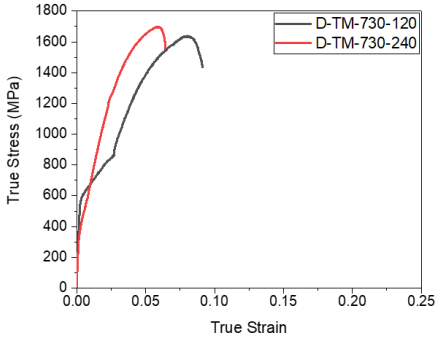
True Stress (MPa)
True Strain
D-TM-730-120
D-TM-730-240

(g)

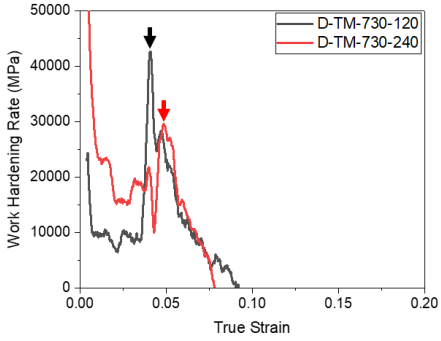
Work Hardening Rate (MPa)
True Strain
D-TM-730-120
D-TM-730-240

(h)

Figure 5.14: True stress – true strain curves of samples annealed from the TM starting microstructure at an IAT of (a) 690°C; (c) 710°C; (e) 720°C and (g) 730°C and corresponding instantaneous work hardening rate curves of samples annealed at an IAT of (b) 690°C; (d) 710°C; (f) 720°C and (h) 730°C.

The TM-690-120 samples exhibited excellent ductility, with a total elongation (TE) of 0.22 engineering strain and but with significant yield point elongation (YPE). The yield strength (YS) and ultimate tensile strength (UTS) were 1190 MPa and 1200 MPa respectively (Figure 5.14(a) and Table 5.1), which was consistent with the work hardening rate curves which showed no significant increase with true strain (Figure 5.14(b)). SEM images of TM-690-120 showed a significant amount of ferrite was present in the as-annealed microstructure (Figure 5.4). TM-690-240 and TM-690-360 exhibited less ductility, with a TE of 0.14 engineering strain and 0.18 engineering strain, respectively with improved UTS, 1360 MPa and 1250 MPa, respectively (Table 5.1). The work hardening rate curves for TM-690-240 and TM-690-360, shown in Figure 5.14(b), show an increase in the work hardening rate at true strains of 0.06 and 0.09, corresponding change in slope of the true stress – true strain plots, shown in Figure 5.14(a). The increase in the work hardening rate indicates the activation of a plasticity enhancing mechanism, either the TRIP effect, TWIP effect or a combination of both. After the increase in slope, the true stress – true strain curves exhibited unstable plastic flow characteristic of dynamic strain ageing (DSA) Portevin Le Chatelier (PLC) effects (Figure 5.14(a)), phenomenon associated with materials exhibiting negative strain rate sensitivity.

The mechanical properties for samples intercritically annealed at 710°C from the TM starting microstructure had higher strength but reduced ductility compared to samples intercritically annealed at 690°C. The mechanical properties were not significantly impacted by changing IAT holding times. The UTS and TE were 1400 MPa and 0.12 engineering strain respectively (Table 5.1). The work hardening rate curves for samples TM-710-120 and TM-710-360 show an increase at a true strain of 0.04, while TM-710-360 shows an increase at a true strain of 0.055 (Figure 5.14(d)). After the increase in slope, the true stress – true strain curves exhibited unstable plastic flow (Figure 5.14(c)).

The TM-720-120 and TM-720-240 showed further increases in strength with reduced ductility, where the mechanical properties showed minimal variance with increased IAT holding time (Figure 5.14(e)). The UTS and TE were 1550 MPa and 0.09 engineering strain respectively (Table 5.1). The mechanical properties of the TM-720-360 sample resembled the mechanical properties exhibited by samples intercritically annealed at 710°C, where the UTS and TE were 1430 MPa and 0.11 engineering strain, respectively (Table 5.1). The work hardening rate curves show an increase at a true strain of 0.04, where the TM-720-120 and TM-720-240 samples exhibited a greater increase in work hardening rate compared to the TM-720-360 samples (Figure 5.14(f)).

Samples intercritically annealed at the highest IAT, 730°C, exhibited the greatest UTS with the lowest TE. Additionally, samples exhibited different mechanical properties with IAT holding times. The true stress – true strain curves for the TM-730-120 samples resembled those of the TM-720-120 and TM-720-240 samples. The TM-730-120 samples had a UTS and TE of 1510 MPa and 0.09 engineering strain, respectively, while the TM-

730-240 samples had a UTS and TE of 1600 MPa and 0.07 engineering strain, respectively (Table 5.1). The work hardening rate curves showed an increase at true strains of 0.04 and 0.05 for the TM-730-120 and TM-730-240 samples, respectively (Figure 5.14(h)).

Samples intercritically annealed from the TM starting microstructure exhibited an increase in UTS and a decrease in TE with increasing IAT (Figure 5.14). Ferrite is known to be a soft and ductile phase [49], the increase in UTS and decrease in TE with increasing IAT (Figure 5.14) is consistent with the microstructural observations, where, SEM images showed that samples intercritically annealed at 690°C (Figure 5.4) contained the greatest volume fraction of ferrite and the volume fraction of ferrite decreased with increasing IAT, samples intercritically annealed at 730°C (Figure 5.7) and 740°C (Figure 5.13) contained very small fractions of ferrite.

Interrupted tensile tests were conducted on selected samples annealed from the TM starting microstructure in order to determine the mechanical stability of the retained austenite. Tensile specimens were pulled to true strains of 0.019, 0.049 and 0.095 and XRD was conducted to determine the volume fraction of retained austenite as a function of true strain, the results of which are shown in Figure 5.15.

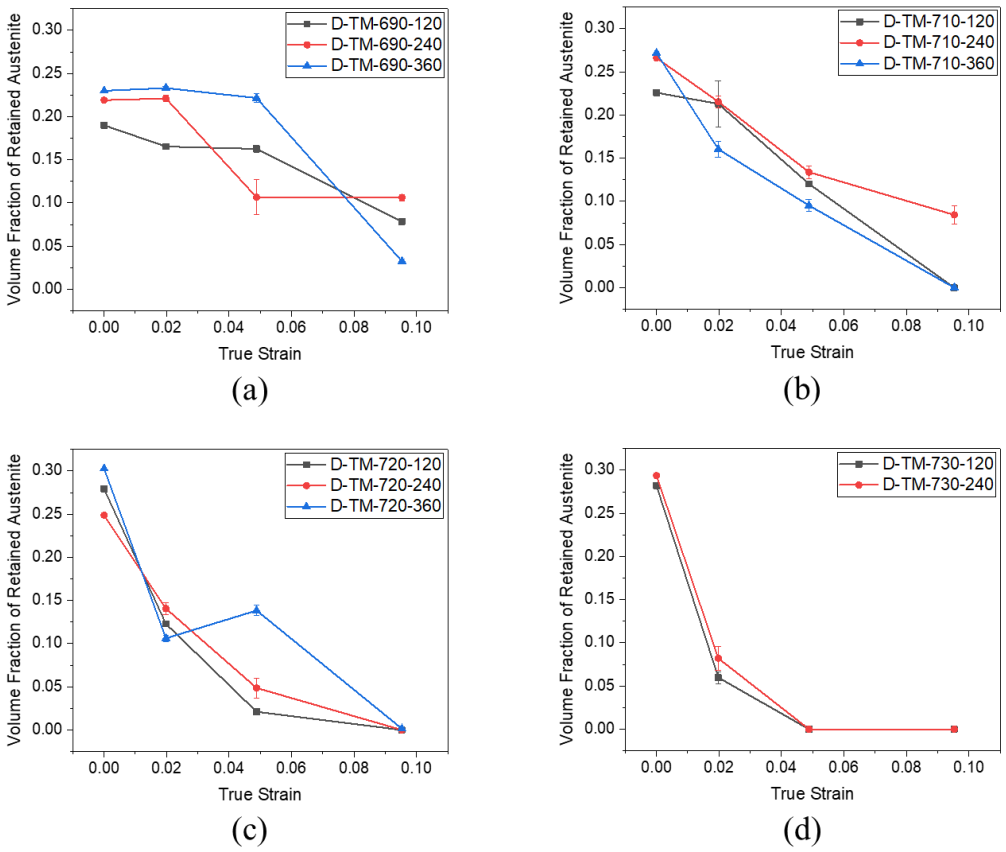

Figure 5.15: Volume fraction of retained austenite as a function of strain for samples intercritically annealed from the TM starting microstructure at (a) 690°C; (b) 710°C; (c) 720°C and (d) 730°C.

The volume fraction of retained austenite for samples intercritically annealed at 690°C from the TM microstructure ranged from 0.19 to 0.23 (Figure 5.15(a)). The TM-690-120 and TM-690-360 samples exhibited minimal reduction in retained austenite with increasing strain, suggesting that the retained austenite was too mechanically stable (Figure 5.15(a)). The TM-690-240 samples exhibited greater transformation of retained austenite to martensite at lower strains compared to the other investigated IAT holding time (Figure

5.15(a)). The volume fraction of retained austenite for samples intercritically annealed at 710°C ranged from 0.22 to 0.27 (Figure 5.15(b)). Samples intercritically annealed at 710°C (Figure 5.15(b)) showed accelerated transformation of retained austenite to martensite upon deformation compared to samples intercritically annealed at 690°C (Figure 5.15(a)). The volume fraction of retained austenite for samples intercritically annealed at 720°C ranged from 0.25 to 0.30 (Figure 5.15(c)) and exhibited faster transformation of retained austenite to martensite with deformation compared to samples intercritically annealed at 710°C (Figure 5.15(b)). The volume fraction of retained austenite of samples intercritically annealed at 730°C was 0.28 and the fastest transformation kinetics of retained austenite to martensite with deformation were observed in this sample (Figure 5.15(d)).

The volume fraction of retained austenite was not significantly impacted by the IAT (Figure 5.15) and the IAT holding time did not influence the mechanical stability of retained austenite (Figure 5.15). The IAT heavily influenced the mechanical stability of retained austenite i.e. the rate at which retained austenite transformed to martensite with deformation. At the lowest IAT of 690°C, the retained austenite exhibited sluggish transformation kinetics ((Figure 5.15(a)) while at an IAT of 730°C, the retained exhibited rapid transformation to martensite with deformation (Figure 5.15(d)).

Table 5.1: Summary of mechanical properties (engineering stress - engineering strain) for samples annealed from the TM starting microstructure.

Sample ID	Yield Strength (MPa)	Ultimate Tensile Strength (MPa)	% Elongation	UTS x % Elongation (MPa %)
D-TM-690-120	1190	1200	22	26400
D-TM-690-240	900	1360	14	19040
D-TM-690-360	1100	1250	18	22500
D-TM-710-120	830	1460	12	17520
D-TM-710-240	880	1380	13	17940
D-TM-710-360	750	1440	11	15840
D-TM-720-120	440	1570	8	12560
D-TM-720-240	600	1550	9	13950
D-TM-720-360	730	1430	11	15730
D-TM-730-120	520	1510	9	13590
D-TM-730-240	300	1600	7	11200

The mechanical properties of samples intercritically annealed from the TM starting microstructure are summarized in Table 5.1. The TM-690-120 samples had a product of UTS × TE of 26,400 MPa% (Table 5.1) and was the only thermal treatment from the TM starting microstructure that met the 3G-AHSSs mechanical property target envelope 24,000 MPa% ≤ UTS × TE ≤ 40,000 MPa%. Samples intercritically annealed at higher IATs exhibited high UTS values, e.g. the TM-730-240 heat treatment resulted in a UTS of 1600 MPa (Table 5.1); however, the increased strength came at the expense of ductility, therefore the mechanical property UTS × TE product targets were not realized.

Overall, the mechanical properties of the TM samples were a strong function of the IAT and did not depend on IAT holding time, where increasing the IAT resulted in improved strength at the expense of the sample's ductility (Figure 5.14). Similar tensile properties evolving largely as a function of the IAT were found by Gibbs et al. [70] for a 0.1C-7Mn-0.1Si alloy. The relationship between the mechanical properties (UTS and TE) and the IAT can be explained by the volume fraction and C content of retained austenite (Figure 5.1) in the as-annealed microstructure and how these factors dictated the retained austenite mechanical stability and resulting rates of retained austenite transformation to martensite with deformation (Figure 5.15) i.e. the TRIP effect, which allowed the material to maintain a high work hardening rate. The sudden change in slope observed in the tensile curves is common among steels exhibiting twinning induced plasticity (TWIP) effect. To investigate the formation of mechanical twins TEM samples were prepared from the as-annealed TM-710-240 samples and tensile specimens pulled to 0.02 engineering strain and 0.05 engineering strain, presented in §5.5.

5.3.2. Martensite Starting Microstructure

True stress – true strain and corresponding work hardening rate curves for samples annealed from the M starting microstructure are shown in Figure 5.16. The derivative of the plastic portion of the true stress – true strain curves were used to determine the instantaneous work hardening rate ($d\sigma/d\varepsilon$) as a function of true strain and are also presented in Figure 5.16.

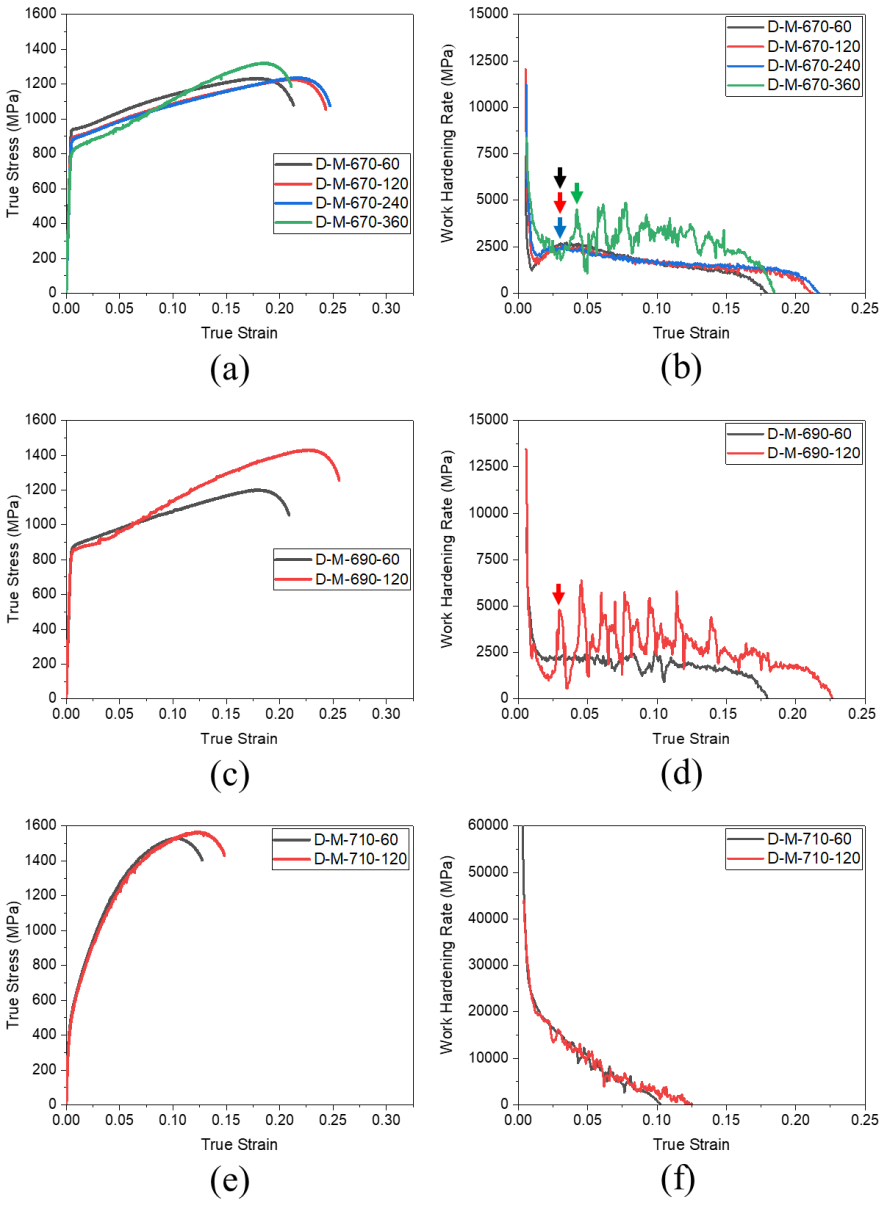

Figure 5.16: True stress – true strain curves of samples annealed from the M starting microstructure at an IAT of (a) 670°C; (c) 690°C and (e) 710°C and instantaneous work hardening rate curves of samples annealed from the M starting microstructure at an IAT

of (b) 670°C; (d) 690°C and (f) 710°C (the scale was changed from 0 MPa to 15,000 MPa to 0 MPa to 60,000 MPa to accommodate the very high initial work hardening rate).

The M-670-60 sample exhibited excellent ductility, with a TE of 0.24 engineering strain and a relatively low UTS of 1045 MPa (Table 5.2). M-670-120 and M-670-240 exhibited similar mechanical properties, with a UTS and TE of 1000 MPa and 0.28 engineering strain respectively (Table 5.2). The true stress – true strain curves (Figure 5.16(a)) and work hardening rate curves (Figure 5.16(b)) for all three samples were similar, exhibiting relatively low work hardening with an increase in the work hardening rate at 0.03 true strain (Figure 5.16(b)). M-670-360 exhibited a slightly increased UTS of 1100 MPa and reduced TE of 0.23 engineering strain (Table 5.2). The true stress – true strain curves exhibit serrated flow, characteristic of DSA (Figure 5.16(a)) [71].

The M-690-60 sample exhibited mechanical properties similar to the samples intercritically annealed at 670°C from the M starting microstructure, where the UTS and TE were 1000 MPa and 0.23 engineering strain respectively (Table 5.2). Sample M-690-120 exhibited the greatest combination of strength and ductility, where the UTS and TE was 1150 MPa and 0.29 engineering strain (Table 5.2), which nearly met the specific mechanical property target of 1200 MPa and 0.30 engineering strain set by the U.S. DOE. Both heat treatments exhibited serrated flow (Figure 5.16(c)); however, only the M-690-120 sample showed an small increase in the work hardening rate at 0.03 true strain, the work hardening curves resemble that of dual phase steels [72] (Figure 5.16(d)).

Increasing the IAT to 710°C resulted in increased strength and reduced ductility (Figure 5.16(e)). The work hardening rates curves (Figure 5.16(f)) initially had a very high work hardening rate that decreased rapidly. The M-710-60 and M-710-120 samples also exhibited limited serrated flow (Figure 5.16(e)). Moreover, the yield strength of samples intercritically annealed at 710°C from the M starting microstructure was 500 MPa compared to 850 MPa from samples intercritically annealed at 690°C.

Samples intercritically annealed from the M starting microstructure showed an increase in the UTS and decrease in TE and YS with increasing IAT (Figure 5.16). Samples intercritically annealed from the TM starting microstructure also exhibited similar relationship between the samples UTS, TE and YS and the IAT (Figure 5.14). Samples intercritically annealed at 670°C (Figure 5.16(b)) and 690°C (Figure 5.16(d)) exhibited an increase in the work hardening rate, however, at 710°C the work hardening rate resembled a dual phase steel i.e. the work hardening rapidly declined with increasing true strain (Figure 5.16(f)).

Interrupted tensile tests were conducted on samples annealed from the M starting microstructure in order to determine the mechanical stability of the resident retained austenite. Tensile specimens machined from samples intercritically annealed at 670°C and 690°C from the M starting microstructure were pulled to 0.049 true strain, 0.095 true strain and 0.139 true strain and samples intercritically annealed at 710°C were pulled to 0.019 true strain, 0.049 true strain and 0.095 true strain. XRD was conducted on the specimens to determine the volume fraction of retained austenite as a function of true strain, the results of which are shown in Figure 5.17.

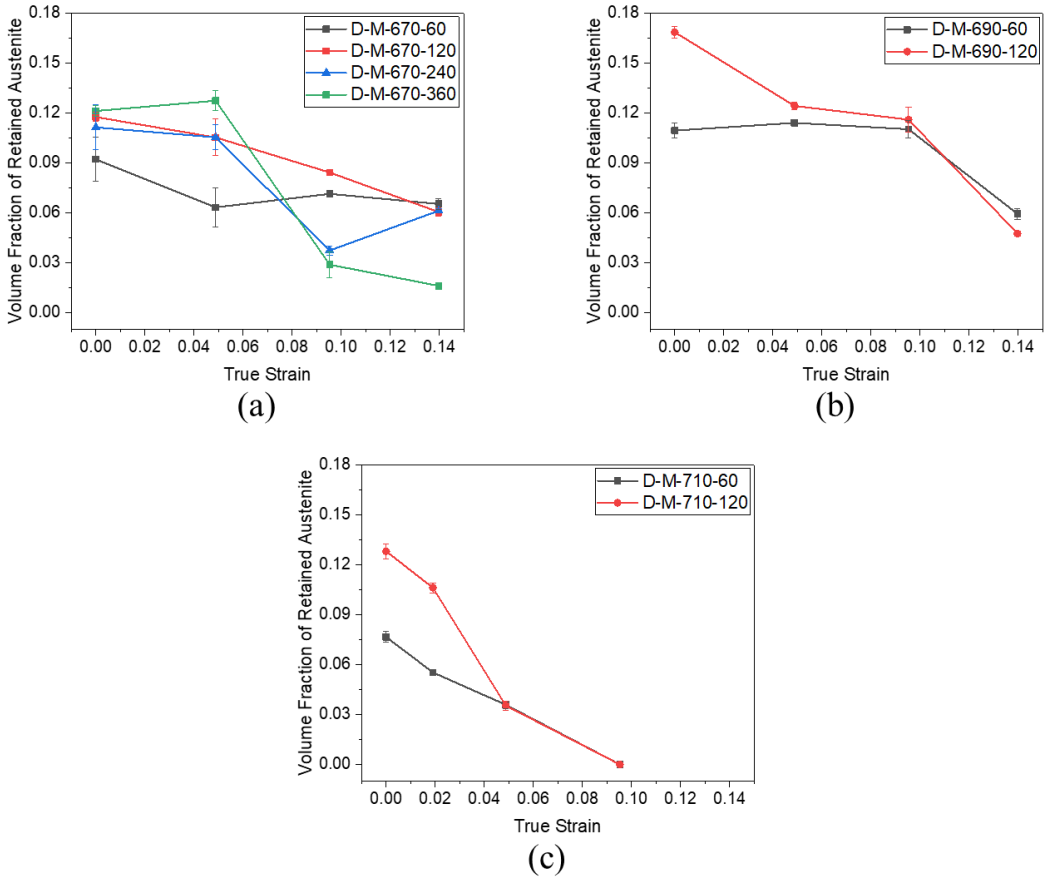

Figure 5.17: Volume fraction of retained austenite as a function of strain for samples annealed from the M starting microstructure at (a) 670°C; (b) 690°C; and (c) 710°C .

Samples intercritically annealed at 670°C (Figure 5.16(a)) and sample M-690-60 (Figure 5.16 (b)) showed sluggish transformation kinetics of retained austenite to martensite with deformation. Additionally, samples intercritically annealed at 670°C (Figure 5.16(a)) and sample M-690-60 (Figure 5.16(c)) exhibited similar mechanical properties. The sluggish $\gamma_{ret} \rightarrow \alpha'$ transformation kinetics resulted in minimal increase in the work hardening rate samples intercritically annealed at 670°C (Figure 5.16(b)) and

sample M-690-60 (Figure 5.16(d)). Sample M-690-120 exhibited a gradual transformation of retained austenite to martensite with deformation (Figure 5.17(b)), which resulted in samples M-690-120 maintaining a high work hardening rate (Figure 5.16(d)). Samples intercritically annealed at 710°C exhibited the fastest $\gamma_{ret} \rightarrow \alpha'$ transformation kinetics of (Figure 5.17(c)), resulting in high strength at the expense of TE (Figure 5.16(e)).

Table 5.2: Summary of mechanical properties (engineering stress - engineering strain) for samples annealed from the M starting microstructure.

Sample ID	Yield Strength (MPa)	Ultimate Tensile Strength (MPa)	% Elongation	UTS x % Elongation (MPa %)
D-M-670-60	945	1045	24	25080
D-M-670-120	900	1000	28	28000
D-M-670-240	895	1000	28	28000
D-M-670-360	850	1100	23	25300
D-M-690-60	865	1000	23	23000
D-M-690-120	845	1150	29	33350
D-M-710-60	500	1390	14	19460
D-M-710-120	500	1390	16	22240

The mechanical properties of samples intercritically annealed from the M starting microstructure are summarized in (Table 5.2). Samples intercritically annealed at 670°C exhibited similar mechanical properties, where the UTS ranged 1000 MPa to 1100 MPa while the TE ranged from 0.23 engineering strain to 0.28 engineering strain, thereby meeting the 3G-AHSSs mechanical properties target envelope of UTS ×TE from 24,000

MPa% ≤ UTS × TE ≤ 36,000 MPa% (Table 5.2). The M-690-60 annealed samples also exhibited mechanical properties that resembled that of the samples intercritically annealed at 670°C (Table 5.2). The M-690-120 sample exhibited UTS and TE of 1150 MPa and 0.29 engineering strain respectively, very close to the specific targets set by the U.S. DOE of UTS and TE of 1200 MPa and 0.30 engineering strain, respectively (Table 5.2). Further increasing the IAT resulted in an increase in strength at the expense of ductility and did not meet the 3G-AHSS mechanical properties target envelope.

Similar to the mechanical properties exhibited by samples intercritically annealed from the TM starting microstructure, the mechanical properties were not significantly impacted by changing the IAT holding times but were significantly dependant on the IAT, which influenced the retained austenite stability. Moreover, apart from the TRIP effect, these samples also exhibited another plasticity enhancing mechanism that increasing the rate of work hardening with strain consistent with TWIP steels. To investigate the formation of mechanical twins in retained austenite TEM samples were prepared from tensile specimens pulled to 0.10 engineering strain and 0.15 engineering strain. The results of the TEM investigation will be presented in §5.5.

5.4. Fractography

Figure 5.18 and Figure 5.19 show the true stress – true strain curves up to the point of necking for samples intercritically annealed from the TM and M microstructure, respectively. The final data point was calculated from the area at fracture, which represents the load experienced by the sample before fracturing within the necked region.

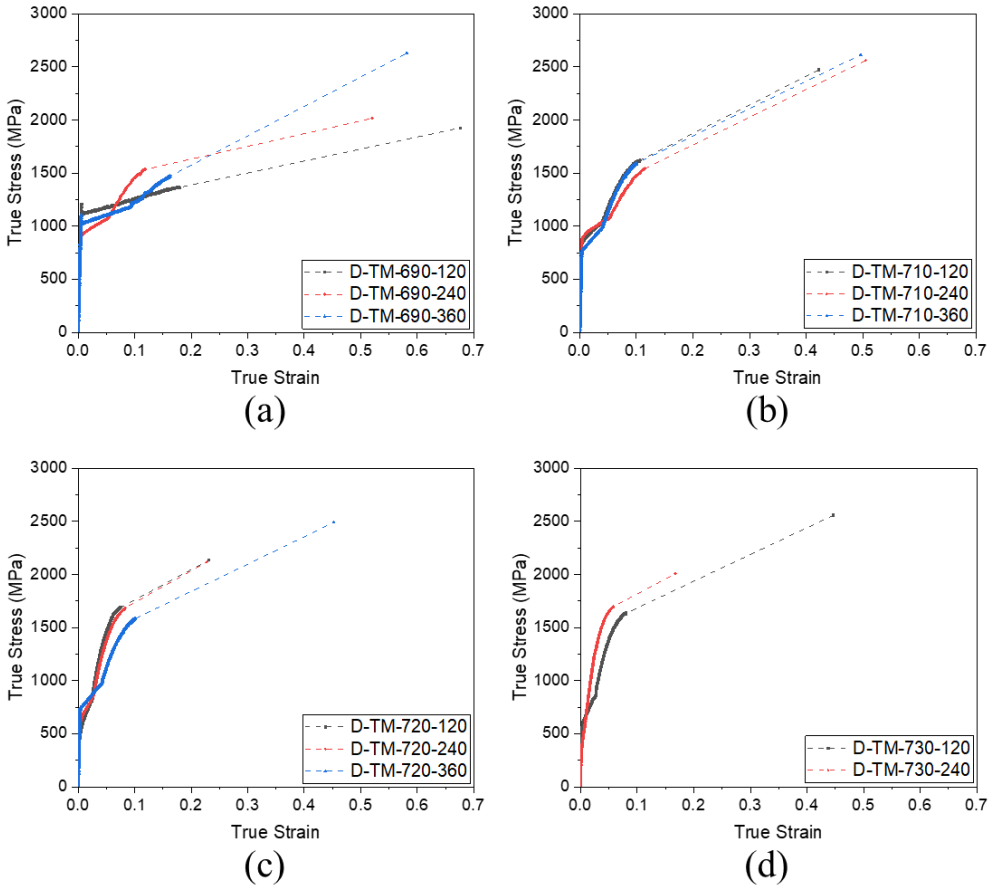

Figure 5.18: True stress – true strain curves including the area at fracture of samples annealed from the TM starting microstructure at an IAT of (a) 690°C; (c) 710°C; (e) 720°C and (g) 730°C.

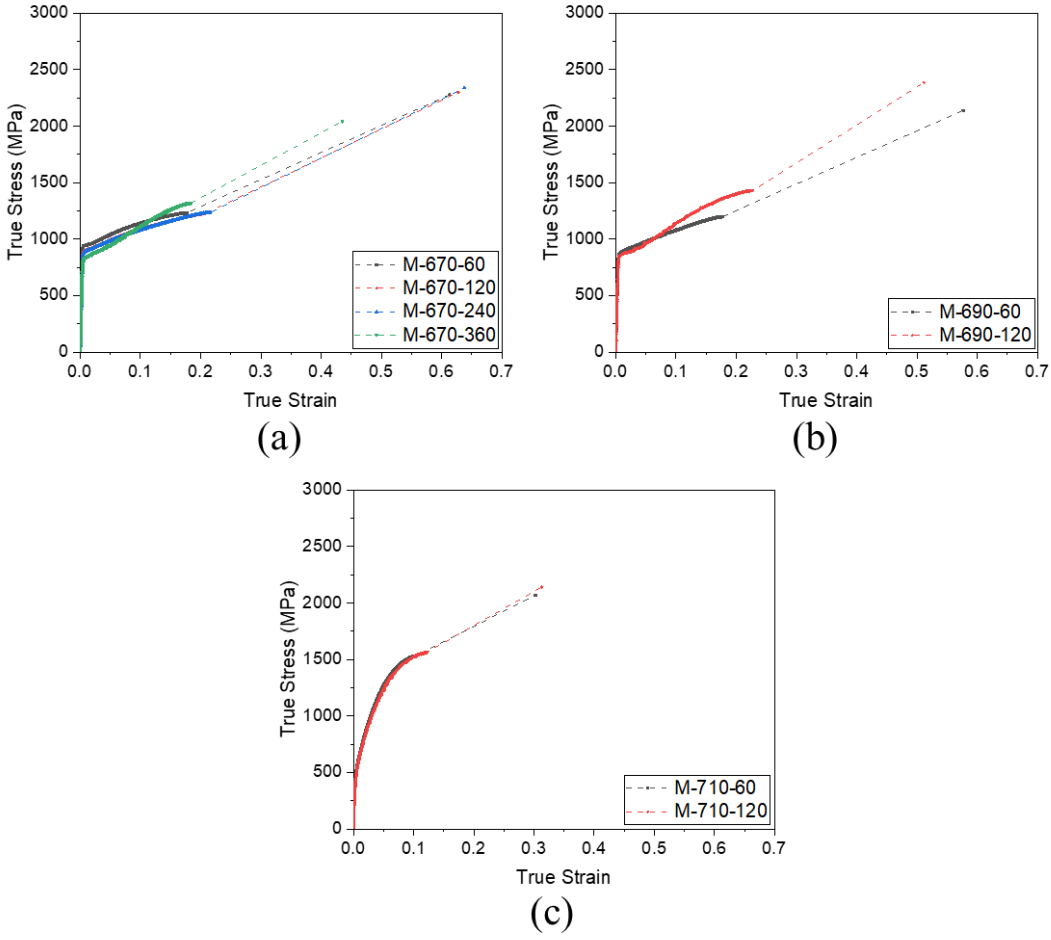

Figure 5.19: True stress – true strain curves including the area at fracture of samples annealed from the M starting microstructure at an IAT of (a) 670°C; (c) 690°C and (e) 710°C.

The elongation at fracture of the TM-690-120, TM-690-240 and TM-690-360 samples was 0.68 true strain, 0.54 true strain and 0.59 true strain, respectively (Figure 5.18(a)). Samples intercritically annealed at 710°C resulted in 0.50 true strain at fracture (Figure 5.18(b)). Samples intercritically annealed at 720°C (Figure 5.18(c)) and 730°C (Figure 5.18(d)) from the TM starting microstructure showed a greater variance in

deformation at failure with IAT holding time. Samples TM-720-120/240 exhibited 0.23 true strain, while sample TM-720-360 resulted in 0.45 true strain. The deformation at fracture improved with increasing IAT holding time for an IAT of 720°C ((Figure 5.18(c)), whereas, the opposite trend was observed for samples intercritically annealed at 730°C from the TM starting microstructure. Sample TM-730-120 exhibited 0.45 true strain at fracture ((Figure 5.18(d)) and sample TM-730-240 exhibited 0.19 true strain at fracture ((Figure 5.18(d)). Samples intercritically annealed at 670°C from the M starting microstructure exhibited 0.65 true strain at fracture (Figure 5.19(a)). Samples M-690-60 and M-690-120 exhibited 0.52 true strain and 0.65 true strain at fracture, respectively (Figure 5.19(b)). Samples intercritically annealed at 710°C from the M starting microstructure exhibited 0.31 true strain at fracture (Figure 5.19(c)). Samples intercritically annealed from both the TM (Figure 5.18) and M (Figure 5.19) starting microstructures exhibit decreasing true strain at failure with increasing IAT, which is consistent with the decrease in TE with increasing IAT observed in the tensile specimens (Figure 5.14 and Figure 5.16).

Fracture surfaces of specimens that underwent uniaxial tensile testing to failure generally had three zones, as shown in Figure 5.20: (1) a fibrous zone (center); (2) radial zone and (3) shear lip zone. The fibrous zone generally surrounded the origin of the critical flaw. It consisted of randomly oriented fibrous regions and indicated stable crack propagation requiring large amounts of energy to grow [73]. Crack growth transitioned from stable slow growth to unstable rapid propagation; this transition was indicated by the radial zone. A coarse radial zone suggests the crack grew by radial shear while a finer radial

zone suggests quasi-cleavage [73]. When the fibrous zone was small, the radial marks deviated from linearity and curved toward the free surface. The shear lip zone was adjacent to the free surface, and very little deformation visible within this zone [73].

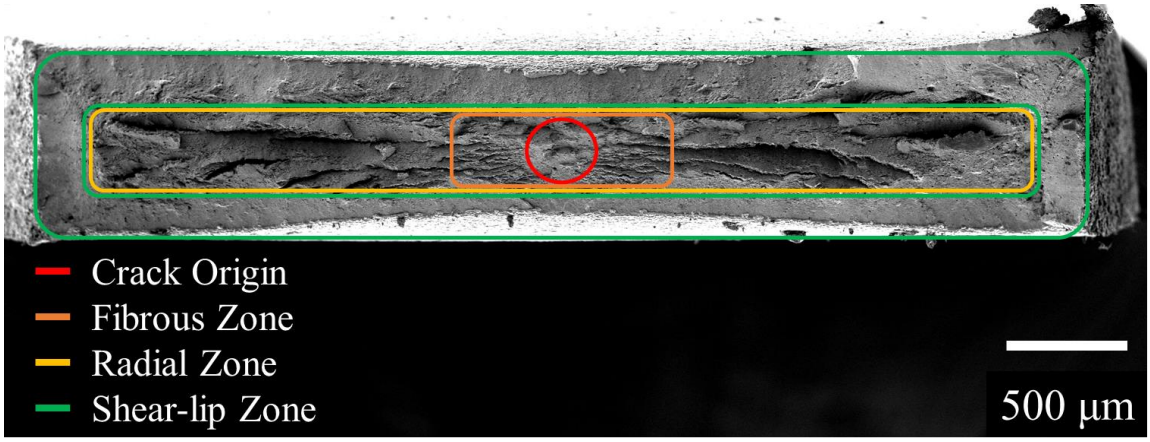

Figure 5.20: Fracture surface of rectangular tensile specimen (M-670-120) showing the crack origin, fibrous zone, radial zone and the shear lip zone.

Representative fracture surfaces are shown in Figure 5.21, for samples intercritically annealed from the TM starting microstructure (Figure 5.21(a)) and M starting microstructure (Figure 5.21(b)). Higher magnification images of the fracture surfaces are shown in Figure 5.22.

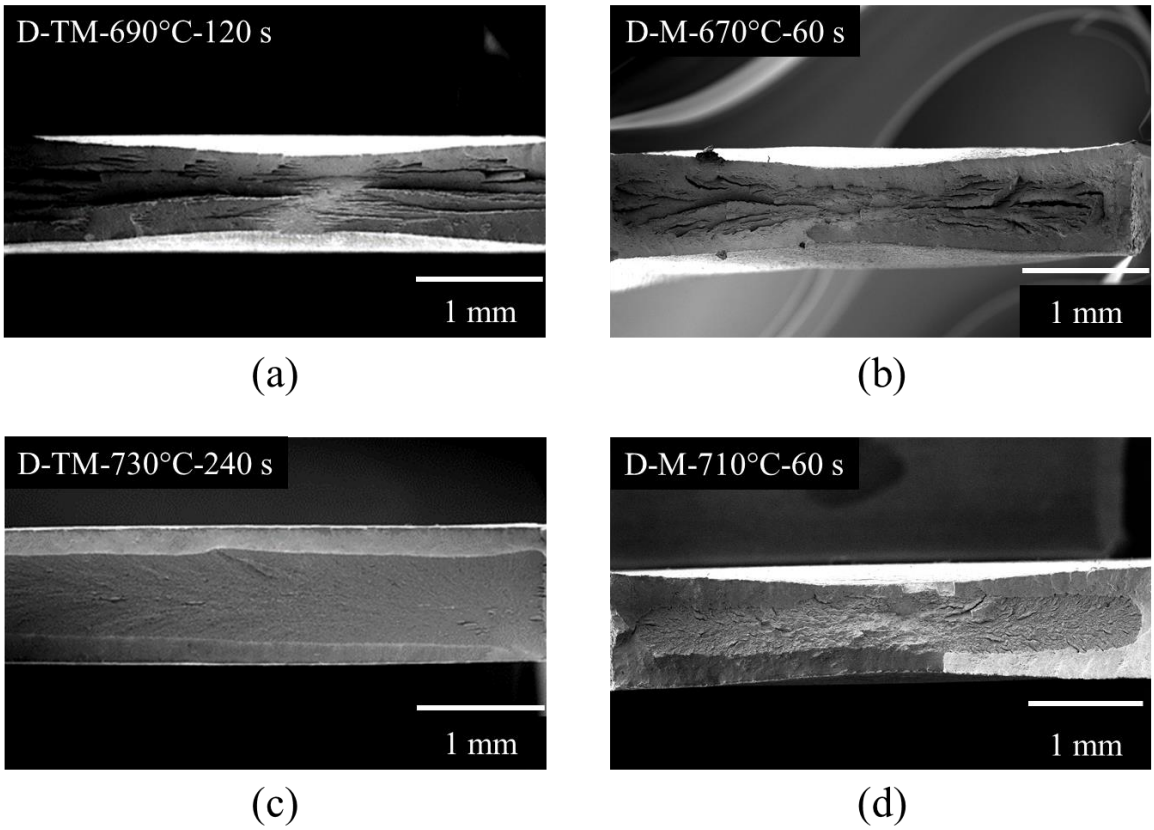

Figure 5.21: Fracture surfaces of (a) TM-690-240; (b) M-670-120; (c) TM-730-240 and (d) M-710-60.

Most samples exhibited the fibrous zone, radial zone and the shear lip zone, highlighted in Figure 5.20. The mode of failure was ductile tearing alongside quasi-cleavage, which was observed in the fibrous and radial zones for nearly all samples. Figure 5.22(a) and Figure 5.22(b) show higher magnification images of sample TM-690-120 and M-670-60, respectively. The fracture surfaces consisted of numerous dimples across the fracture surface (Figure 5.22(a) and Figure 5.22(b)), which formed as a result of micro-void formation and coalescence, which suggests that the samples fractured in a ductile

manner, which is consistent with the large true strain at fracture observed from samples intercritically annealed from the TM (Figure 5.18) and M (Figure 5.19) starting microstructures. The TM-730-240 (Figure 5.21(c)) and M-710-60/120 (Figure 5.21(d)) samples exhibited atypical fracture features. The fracture surface of sample TM-730-240 exhibited only the radial zone and shear lip zone. The radial zone showed minimal deformation (Figure 5.21(c) and Figure 5.22(c)) which is consistent with the true stress - true strain curve of sample TM-730-240 exhibiting the least true strain at fracture (Figure 5.18). Samples M-710-60/120 showed similar fracture surfaces, representative low magnification and high magnification images of the fracture surface are shown in Figure 5.21 and Figure 5.22, respectively. The fracture surfaces of samples M-710-60/120 (Figure 5.21(d) and Figure 5.22(d)) showed less deformation compared to samples intercritically annealed at 670°C (Figure 5.21(b) and Figure 5.22(b)) and 690°C (Figure 5.21(b) and Figure 5.22(b)) from the M starting microstructure. Moreover, the fracture surfaces of samples intercritically annealed at 710°C exhibited features suggesting the samples failed primarily due to quasi-cleavage rather than ductile tearing and micro-void coalescence (Figure 5.21(d) and Figure 5.22(d)). These results are consistent with the lower true strain at fracture exhibited by samples intercritically annealed from the M starting microstructure at 710°C (Figure 5.19(c)) compared to samples intercritically annealed at 670°C (Figure 5.19(a)) and 690°C (Figure 5.19(b)).

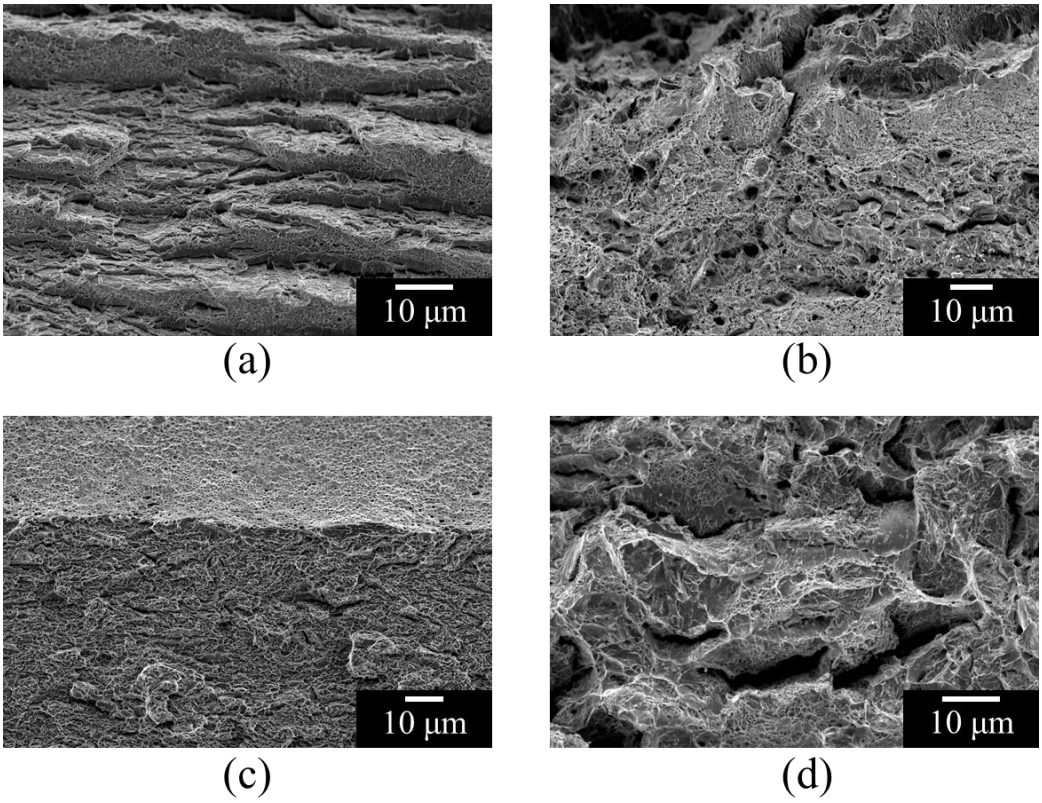

Figure 5.22: Fracture surfaces (high magnification) of (a) TM-690-120; (b) M-670-60; (c) TM-730-240 and (d) M-710-60.

Cross sections of samples strained to failure were observed along the gauge length, away from the fracture surface, to determine crack initiation sites. Figure 5.23 shows a cross-sectional view of the TM-690-120 sample where shear voids nucleated at the ferrite/martensite interface. Similar features were observed in all other specimens.

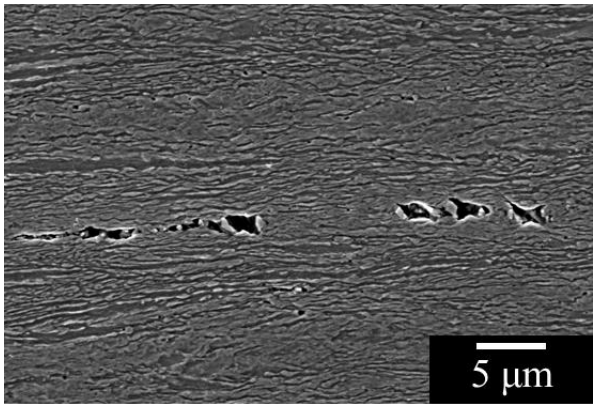

Figure 5.23: Cross sectional view of TM-690-120 away from the fracture surface showing shear void nucleation at the ferrite – martensite interface.

The retained austenite in samples intercritically from TM (Figure 5.15) and M (Figure 5.17) starting microstructure became less mechanically stable as the IAT was increased. As the mechanical stability of retained austenite decreased, the UTS increased, while the TE decreased for samples intercritically annealed from the TM (Figure 5.14) and M (Figure 5.16) starting microstructures.

5.5. Microstructural Characterization – TEM

Fine scale microstructural analysis on the as-annealed and strained samples was conducted on the PHILIPS-CM12 Transmission Electron Microscope (TEM). True stress true strain curves for the TM starting microstructure (Figure 5.14) and M starting microstructure (Figure 5.16), exhibited serrated flow indicative of DSA and PLC effects. Moreover, work hardening curves for the TM starting microstructure (Figure 5.14) and M starting microstrure (Figure 5.16) showed an increase in the work hardening rate, which indicated the possible activation of a plasticity enhancing mechanism other than the TRIP-

effect during deformation. TEM analysis was conducted on selected samples of the as-annealed samples from TM and M starting microstructures which exhibited good mechanical properties – i.e. the TM-710-240, M-690-120 and M-710-120 samples. TEM samples were also prepared for samples pulled to specific engineering strains. In particular, samples were taken from the TM-710-240 sample pulled to 0.02 and 0.05 engineering strain, where these strains corresponded to before and after the increase in the work hardening rate curve observed in Figure 5.14(d). Samples intercritically annealed from the M starting microstructure (Figure 5.16) exhibited greater ductility compared to samples intercritically annealed from the TM starting microstructure (Figure 5.14), TEM specimens from the M-690-120 and M-710-120 samples were prepared at 0.10 engineering strain and 0.15 engineering strain to investigate the possibility of mechanical twinning having occurred in the retained austenite and whether the twin population increased with deformation. Bright field (BF) and dark field (DF) images along with selected area diffraction (SAD) patterns provided information regarding phase identification, phase morphology, and retained austenite twin population and distribution as a function of strain.

The BF image from the TM-710-240 sample pulled to 0.02 engineering strain, shown in Figure 5.24(a), shows that the microstructure had an equiaxed morphology, consistent with the equiaxed morphology observed with the SEM (Figure 5.5). The microstructure consisted of blocky retained austenite (denoted γ), ferrite (denoted α) and martensite (denoted α'). The SAD pattern in Figure 5.24(b), corresponding to the [111] retained austenite zone axis, and exhibited satellite twin spots. The DF images

corresponding to the $(1\bar{1}0)$ and $(10\bar{1})$ planes shown in Figure 5.24(c) and Figure 5.24(d) highlight the twins present within the retained austenite.

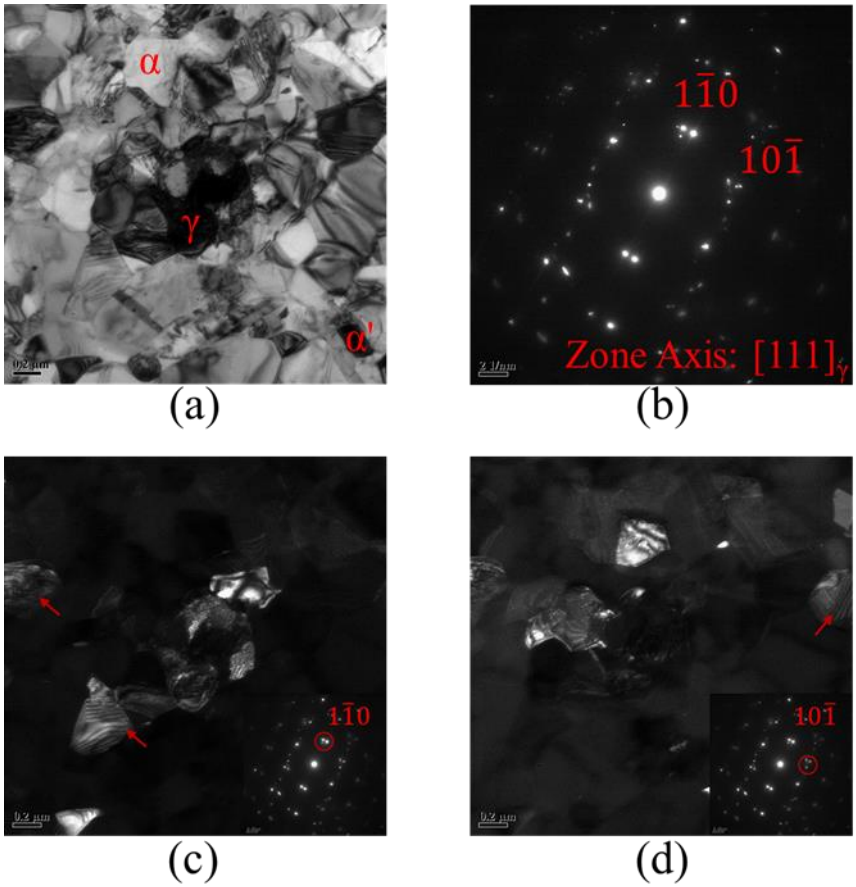

Figure 5.24: TM-710-240 strained to 0.02 engineering strain (a) BF image; (b) SAD corresponding to the [111] retained austenite zone axis; DF images with the objective aperature centered about (c) $1\bar{1}0$ and (d) $10\bar{1}$.

Figure 5.25 shows the TEM results for the TM-710-240 samples pulled to 0.05 engineering strain. The DF images corresponding to the $(1\bar{1}0)$, $(0\bar{1}1)$ and $(10\bar{1})$ planes, shown in Figure 5.25(c), Figure 5.25(d) and Figure 5.25(e), respectively, confirmed the

presence of twins in the retained austenite; however, comparing the samples pulled to 0.02 engineering strain (Figure 5.24) and 0.05 engineering strain (Figure 5.25) it was difficult to ascertain if the twin population increased significantly with this strain increment.

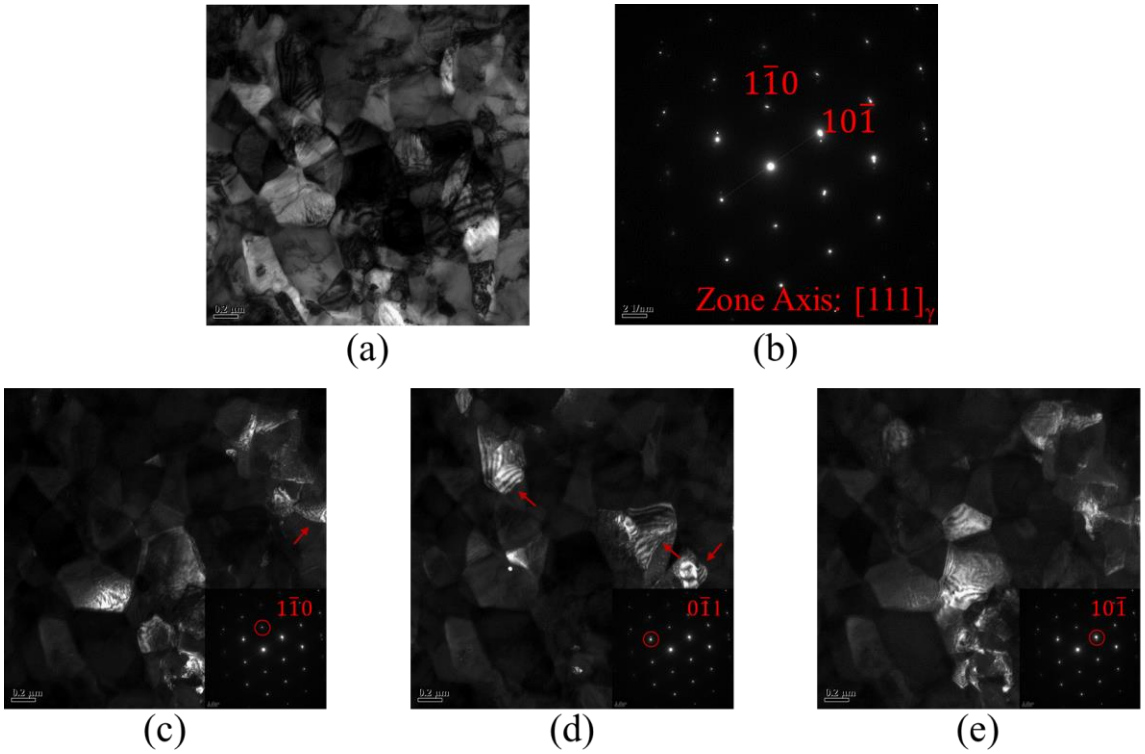

Figure 5.25: TM-710-240 strained to 0.05 engineering strain (a) BF image; (b) SAD pattern corresponding to [111] retained austenite zone axis; DF images centred about (c) $(1\bar{1}0)$; (d) $(0\bar{1}1)$ and (e) $(10\bar{1})$.

Figure 5.26 shows the TEM results for the M-690-120 sample pulled to 0.10 engineering strain. Samples intercritically annealed from the M starting microstructure had a lamellar morphology, which is consistent with the lamellar morphology observed with the SEM, shown in Figure 5.10. The microstructures consisted of lath-type martensite (α'),

film-type retained austenite (γ) and ferrite (α), which were observed in the BF image shown in Figure 5.26(a). The SAD pattern, shown in Figure 5.26(b) contained weak twin satellite spots. Additionally, the DF images corresponding to the $\left(01\bar{1}\right)$ and $\left(0\bar{1}1\right)$ planes, shown in Figure 5.26(c) and Figure 5.26(d), respectively, showed planar faults within the retained austenite grains. The combination of the twin spots observed in the SAD pattern Figure 5.26(b) and the planar faults in the BF and DF images (Figure 5.26), suggest formation of twins within the retained austenite.

Figure 5.27 shows the TEM results for the M-690-120 sample pulled to 0.15 engineering strain. The SAD pattern exhibited prominent twin spots (Figure 5.27(b)). The DF images corresponding to the $\left(\bar{1}10\right)$ and $\left(1\bar{1}0\right)$ planes, shown in Figure 5.27(c) and Figure 5.27(d), respectively, show planar defects within the retained austenite grains, suggesting the formation of twins within the retained austenite.

Figure 5.28 shows the TEM results for the M-710-120 sample pulled to 0.10 engineering strain. The SAD pattern, shown in Figure 5.28(b) showed weak twin spots. However, the DF images, shown in Figure 5.28(c) and Figure 5.28(d), did not show evidence of twin formation within retained austenite.

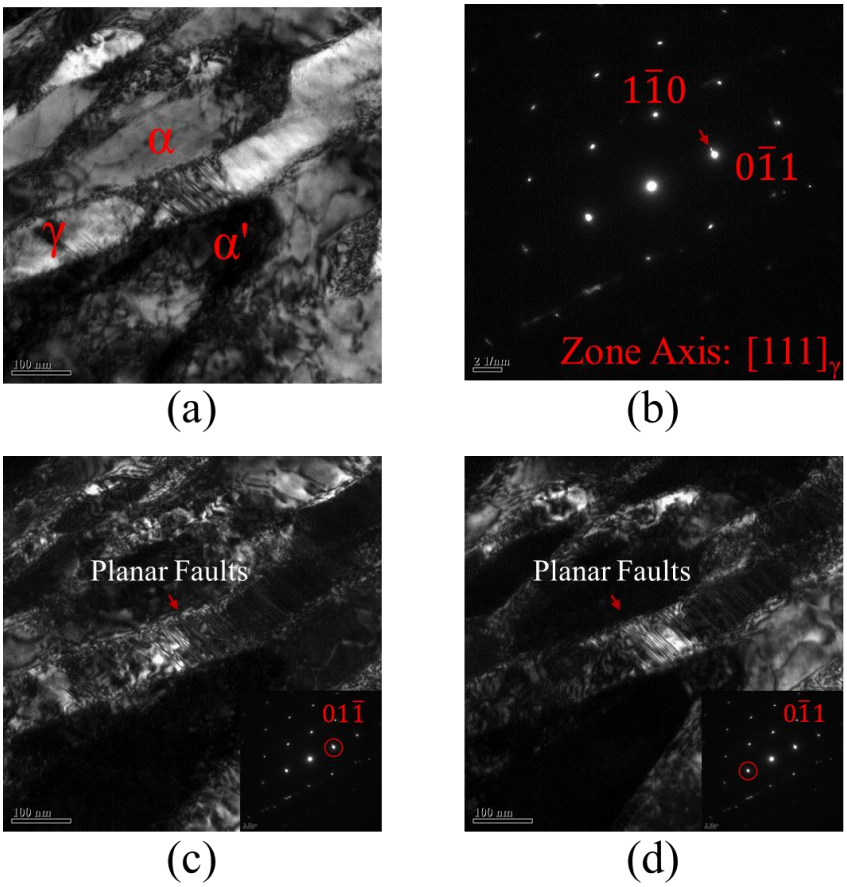

Figure 5.26: M-690-120 strained to 0.10 engineering strain (a) BF image; (b) SAD pattern corresponding to [111] austenite zone axis (arrow indicates weak twin spot); corresponding dark field images centred about (c) $\left(01\bar{1}\right)$ and (d) $\left(0\bar{1}1\right)$.

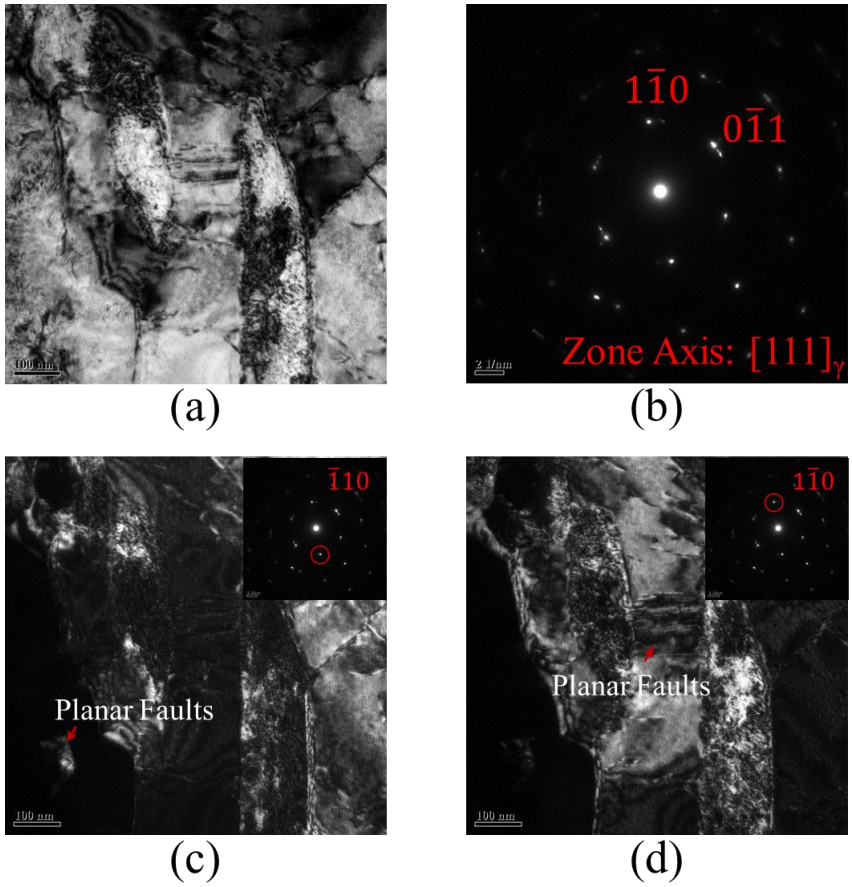

Figure 5.27: M-690-120 strained to 0.15 engineering strain (a) BF image; (b) SAD pattern corresponding to [111] retained austenite zone axis; corresponding DF images centred about (c) $\left(\bar{1}10\right)$ and (d) $\left(1\bar{1}0\right)$.

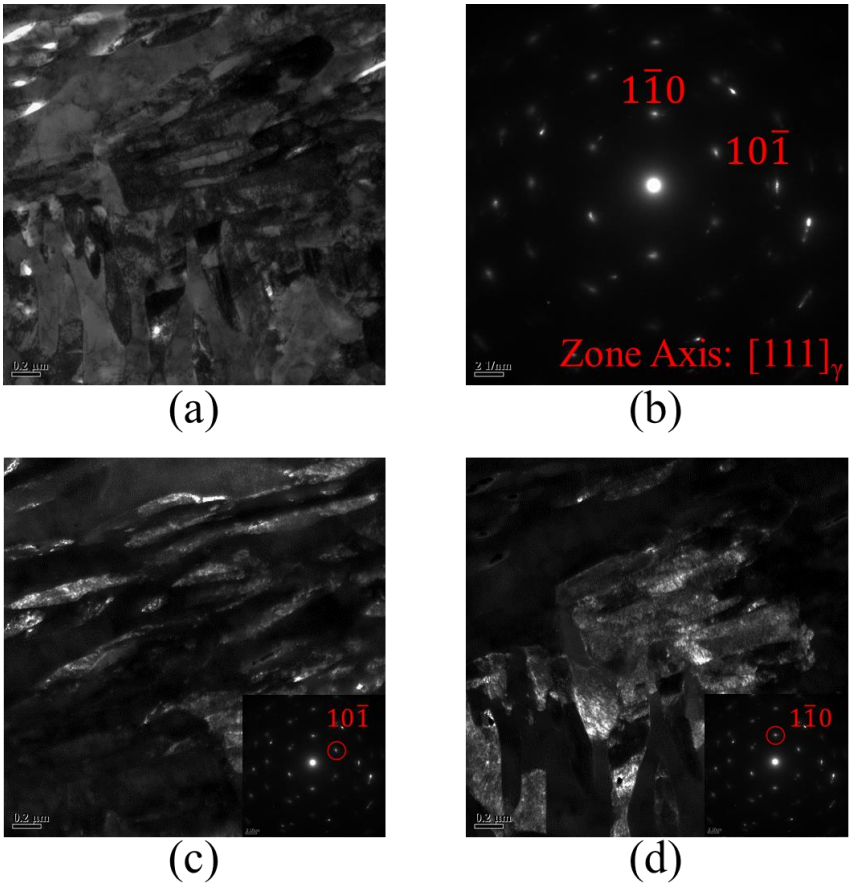

Figure 5.28: M-710-120 strained to 0.10 engineering strain (a) BF image; (b) SAD pattern corresponding to [111] austenite zone axis; DF images centered about (c) $\left(10\bar{1}\right)$ and (d) $\left(1\bar{1}0\right)$.

The most widely reported orientation relationships between retained austenite and ferrite/martensite are the Kurdjumov-Sachs (K-S) [74] and Nishiyama-Wassermann (N-W) [75], [76] orientation relationships, shown in Figure 5.29. Both orientation relations have retained austenite oriented along the [110] zone axis. In the K-S orientation relationship, the [110] austenite zone axis is parallel to the [110] ferrite/martensite zone axis, shown in

Figure 5.29(a). On the other hand, in the N-W orientation relationship, the [110] austenite zone axis is parallel to the [100] ferrite/martensite zone axis, shown in Figure 5.29(b). Both the K-S and N-W orientation relationships were observed in the present samples, where Figure 5.30(a) shows an example of the K-S orientation relationship and Figure 5.30(b) shows both K-S and N-W orientation relationships in the case of the M-690-120 sample. The observed orientation relationships (Figure 5.30) suggests that austenite grew from the parent martensite grains during intercritical annealing.

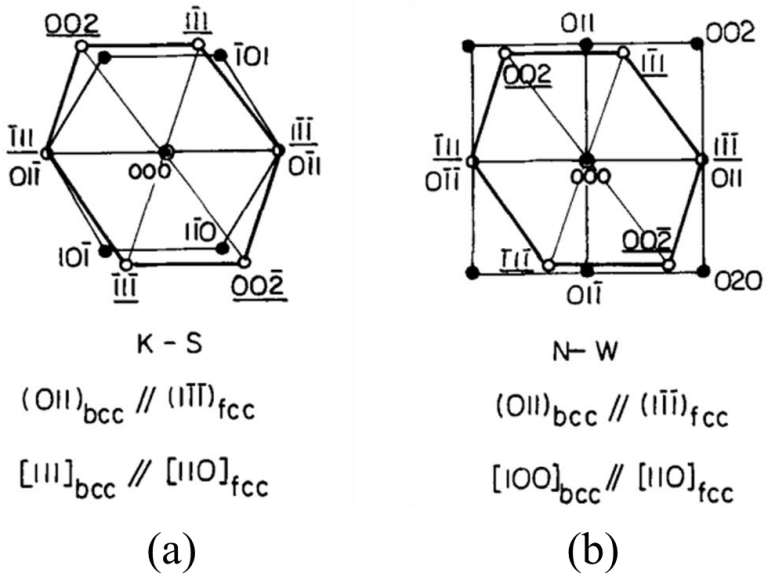

Figure 5.29: Schematic of orientation relationship between retained austenite and ferrite/martensite for (a) Kurdjumov-Sachs and (b) Nishiyama-Wassermann [77].

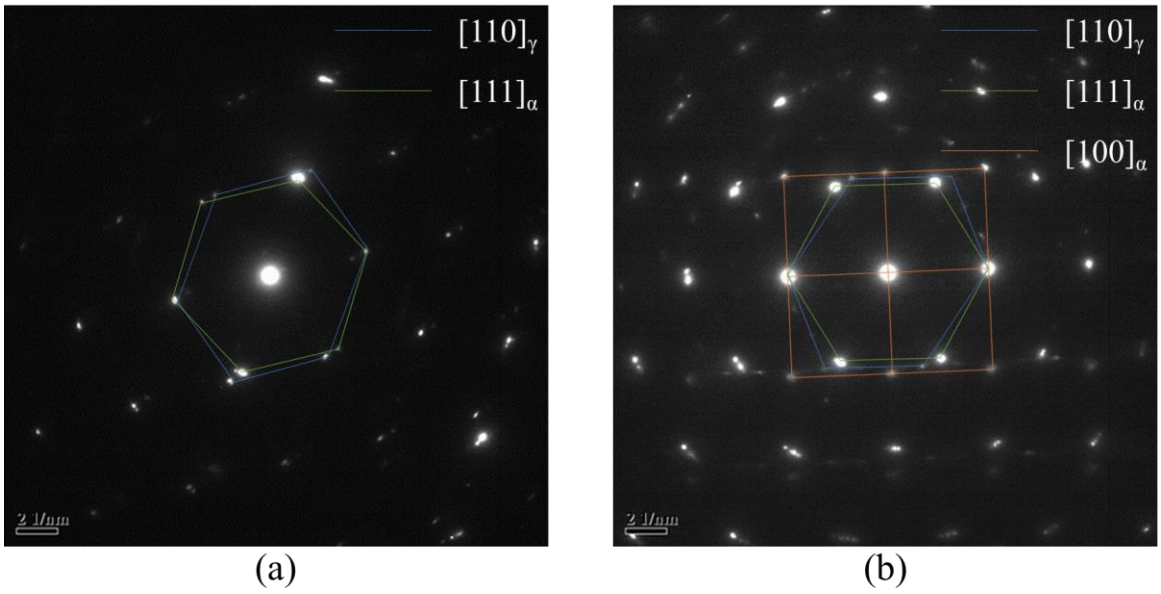

Figure 5.30: Diffraction patterns for (a) M-690-120 pulled to 0.10 strain illustrating the K-S orientation relationship and (b) M-690-120 pulled to 0.15 strain exhibiting both K-S and N-W orientation relationships.

Chapter 6: Discussion

The starting microstructures affected the morphology of the final microstructure. Samples intercritically annealed from the TM starting microstructure had an equiaxed morphology, shown in Figure 5.4 to Figure 5.8, whereas samples annealed from the M starting microstructure had a lamellar morphology, shown in Figure 5.9 to Figure 5.13. The M starting microstructure provided a larger number of nucleation sites compared to the TM microstructure, resulting in finer grains of retained austenite that were more plastically constrained, improving its mechanical stability [41].

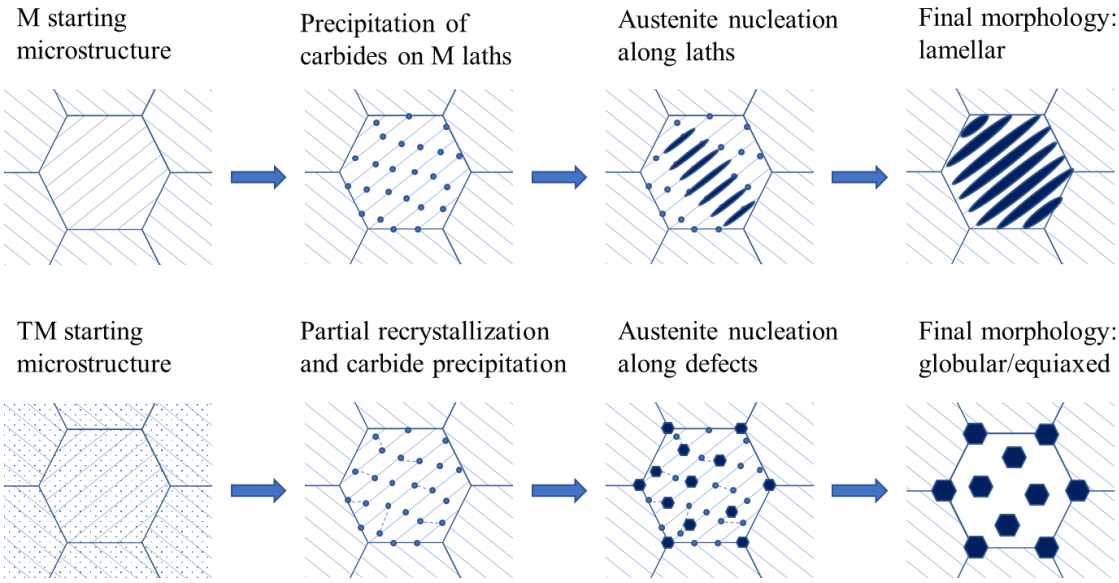

Figure 6.1: Proposed microstructural evolution from the TM and M starting microstructures adapted from Arlazarov et al. [18].

Based on the mechanism for microstructural evolution proposed by Arlazarov et al. [18], Figure 6.1 shows a schematic of the microstructural evolution from the TM and M starting microstructure. The microstructural evolution from the TM starting microstructure is consistent with Arlazarov et al. [18], where partial recrystallization takes place prior to carbide precipitation along high angle boundaries such as prior austenite grain boundaries. Austenite nucleates where carbides are present resulting in a globular/equiaxed morphology of the as-annealed microstructure, consistent with the SEM images shown in Figure 5.4 to Figure 5.8. On the other hand, for the M starting microstructure carbides only precipitated along martensite laths and became sites for austenite nucleation, resulting in a lamellar morphology. Arlazarov et al. [18] suggested that carbides precipitated along high- and low-angle grain boundaries from the M starting microstructure resulting in an as-annealed microstructure exhibiting both lamellar and globular morphology (Figure 5.9 to Figure 5.13). Kim et al. [41] showed that 0.2C-2.2Mn-1.5 alloy intercritically annealed from the M starting microstructure (denoted M1), which consisted of 0.03 volume fraction retained austenite, resulted in a lamellar morphology of the as-annealed microstructure. Kim et al. [41] also investigated a fully martensitic sample (denoted M2), free of retained austenite, which resulted in a globular morphology of the as-annealed microstructure. Kim et al. suggested that the retained austenite present in M1 samples allowed for austenite growth to occur without requiring nucleation of austenite beforehand. The retained

austenite was present as thin films in between the martensite laths, resulting in a lamellar morphology, which is consistent with the present work.

The XRD results illustrate the evolution of the volume fraction of retained austenite in annealed samples shown in Figure 5.1(a) and Figure 5.1(c) for the TM and M starting microstructures, respectively. From the TM starting microstructure, IATs of 710°C and 720°C were required to achieve greater than 0.20 volume fraction retained austenite (Figure 5.1(a)) whereas from the M starting microstructure similar volume fractions of retained austenite were achieved at lower IATs, specifically at 670°C and 690°C (Figure 5.1(c)). Other researchers have shown accelerated retained austenite reversion kinetics from a M starting microstructure compared to a TM starting microstructure for medium Mn steels [8], [38], [41], [69]. The accelerated austenite reversion kinetics were attributed to reduction of diffusion distance for the partitioning of alloying elements, namely C and Mn, and the increased stored energy within the M microstructure compared to the TM microstructure, providing a greater driving force for austenite reversion [38].

Interrupted tensile test results for both the TM and M starting microstructures, shown in Figure 5.15 and Figure 5.17, respectively, showed decreasing retained austenite stability with increasing IAT. At the lowest IATs, in samples M-670-60/120/240/360 (Figure 5.17(a)) and TM-690-120 (Figure 5.15(b)), the retained austenite was too chemically stable and the transformation kinetics to martensite with strain were sluggish, resulting in these samples showing minimal work hardening (Figure 5.14(a), Figure 5.16(a)). With increasing IAT, the retained austenite was less stable and gradually transformed to martensite during deformation (Figure 5.15(b)(c), Figure 5.17(b)); the

activation of the TRIP effect resulted in greater work hardening and a superior balance of strength and ductility (Figure 5.14(b)(c), Figure 5.16(b)). At the highest IATs, 710°C (Figure 5.17(c)) and 730°C (Figure 5.15(c)) for samples annealed from the M and TM starting microstructure, respectively, the retained austenite was mechanically unstable, resulting in a rapid $\gamma_{ret} \rightarrow \alpha'$ transformation and an unsustainable increase in work hardening (Figure 5.14(d), Figure 5.16 (c)). These samples exhibited a significant increase in UTS at the expense of ductility (Figure 6.2). The chemical stability of the retained austenite depended upon the partitioning of alloying elements, primarily C, to the retained austenite during the heat treatment. Jacques et al. [78] concluded that lower IAT resulted in a higher volume fraction of chemically stable retained austenite in low alloy TRIP-assisted steels. At higher temperatures more intercritical austenite formed; however, there was an insufficient amount of C to stabilize it. Similar trends were observed for medium Mn TRIP-assisted steels [37], [79], [80]. At lower IATs the austenite formed was enriched with C, making it more chemically stable [78]. Lee et al. [40] annealed a 0.05C-6.15Mn-1.4Si alloy at an IAT of 640°C for a holding time of 180 s and found the Mn content was close to the equilibrium value i.e. 9.4 wt.%. Additionally, increasing the IAT resulted in a greater volume fraction of retained austenite; however, the C and Mn content decreased [40]. It has been proposed by other researchers [81] that the reduction of C and Mn in retained austenite with increasing amounts of intercritical austenite would explain the reduction of retained austenite stability with increasing IAT. However, electron energy loss

spectroscopy (EELS) analysis or atom probe tomography would have to be conducted to assess the partitioning of alloying elements between austenite and ferrite/martensite.

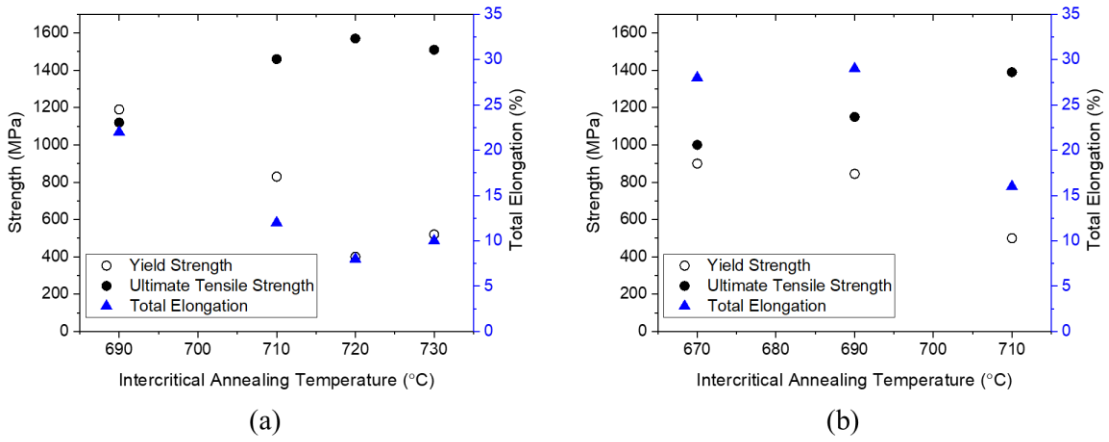

Figure 6.2: Effect of IAT on the YS, UTS and TE for samples intercritically annealed for 120 s from the (a) TM starting microstructure and (b) M starting microstructure.

For both starting microstructures, the ultimate tensile strength (UTS) increased while the total elongation (TE) and yield strength (YS) decreased with increasing IAT, as shown in Figure 6.2. Luo and Dong [38] studied 0.1C-5Mn and 0.2C-5Mn alloy and Steineder et al. [37] investigated a 0.1C-6Mn alloy from the TM and M starting microstructures and found a similar evolution of the mechanical properties with increasing IAT. Luo and Dong [38] suggested that the YS decreased with increasing IAT due to greater partitioning of C from ferrite to austenite during intercritical annealing, resulting in a decrease in YS of ferrite. Ferrite being the softest phase dictated the alloy's YS, which would explain the current trends. Lee et al. [82] suggested that as the IAT increased, the retained austenite became less stable and the onset of $\gamma_{ret} \rightarrow \alpha'$ dictated the YS of the alloy.

The UTS increased while the TE decreased with increasing IAT, which is consistent with the reduction in the mechanical stability of retained austenite with increasing IAT for the TM and M starting microstructures. As the stability of retained austenite was reduced, it underwent the $\gamma_{ret} \rightarrow \alpha'$ at low strains resulting in an increase in the work hardening rate, however, this could not be sustained, resulting in diminished total elongation [38] [37]. Samples intercritically annealed from the TM starting microstructure resulted in greater UTS but lower TE compared to samples intercritically annealed from the M starting microstructure (Figure 6.2). Moreover, the product of UTS × TE was greater for samples intercritically annealed from the M starting microstructure (Table 5.2) compared to the TM starting microstructure (Table 5.1), which was attributed to the greater chemical and mechanical stability of retained austenite (Figure 6.3).

The schematic of the generations of AHSSs is shown again in Figure 6.3, including data points for samples that met the 3G-AHSS mechanical property targets. The mechanical properties of samples intercritically annealed from the TM starting microstructure fell within upper limits of the 1G-AHSS mechanical property envelope (TM-690-120 was the exception). The mechanical properties (product of UTS × TE) of samples intercritically annealed from the M starting microstructure ranged from 25,000 MPa% to 28,000 MPa%, which fell within the 3G-AHSS mechanical property envelope (Figure 6.3,Table 5.1, Table 5.2). The M-690-120 sample exhibited UTS and TE of 1150 MPa and 0.29 engineering

strain respectively, very close to the specific targets set by the U.S. DOE of UTS and TE of 1200 MPa and 0.30 engineering.

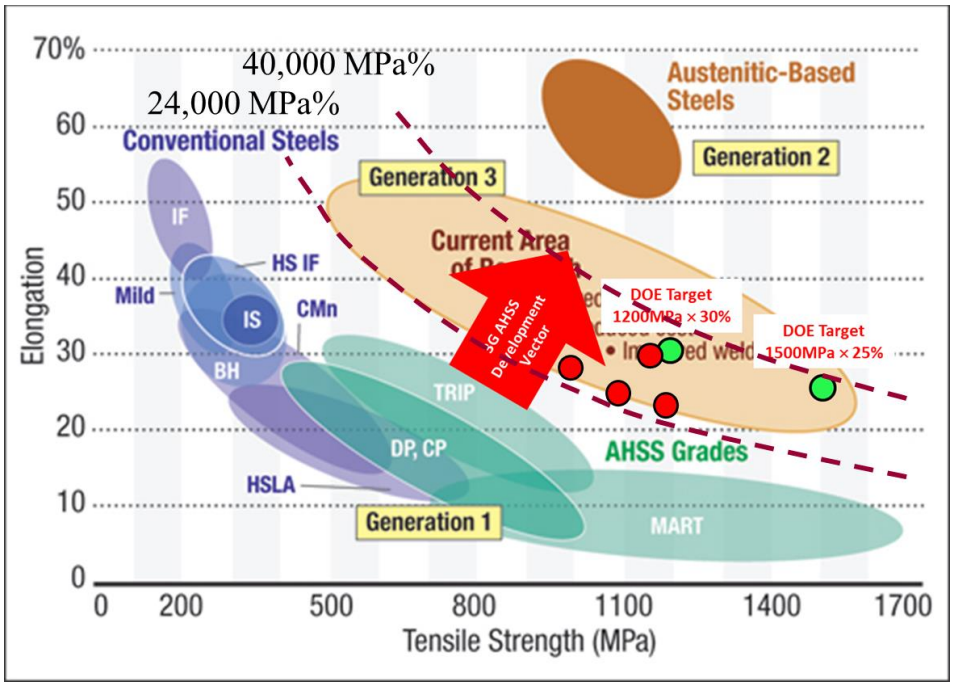

Figure 6.3: Classifications of AHSSs with the 3G-AHSSs mechanical property target window including results from present work (red dots).

Fracture surfaces and the cross sections away from the fracture site were observed using SEM. Most samples exhibited ductile tearing alongside quasi-cleavage, suggesting the classical micro-void nucleation mechanism. Cross sectional images away from the fracture surface showed decohesion at the ferrite-martensite interface, which suggests that failure was driven by void formation at the ferrite-martensite interface. Similar results were found in low alloy TRIP steels [83][84] and medium Mn TRIP steels [60].

Chapter 7: Conclusions

The starting microstructures and IAT significantly influenced the volume fraction and stability of retained austenite, which dictated the mechanical properties through the activation of the plasticity enhancing TRIP and TWIP-effects.

- Samples intercritically annealed at 670°C from the M starting microstructure and 690°C from the TM starting microstructure produced retained austenite which exhibited sluggish transformation kinetics of retained austenite to martensite with deformation. No additional plasticity was provided by the TRIP or TWIP effects due to this unsuitable retained austenite stability, resulting in lower tensile strengths due to the resultant low work hardening rates but resulted in excellent tensile elongations.
- The M-690-120 heat treatment samples exhibited twin formation within the retained austenite and a gradual transformation to martensite with deformation. The combination of the TRIP and TWIP effects allowed the samples to maintain a high work hardening rate and resulted in an excellent combination of strength and ductility (i.e. a UTS × TE of 33,350 MPa%).
- Samples intercritically annealed at 710°C from the M starting microstructure produced less stable retained austenite, accelerating the transformation kinetics of retained austenite to martensite during deformation. The TRIP and TWIP effects were not sustained, resulting in greater strength but reduced tensile elongation.

- Samples intercritically annealed from the M starting microstructure resulted in a lamellar morphology of the as-annealed microstructure whereas samples intercritically annealed from the TM starting microstructure had a globular/equiaxed morphology. The lamellar morphology of retained austenite originating from the M starting microstructure exhibited greater mechanically stable compared to blocky retained austenite, consistent with literature.
- Samples intercritically annealed from the M starting microstructure exhibited faster austenite reversion kinetics and enhanced stability of retained austenite compared to samples intercritically annealed from the TM starting microstructure.

Retained austenite within samples intercritically annealed from the TM starting microstructure showed poor mechanical stability, resulting in improved strength at the expense of ductility for IATs greater than 690°C. Apart from TM-690-120 heat treatment, samples intercritically annealed from the TM starting microstructure did not meet the 3G-AHSSs mechanical property targets due to limited ductility.

Appendix I:

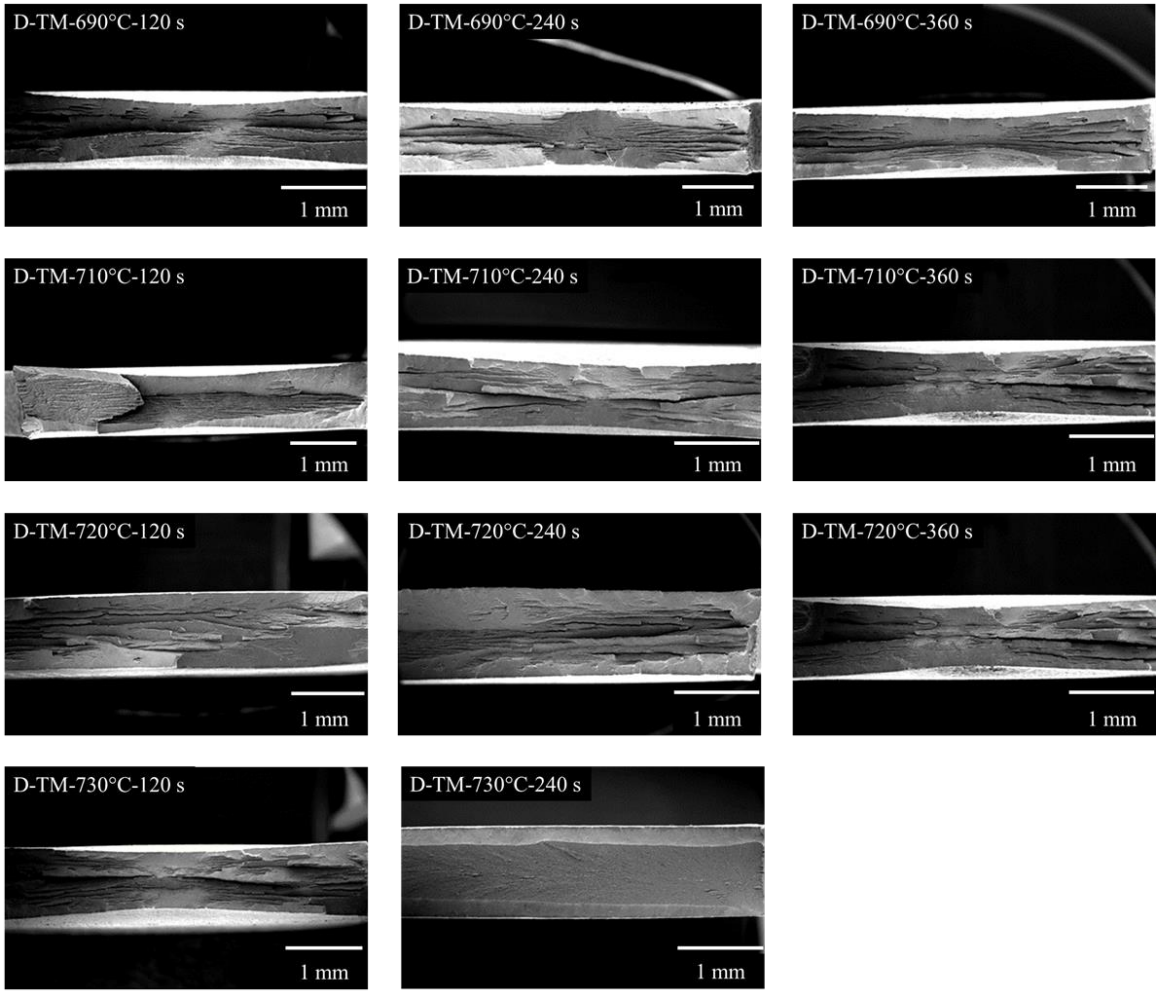

Figure I.1: Fracture surfaces of samples intercritically annealed from the TM starting microstructure.

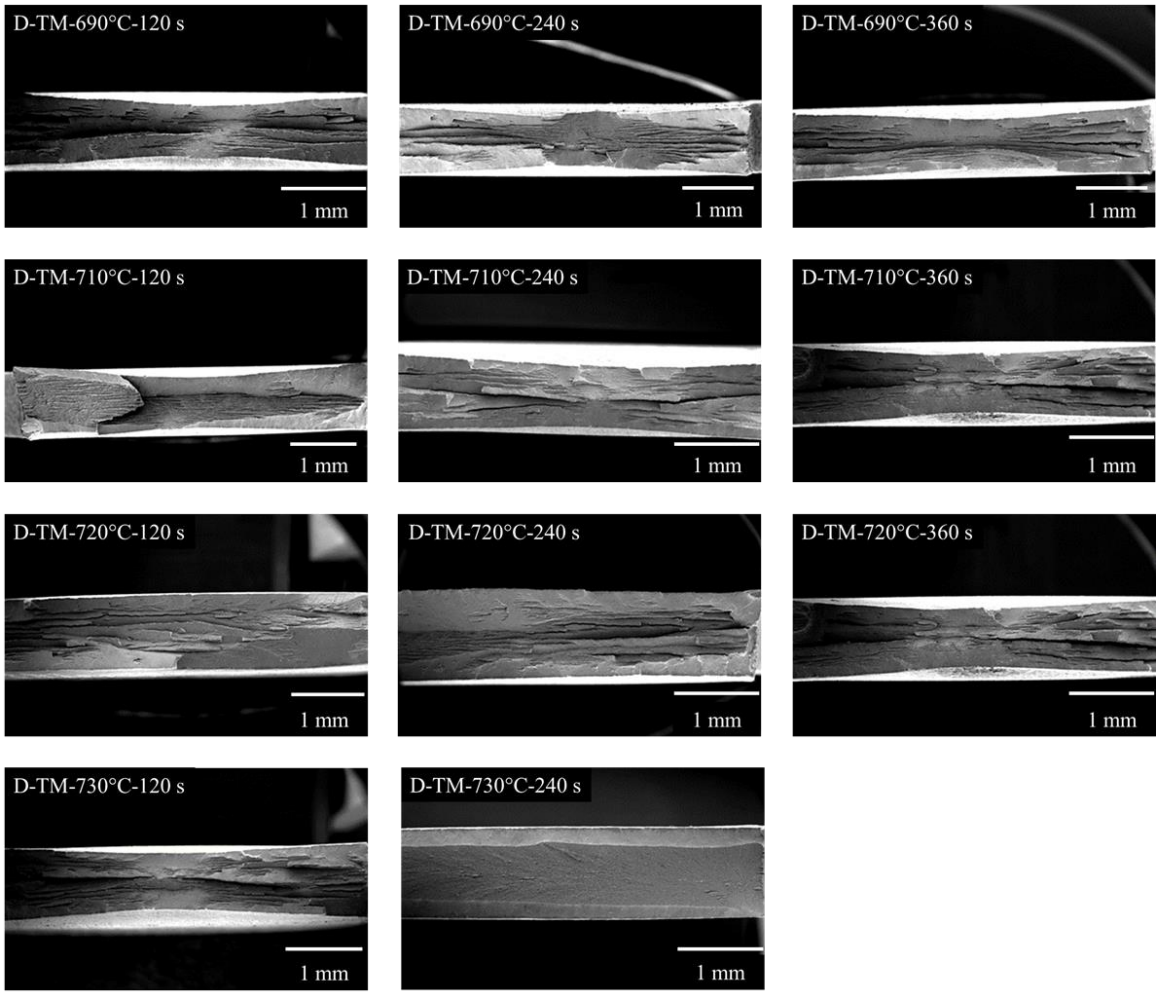

Figure I.2: Fracture surfaces of samples intercritically annealed from the M starting microstructure

Chapter 8: References

[1] E. De Moor, P. J. Gibbs, J. G. Speer, D. K. Matlock, and J. G. Schroth, "AIST transactions strategies for third-generation advanced high-strength steel development," *Iron steel Technol.*, vol. 7, no. 11, p. 132, 2010.

[2] A. T. Davenport, "Formable HSLA and Dual-Phase Steels," *Chicago*, 1977.

[3] D. K. Matlock and J. G. Speer, "Design considerations for the next generation of advanced high strength sheet steels," in *Proc. of the 3rd International Conference on Structural Steels, ed. by HC Lee, the Korean Institute of Metals and Materials, Seoul/Korea*, 2006, pp. 774–781.

[4] "2019 Volvo XC90 - Luxury SUV | Volvo Car USA." .

[5] C. Schutte, "SAE Technical Paper 2015-01-0405." 2015.

[6] E. De Moor, P. J. Gibbs, J. G. Speer, D. K. Matlock, and J. G. Schroth, "Strategies for third-generation advanced high-strength steel development," in *Iron and Steel Technology*, 2010, vol. 7, no. 11, pp. 133–144.

[7] D. K. Matlock and J. G. Speer, "Third Generation of AHSS: Microstructure Design Concepts," in *Microstructure and Texture in Steels*, London: Springer London, 2009, pp. 185–205.

[8] D. M. Pallisco, J. R. McDermid, E. A. McNally, and Goodwin Frank E., "Effect of Starting Microstructure and Intercritical Annealing Parameters on the Mechanical Property Development of a Medium-Mn Third-Generation Advanced High Strength Steel," in *Galvatech*, 2017, pp. 782–789.

[9] S. Lee and B. C. De Cooman, "On the Selection of the Optimal Intercritical Annealing Temperature for Medium Mn TRIP Steel."

[10] S. Lee and B. C. De Cooman, "Effect of the Intercritical Annealing Temperature on the Mechanical Properties of 10 Pct Mn Multi-phase Steel," *Metall. Mater. Trans. A*, vol. 45, no. 11, pp. 5009–5016, Oct. 2014.

[11] S. Lee, S. Shin, M. Kwon, K. Lee, and B. C. De Cooman, "Tensile Properties of Medium Mn Steel with a Bimodal UFG $\alpha + \gamma$ and Coarse δ-Ferrite Microstructure," *Metall. Mater. Trans. A*, vol. 48, no. 4, pp. 1678–1700, Apr. 2017.

[12] S. Lee, K. Lee, and B. C. De Cooman, "Communication Observation of the TWIP + TRIP Plasticity-Enhancement Mechanism in Al-Added 6 Wt Pct Medium Mn Steel."

[13] S. Lee and B. C. De Cooman, "Annealing Temperature Dependence of the Tensile

Behavior of 10 pct Mn Multi-phase TWIP-TRIP Steel," *Metall. Mater. Trans. A*, vol. 45, no. 13, pp. 6039–6052, Dec. 2014.

[14] K. Steineder, D. Krizan, R. Schneider, C. Béal, and C. Sommitsch, "On the microstructural characteristics influencing the yielding behavior of ultra-fine grained medium-Mn steels," *Acta Mater.*, vol. 139, pp. 39–50, Oct. 2017.

[15] K. Steineder, D. Krizan, R. Schneider, C. Beal, and C. Sommitsch, "The Effects of Intercritical Annealing Temperature and Initial Microstructure on the Stability of Retained Austenite in a 0.1C-6Mn Steel," *Mater. Sci. Forum*, vol. 879, pp. 1847–1852, Nov. 2016.

[16] A. R. Marder, "The metallurgy of galvanized coatings," *Progr. Mater. Sci*, vol. 45, pp. 191–271, 2000.

[17] D. Lee, J.-K. Kim, S. Lee, K. Lee, and B. C. De Cooman, "Microstructures and mechanical properties of Ti and Mo micro-alloyed medium Mn steel," *Mater. Sci. Eng. A*, vol. 706, pp. 1–14, Oct. 2017.

[18] A. Arlazarov and M. Goune, "Characterization of microstructure formation and mechanical behavior of an advanced medium Mn steel Development of ecological ceramic/polymer nanocomposites for biomedical and energy storage applications View project Spinodal decomposition View project," 2012.

[19] M. Pourmajidian and J. R. Mcdermid, "Effect of Annealing Temperature on the Selective Oxidation and Reactive Wetting of a 0.1C-6Mn-2Si Advanced High Strength Steel During Continuous Galvanizing Heat Treatments," *ISIJ Int.*, vol. 58, no. 9, pp. 1635–1643, Sep. 2018.

[20] M. Pourmajidian and J. R. McDermid, "On the reactive wetting of a medium-Mn advanced high-strength steel during continuous galvanizing," *Surf. Coatings Technol.*, vol. 357, pp. 418–426, Jan. 2019.

[21] S. E. A., "Private Communication." 2005.

[22] M. Pourmajidian and J. R. McDermid, "Selective Oxidation of a 0.1C-6Mn-2Si Third Generation Advanced High-Strength Steel During Dew-Point Controlled Annealing," *Metall. Mater. Trans. A*, vol. 49, no. 5, pp. 1795–1808, May 2018.

[23] C. Wagner, "Reaktionstypen bei der Oxydation von Legierungen," *Zeitschrift für Elektrochemie, Berichte der Bunsengesellschaft für Phys. Chemie*, vol. 63, no. 7, pp. 772–782, Sep. 1959.

[24] J. Maki, J. Mahieu, B. C. De Cooman, and S. Claessens, "Galvanisability of silicon free CMnAl TRIP steels," *Mater. Sci. Technol.*, vol. 19, no. 1, pp. 125–131, 2003.

[25] J. Mahieu, B. C. De Cooman, and S. Claessens, "Galvanizability of high-strength steels for automotive applications," *Metall. Mater. Trans. A*, vol. 32, no. 11, pp. 2905–2908, Nov. 2001.

[26] D. K. Matlock and J. G. Speer, "Design Considerations for the Next Generation of Advanced High Strength Sheet Steels," *Proc. 3rd Int. Conf. Adv. High Strength Steels*, pp. 774–781, 2006.

[27] E. De Moor, P. J. Gibbs, J. G. Speer, and D. K. Matlock, "Strategies for Third-Generation Advanced High-Strength Steel Development," *AIST Trans.*, vol. 7, no. 3, pp. 133–144, 2010.

[28] D. K. Matlock, J. G. Speer, E. De Moor, and P. J. Gibbs, "JESTECH RECENT DEVELOPMENTS IN ADVANCED HIGH STRENGTH SHEET STEELS FOR AUTOMOTIVE APPLICATIONS: AN OVERVIEW," 2012.

[29] J. Speer, D. K. Matlock, B. C. De Cooman, and J. G. Schroth, "Carbon partitioning into austenite after martensite transformation," *Acta Mater.*, vol. 51, no. 9, pp. 2611–2622, May 2003.

[30] D. V. Edmonds, K. He, F. C. Rizzo, B. C. De Cooman, D. K. Matlock, and J. G. Speer, "Quenching and partitioning martensite—A novel steel heat treatment," *Mater. Sci. Eng. A*, vol. 438–440, pp. 25–34, Nov. 2006.

[31] R. L. Miller, "Ultrafine-grained microstructures and mechanical properties of alloy steels," *Metall. Mater. Trans. B*, vol. 3, no. 4, pp. 905–912, Apr. 1972.

[32] Y. Ma, "Medium-manganese steels processed by austenite-reverted-transformation annealing for automotive applications," *Mater. Sci. Technol.*, vol. 33, no. 15, pp. 1713–1727, Oct. 2017.

[33] B. C. De Cooman, "Structure–properties relationship in TRIP steels containing carbide-free bainite," *Curr. Opin. Solid State Mater. Sci.*, vol. 8, no. 3–4, pp. 285–303, Jun. 2004.

[34] S. Lee, S.-J. Lee, and B. C. De Cooman, "Austenite stability of ultrafine-grained transformation-induced plasticity steel with Mn partitioning," *Scr. Mater.*, vol. 65, no. 3, pp. 225–228, Aug. 2011.

[35] P. J. Jacques, E. Girault, P. Harlet, and F. Delannay, "The Developments of Cold-rolled TRIP-assisted Multiphase Steels. Low Silicon TRIP-assisted Multiphase Steels.," *ISIJ Int.*, vol. 41, no. 9, pp. 1061–1067, Sep. 2001.

[36] H. K. D. H. Bhadeshia and D. V. Edmonds, "The bainite transformation in a silicon steel," *Metall. Trans. A*, vol. 10, no. 7, pp. 895–907, Jul. 1979.

[37] R. Schneider, K. Steineder, D. Krizan, and C. Sommitsch, "Effect of the heat treatment on the microstructure and mechanical properties of medium-Mn-steels," *Mater. Sci. Technol.*, pp. 1–9, Nov. 2018.

[38] H. Luo and H. Dong, "New ultrahigh-strength Mn-alloyed TRIP steels with improved formability manufactured by intercritical annealing," *Mater. Sci. Eng. A*, vol. 626, pp. 207–212, Feb. 2015.

[39] W. Q. Cao, C. Wang, J. Shi, M. Q. Wang, W. J. Hui, and H. Dong, "Microstructure and mechanical properties of Fe–0.2C–5Mn steel processed by ART-annealing," *Mater. Sci. Eng. A*, vol. 528, no. 22–23, pp. 6661–6666, Aug. 2011.

[40] S.-J. Lee, S. Lee, and B. C. De Cooman, "Mn partitioning during the intercritical annealing of ultrafine-grained 6% Mn transformation-induced plasticity steel," *Scr. Mater.*, vol. 64, no. 7, pp. 649–652, Apr. 2011.

[41] J. I. Kim, J. H. Ryu, S. W. Lee, K. Lee, Y.-U. Heo, and D.-W. Suh, "Influence of the Initial Microstructure on the Reverse Transformation Kinetics and Microstructural Evolution in Transformation-Induced Plasticity–Assisted Steel," *Metall. Mater. Trans. A*, vol. 47, no. 11, pp. 5352–5361, Nov. 2016.

[42] S. Yan, X. Liu, T. Liang, and Y. Zhao, "The effects of the initial microstructure on microstructural evolution, mechanical properties and reversed austenite stability of intercritically annealed Fe-6.1Mn-1.5Si-0.12C steel," *Mater. Sci. Eng. A*, vol. 712, pp. 332–340, Jan. 2018.

[43] E. De Moor, D. K. Matlock, J. G. Speer, and M. J. Merwin, "Austenite stabilization through manganese enrichment," *Scr. Mater.*, vol. 64, no. 2, pp. 185–188, Jan. 2011.

[44] F. B. Pickering, *Physical metallurgy and the design of steels*. Applied Science Publishers, 1978.

[45] E. M. Bellhouse and J. R. McDermid, "Selective oxidation and reactive wetting of 1.0 Pct Si-0.5 Pct Al and 1.5 Pct Si TRIP-assisted steels," *Metall. Mater. Trans. A Phys. Metall. Mater. Sci.*, vol. 41, no. 6, pp. 1539–1553, 2010.

[46] E. M. Bellhouse and J. R. McDermid, "Selective Oxidation and Reactive Wetting during Galvanizing of a CMnAl TRIP-Assisted Steel," *Metall. Mater. Trans. A*, vol. 42, no. 9, pp. 2753–2768, Sep. 2011.

[47] Q. Furnemont, "The micromechanics of TRIP-assisted multiphase steels," *PhD thesis*. Université Catholique de Louvain, 2003.

[48] Q. Furnémont, M. Kempf, P. J. Jacques, M. Göken, and F. Delannay, "On the measurement of the nanohardness of the constitutive phases of TRIP-assisted multiphase steels," *Mater. Sci. Eng. A*, vol. 328, no. 1–2, pp. 26–32, May 2002.

[49] P. J. Jacques, "Transformation-induced plasticity for high strength formable steels," *Curr. Opin. Solid State Mater. Sci.*, vol. 8, no. 3–4, pp. 259–265, Jun. 2004.

[50] P. Jacques, Q. Furnémont, A. Mertens, and F. Delannay, "On the sources of work hardening in multiphase steels assisted by transformation-induced plasticity," *Philos. Mag. A*, vol. 81, no. 7, pp. 1789–1812, Jul. 2001.

[51] Q. Furnémont, G. Lacroix, S. Godet, K. T. Conlon, and P. J. Jacques, "Critical Assessment of the Micromechanical Behaviour of Dual Phase and Trip-Assisted Multiphase Steels," *Can. Metall. Q.*, vol. 43, no. 1, pp. 35–42, Jan. 2004.

[52] J. R. McDermid, H. S. Zurob, and Y. Bian, "Stability of Retained Austenite in High-Al, Low-Si TRIP-Assisted Steels Processed via Continuous Galvanizing Heat Treatments," *Metall. Mater. Trans. A*, vol. 42, no. 12, pp. 3627–3637, Dec. 2011.

[53] G. B. Olson and M. Cohen, "Kinetics of strain-induced martensitic nucleation," *Metall. Trans. A*, vol. 6, no. 4, pp. 791–795, Apr. 1975.

[54] B. C. De Cooman, Y. Estrin, and S. K. Kim, "Twinning-induced plasticity (TWIP) steels," *Acta Mater.*, vol. 142, pp. 283–362, Jan. 2018.

[55] B. C. De Cooman, O. Kwon, and K.-G. Chin, "State-of-the-knowledge on TWIP steel," *Mater. Sci. Technol.*, vol. 28, no. 5, pp. 513–527, May 2012.

[56] S. Asgari, E. El-Danaf, S. R. Kalidindi, and R. D. Doherty, "Strain hardening regimes and microstructural evolution during large strain compression of low stacking fault energy fcc alloys that form deformation twins," *Metall. Mater. Trans. A*, vol. 28, no. 9, pp. 1781–1795, Sep. 1997.

[57] S. Allain, J.-P. Chateau, D. Dahmoun, and O. Bouaziz, "Modeling of mechanical twinning in a high manganese content austenitic steel," *Mater. Sci. Eng. A*, vol. 387–389, pp. 272–276, Dec. 2004.

[58] I. Gutierrez-Urrutia and D. Raabe, "Dislocation and twin substructure evolution during strain hardening of an Fe–22 wt.% Mn–0.6 wt.% C TWIP steel observed by electron channeling contrast imaging," *Acta Mater.*, vol. 59, no. 16, pp. 6449–6462, Sep. 2011.

[59] K. Steineder, D. Krizan, R. Schneider, C. Béal, and C. Sommitsch, "On the Damage Behavior of a 0.1C6Mn Medium-Mn Steel," *steel Res. Int.*, vol. 89, no. 9, p. 1700378, Sep. 2018.

[60] B. Sun *et al.*, "Revealing fracture mechanisms of medium manganese steels with and without delta-ferrite," *Acta Mater.*, vol. 164, pp. 683–696, Feb. 2019.

[61] S. W. Lee, K. Y. Lee, and B. C. De Cooman, "Ultra Fine-Grained 6wt% Manganese TRIP Steel," *Mater. Sci. Forum*, vol. 654–656, pp. 286–289, Jun. 2010.

[62] "ASTM E8/E8M - 16a: Standard Test Methods for Tension Testing of Metallic Materials 1," no. C, pp. 1–27, 2009.

[63] "ASTM E18 − 18a Standard Test Methods for Rockwell Hardness of Metallic Materials 1,2."

[64] A. Tyedmers, "Private Communication." 2018.

[65] "ASTM E975-13: Standard Practice for X-Ray Determination of Retained Austenite in Steel with Near Random Crystallographic Orientation 1," vol. 03, no. Reapproved 2008, pp. 1–7, 2009.

[66] R. C. Ruhl and M. Cohen, "Splat Quenching of Iron-Carbon Alloys," *Trans Met Soc*

AIME, vol. 245, no. 2, pp. 241–251, 1969.

[67] D. J. Dyson and B. Holmes, "Effect of Alloying Additions on the Lattice Parameter of Austenite," *J Iron Steel Inst.*, vol. 208, no. 5, pp. 469–474, 1970.

[68] A. W. Hull., "A New Method of X-Ray Crystal Analysis," *Phys. Rev.*, vol. 10, no. 6, pp. 661–696, Dec. 1917.

[69] Y. H. Choi *et al.*, "Influence of initial microstructures on intercritical annealing behaviour in a medium Mn steel," *Mater. Sci. Technol.*, pp. 1–9, May 2018.

[70] P. J. Gibbs, E. De Moor, M. J. Merwin, B. Clausen, J. G. Speer, and D. K. Matlock, "Austenite Stability Effects on Tensile Behavior of Manganese-Enriched-Austenite Transformation-Induced Plasticity Steel," *Metall. Mater. Trans. A*, vol. 42, no. 12, pp. 3691–3702, Dec. 2011.

[71] D. M. Field and D. C. Van Aken, "Dynamic Strain Aging Phenomena and Tensile Response of Medium-Mn TRIP Steel," *Metall. Mater. Trans. A*, vol. 49, no. 4, pp. 1152–1166, Apr. 2018.

[72] P. J. Jacques, Q. Furnemont, S. Godet, T. Pardoen, K. T. Conlon, and F. Delannay, "Micromechanical characterisation of TRIP-assisted multiphase steels by *in situ* neutron diffraction," *Philos. Mag.*, vol. 86, no. 16, pp. 2371–2392, Jun. 2006.

[73] prepared under the direction of the A. S. M. H. Committee, *ASM handbook. Volume 12, Fractography*. Metals Park, Ohio : American Society for Metals. c1987.

[74] G. Kurdjumov, "G. Kurdjumov and G. Sachs, Z. Phys. 64, 325 (1930).," *Z. Phys.*, vol. 64, p. 325, 1930.

[75] Z. Nishiyama, "X-ray investigation of the mechanism of the transformation from face centered cubic lattice to body centered cubic," *Sci. Rep. Tohoku Univ.*, vol. 23, p. 637, 1934.

[76] G. Wassermann, "Influence of the α-γ-transformation of an irreversible Ni steel onto crystal orientation and tensile strength.," *Arch. Eisenhüttenwes*, vol. 126, p. 647, 1933.

[77] B. V. N. Rao, "Communications On the Orientation Relationships Between Retained Austenite and "Lath" Martensite," 1979.

[78] P. Jacques, F. Delannay, X. Cornet, P. Harlet, and J. Ladriere, "Enhancement of the mechanical properties of a low-carbon, low-silicon steel by formation of a multiphased microstructure containing retained Austenite," *Metall. Mater. Trans. A*, vol. 29, no. 9, pp. 2383–2393, Sep. 1998.

[79] H. Luo, "Comments on 'Austenite stability of ultrafine-grained transformation-induced plasticity steel with Mn partitioning' by S. Lee, S.J. Lee and B.C. De Cooman, Scripta Materialia 65 (2011) 225–228," *Scr. Mater.*, vol. 66, no. 10, pp.

829–831, May 2012.

[80] Y. H. Choi *et al.*, "Materials Science and Technology Influence of initial microstructures on intercritical annealing behaviour in a medium Mn steel Influence of initial microstructures on intercritical annealing behaviour in a medium Mn steel," 2018.

[81] D. W. Suh, J. H. Ryu, M. S. Joo, H. S. Yang, K. Lee, and H. K. D. H. Bhadeshia, "Medium-Alloy Manganese-Rich Transformation-Induced Plasticity Steels," *Metall. Mater. Trans. A*, vol. 44, no. 1, pp. 286–293, Jan. 2013.

[82] B. C. De Cooman, P. Gibbs, S. Lee, and D. K. Matlock, "Transmission Electron Microscopy Analysis of Yielding in Ultrafine-Grained Medium Mn Transformation-Induced Plasticity Steel," *Metall. Mater. Trans. A*, vol. 44, no. 6, pp. 2563–2572, Jun. 2013.

[83] E. M. Bellhouse and J. R. McDermid, "Effect of Continuous Galvanizing Heat Treatments on the Microstructure and Mechanical Properties of High Al-Low Si Transformation Induced Plasticity Steels," *Metall. Mater. Trans. A*, vol. 41, no. 6, pp. 1460–1473, Jun. 2010.

[84] M. Zhang, L. Li, Y. Su, R. Fu, Z. Wan, and B. C. De Cooman, "Forming Limit Curve (FLC) and Fracture Mechanism of Newly Developed Low-Carbon Low-Silicon TRIP Steel," *steel Res. Int.*, vol. 78, no. 6, pp. 501–505, Jun. 2007.